

**The identification of detectable
gravitational wave signatures using
the Einstein formalism for various
classes of Galactic sources**

Jacques Maritz

Submitted in fulfilment of the requirements for the
degree

Magister Scientiae

in the Faculty of Natural and Agricultural Sciences,
Department of Physics,
University of the Free State,
South Africa

Date of submission: January 2014

Supervised by: Prof P.J. Meintjes, Department of
Physics

The financial assistance of the South African Square Kilometre Array Project towards this research is hereby acknowledged. Opinions expressed and conclusions arrived at, are those of the author and are not necessarily to be attributed to the NRF.

Abstract:

A central result of this thesis is the prediction of short period (transient) GW signatures, using General Relativity. This thesis focused on various LIGO and SKA Gravitational Wave (GW) sources such as collapsing supernovae, rapidly spinning magnetars, the coalescence of compact binary objects and the stochastic Gravitational Wave backgrounds produced by Super Massive Black holes. Upper limits for the GW amplitudes and frequencies were predicted by means of numerical and analytic methods. Finally, the prospects of detecting Gravitational Waves from the galactic center will be discussed.

Opsomming:

'n Kern deel van die projek was die identifisering van Gravitasie Golf spektra wat deur galaksiese bronne geproduseer word, met die gebruik van Alegmene Relatiwiteit. Hierdie projek het gefokus op verskeie LIGO en SKA Gravitasie Golf bronne soos supernovas, magnetars, die samesmelting van kompakte binêre voorwerpe en die stogastiese Gravitasie Golf agtergronde wat deur massiewe gravitasie kolke veroorsaak word. Bo-grense vir die Gravitasie Golf amplitudes en frekwensies was bereken deur gebruik te maak van numeriese en analitiese metodes. Gevolglik word die vooruitsigte vir moontlike waarneming van Gravitasie Golwe uit die galaktiese middelpunt ook bespreek.

List of acronyms:

GWs	Gravitational Waves
SKA	Square Kilometre Array
PTA	Pulsar Timing Array
SPH	Smooth Particle Hydrodynamics
BH	Black hole
NS	Neutron star
NSNS	Binary neutron star systems
SN	Supernovae
GC	Galactic center
LIGO	Laser Interferometer Gravitational Wave Observatory
TT	Trace-Transverse gauge
EM	Electromagnetic
GRB	Gamma-Ray Burst
CGWAS	Caltech Gravitational Wave Astrophysics School 2013

Acknowledgements:

TO MY HEAVENLY FATHER, ALLOWING ME TO INDULGE IN HIS BEAUTIFUL
CREATION. To Prof Meintjes and Elizabeth, thank you.

The financial assistance of the South African Square Kilometre Array Project towards
this research is hereby acknowledged. Opinions expressed and conclusions arrived at, are
those of the author and are not necessarily to be attributed to the NRF.

List of symbols:

Sign Convention	$(-, +, +, +)$
Coordinates on manifold M	x^α
Hypersurface	Σ
Orthonormal basis	\hat{e}_μ^α
Metric on M	$g_{\alpha\beta}$
Christoffel symbols	$\Gamma^\alpha_{\beta\gamma}$
Co-variant derivative	$A^\alpha_{\beta;\mu}$
Lie derivative of A^α	$Le(A^\alpha)$
Killing vector	ζ^α
Quadrupole tensor	Q^{ij}
GW induced stress	h

TABLE OF CONTENTS:

Chapter 1. Introduction	(9)
Chapter 2. A mathematical review of the properties of GWs within the frameworks of General Relativity and the Post Newtonian theory.....	(21)
2.1. Introduction to the weak field limit and the quadrupole formalism.....	(21)
2.2. The Post Newtonian approximation of Gravitation in flat space through the use of the pipeline NEWSOR.....	(26)
2.2.1. Introduction	(26)
2.2.2. Calculating the metric, mass and gravity tensors.....	(33)
2.2.3. Post Newtonian Gravitational Waves.....	(36)
Chapter 3. LIGO Sources of Gravitational Waves within the quadrupole formalism...(40)	
3.1. Introduction to LIGO sources.....	(40)
3.2. Supernovae core bounce.....	(46)
3.3. Spinning objects.....	(60)
3.4. A primitive magnetar model	(73)
3.5. Binary neutron star mergers.....	(80)

3.6. Binary neutron stars.....	(84)
--------------------------------	------

Chapter 4. Implementing the quadrupole formalism in a numerical framework.....(88)

4.1. Gravitational Wave signatures from supernovae core bounce using Smooth Particle Hydrodynamics.....	(88)
--	------

Chapter 5. Pulsar Timing Arrays and Gravitational Waves from the galactic center (97)

5.1 SKA Pulsar Timing Arrays.....	(99)
5.2 Conclusion: Gravitational Waves from the galactic center.....	(107)

Chapter 6. Conclusion.....(116)

Bibliography.....(110)

Appendix A

The weak field Limit and the quadrupole formalism.....	(118)
--	-------

Appendix B

Detector sensitivity curves.....	(127)
----------------------------------	-------

Appendix C

Post Newtonian expansion of Gravitation in flat space.....	(128)
--	-------

Appendix D

GADGET code and files.....	(133)
----------------------------	-------

Chapter 1

Introduction

Gravitational waves (GWs) are ripples in spacetime that are directly predicted by Einstein's geometric interpretation of gravity, ultimately opening a new window in astronomy. Nature provides us with equations, such as Maxwell's equations, that have radiative solutions; it is therefore no surprise that the Einstein's equations also contain radiative solutions in the form of GWs. These waves travel at the speed of light from the radiating source, carrying energy away from the system. The non-dispersive nature of the GWs allows them to propagate unhindered through the universe. The existence of GWs can contribute to physicists' and astronomers' understanding of the universe and the explanation of some of the most fundamental laws of physics.

Gravitational waves are very small distortions of spacetime geometry which propagate through space as waves. These distortions of spacetime are caused by massive bodies and travel through Universe with the speed of light. Gravitational waves squeezes and stretches spacetime by very small quantities. This squeezing and stretching (the strain) of spacetime itself is denoted by the symbol h . This characteristic also mathematically produces the wave polarizations of the GW (see Fig. 1.1, Fig. 1.2 and Appendix A). These tiny changes can be detected by isolating the test masses from all other disturbances in the vicinity. Massive objects that move curve, spacetime. It takes time for the spacetime to react and ripples in spacetime occur since information propagates at the speed of light. This is analogous to the ripples on a pond if you were to disturb the surface by throwing in a large object.

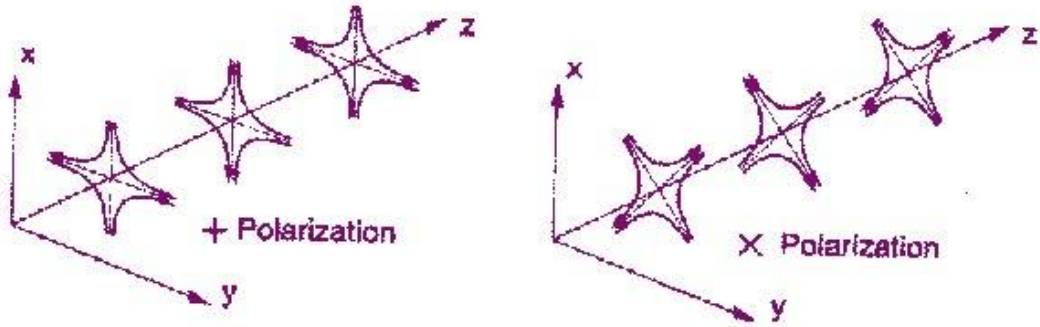


Fig. 1.1: The two polarizations of the propagating GW (h_+ and h_x); the characteristic strain of this wave correspond to $h \sim \Delta L/L$ (From Aharonian et al., 2013).

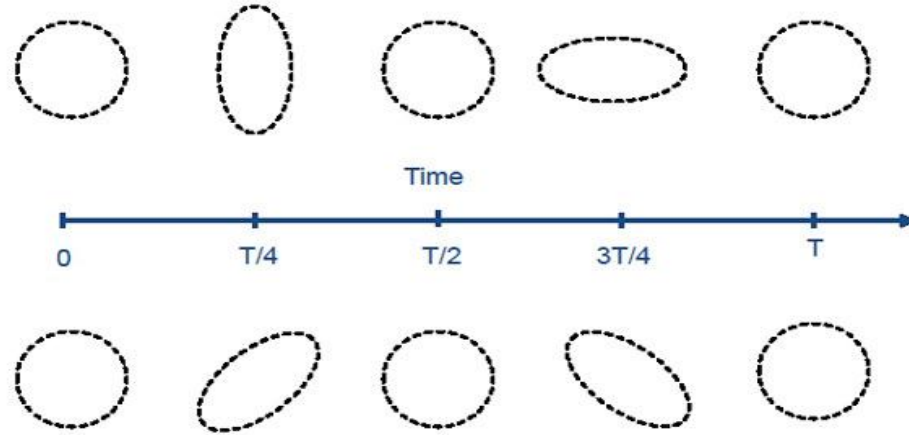


Fig. 1.2: The time evolution of test masses. The GW stretches and pulls the mass configuration (like a tidal force) corresponding to the unique polarizations (h_+ and h_x) as the wave propagates in spacetime itself (From Aharonian et al., 2013).

GW sources are divided up into several frequency classes: low frequency ($f \sim 10^{-8} - 10^{-6}$ Hz), intermediate frequency ($f \sim 10^{-4} - 10^{-2}$ Hz) and high frequency ($f \sim 1 - 3000$ Hz). These various classes of GWs can be detected with the SKA (using Pulsar Timing Arrays and radio telescopes), eLISA (interferometers in space) and LIGO respectively. GWs signatures produced by transient astrophysical sources are divided into several classes: burst signature (unique characteristic of the signature appearing

once), continuous signatures (repeatable signature), chirp signatures and stochastic backgrounds (signatures produced by population of gravitating astrophysical objects).

The universe is possibly filled with small, very detailed background sounds (like deep hums) from the early universe or from massive objects orbiting one another. The background therefore will consist of extremely old signals from the very early universe, as well as the slow interactions of massive binary black holes. This source is known as a stochastic GW background and scales as a power law of the characteristic frequency associated with the gravitating population (e.g. the stochastic background produced by colliding Super Massive Black holes). The SKA (see Fig. 1.3) proposes a unique system that could observe a stochastic GW background that is produced by a population of SMBH binaries. This could be done by using pulsar timing arrays; arrays of pulsars where each earth-pulsar arm forms a leg of an interferometer, after which an incoming GW would influence the pulse train from the pulsar, producing residuals in the ultra-fine timing measurements of the pulsar. This source of GWs is considered as low amplitude waves ($f \sim \text{nHz}$).



Fig. 1.3: The Kat-7 radio telescope; the basis of the SKA project and the proposed Pulsar Timing Array GW detection model (From www.ska.ac.za).

More exotic objects such as neutron stars (continuous gravitational wave sources) and supernovae events (burst gravitational wave sources) are candidates for strong GW radiation. The Hulse-Taylor (Aharonian et al., 2013) binary neutron star system, named after the astronomers who discovered the system more than 20 years ago and was

rewarded the Nobel Prize in 1993, provided the first indirect detection of the emission of GWs. These authors showed that the measured orbital decay coincides with the theoretical predictions made by the theory of General Relativity to better than 1%. Fig. 1.4 illustrates an over-simplified binary orbital evolution (such as the Hulse-Taylor binary pulsar) in spacetime, producing ripples in the fabric of spacetime.

These objects (neutron stars and binary mergers) generate a wide range of unique GWs. Gravitational waves produced by these sources are planned to be detected by LIGO using laser interferometry. This process involves the observation of the change in the path travelled by a photon in one of these interferometer arms. This small disturbance in the photon path length can be in principle caused by the stretching and squeezing of spacetime induced by the GW travelling into the plane of the detector. LIGO will only be able to detect objects within the frequency band of 3-3000 Hz.

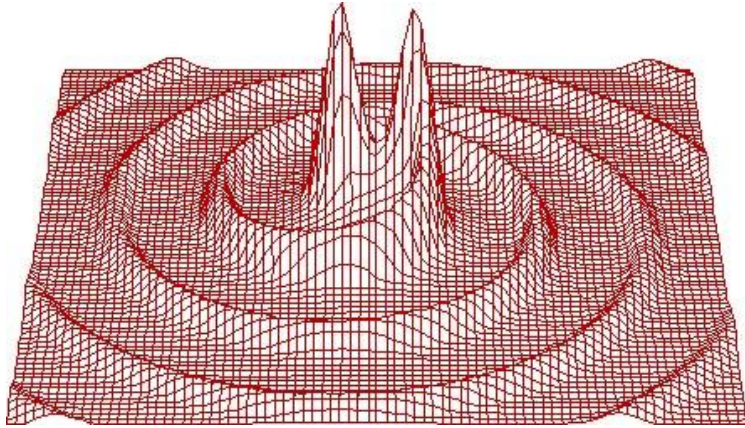


Fig. 1.4: Visualization of ripples in spacetime caused by evolving binary systems (From Aharonian et al., 2013).

To put the relative sizes of GWs from different astrophysical sources into context, we refer the reader to Fig. 1.5 that illustrates the upper limits for the GW strains produced by various binary systems. The formula that was used to obtain the GW upper limits for various binary sources $\left(h \sim \frac{MG^2}{dc^4a} \right)$ scales sensitively with the distance from the detector to source (d), the total mass of the companions (M) and the separation distance of

companions (a). This relation will be derived in detail in the Chapter 3 (see Eq. (3.37) in Section 3.6) and represents the amplitude of the GW wave produced by binary mergers as a function of orbital frequency, since the distance between the companions (a) can be related to the orbital frequency by using Kepler's law $\left(2\pi f_{\text{orbital}} = \sqrt{GM/a^3}\right)$.

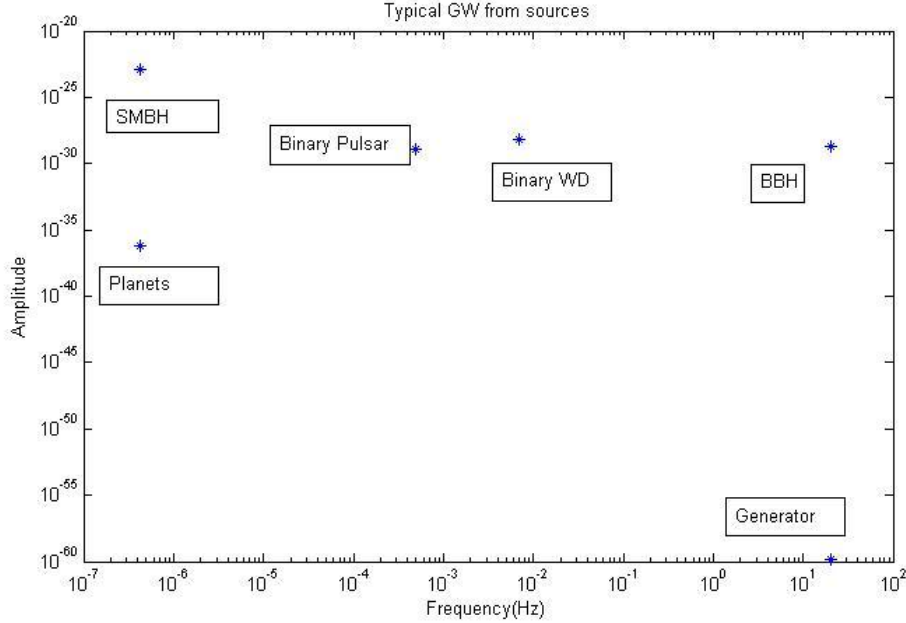


Fig. 1.5: GW upper strain $\left(h \sim \frac{MG^2}{dc^4 a}\right)$ limits for various binary sources. Planets: Jupiter-Sun binary, BBH: binary stellar mass black hole ($m_1 = m_2 \sim 1.4M_\odot$), SMBH: binary super massive black hole ($m_1 = m_2 \sim 10^6 M_\odot$), a GW generator containing two one ton masses orbiting one another with a frequency of $f = 10$ Hz, NSNS: the Hulse-Taylor pulsar and WDWD: binary white dwarf system (with mass $m_1 = m_2 \sim \frac{1}{2}M_\odot$ and an orbital period of 30 minutes).

Future space based detectors such as the Laser Interferometer Space Antenna (LISA) will be detecting GWs from extreme mass ratio inspirals (EMRIs). This GW source essentially originates from a light object orbiting a massive object. One example of this is a neutron star (or a stellar black hole) orbiting SgrA* (Aharonian et al., 2013).

The LIGO (Laser Interferometer Gravitational Wave Observatory, see Fig. 1.6) detectors are situated in Hanford and Livingston (USA). LIGO has already performed several tests and upgrades to their system (see Fig. 1.7). Fig. 1.7 illustrates the strain spectral amplitude (h_f), defined as the square of the power per unit frequency (S_h), plotted as a function of frequency between 3-3000 Hz (see Appendix B). The collaboration initialized the AdvLIGO system, which will be more sensitive than the original LIGO design. AdvLIGO has the capability of detecting GWs from merging neutron stars up to a distance of 30 Mpc (Matthew Pitkin et al., 2012), see Fig 1.8.

It is the stretching and squeezing characteristic of the wave that inspired most of the engineering behind LIGO, which was one of the first facilities specifically designed to detect GWs from astrophysical events, see Fig. 1.6.



Fig. 1.6: The LIGO instrument located in Hanford (USA), the unique design of the perpendicular interferometer arms rest is based on the two GW polarizations (From www.ligo.caltech.edu).

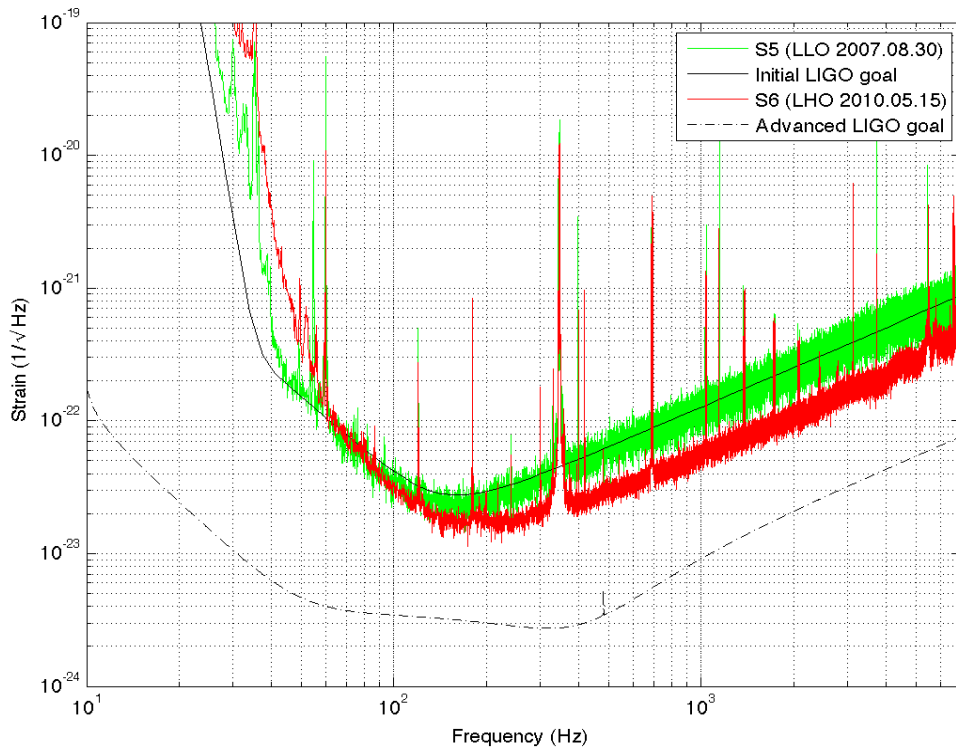


Fig. 1.7: Goals and test runs of LIGO down to the Advanced LIGO sensitivity. The graph shows clear noise contributions due to shot noise ($10 \text{ Hz} < f < 100 \text{ Hz}$) and thermal noise ($1000 \text{ Hz} < f < 3000 \text{ Hz}$) (From www.ligo.caltech.edu). The y-axis represents the strain spectral amplitude (h_f). Shot noise is due to the photon bouncing between the mirrors and the interferometer arms, several times, before exciting the interferometer.

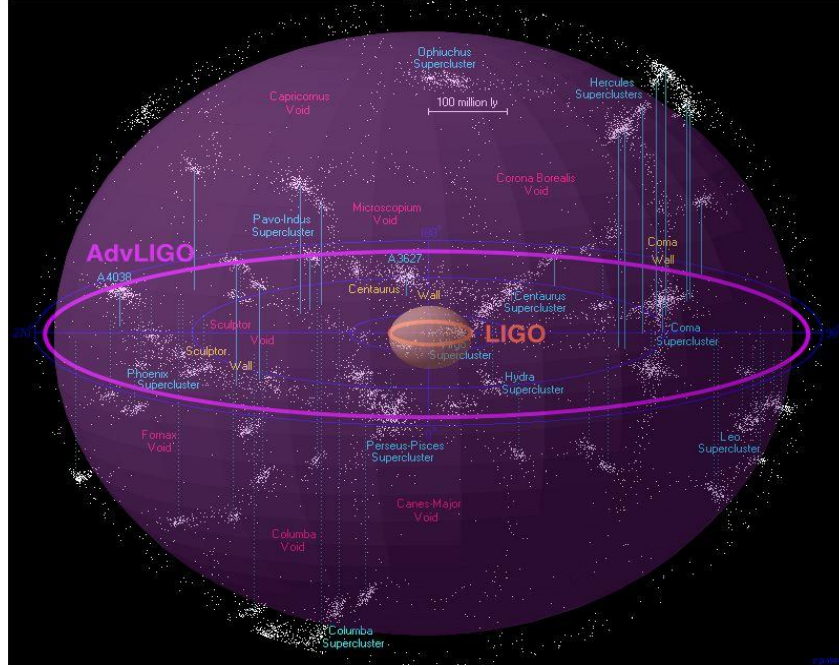
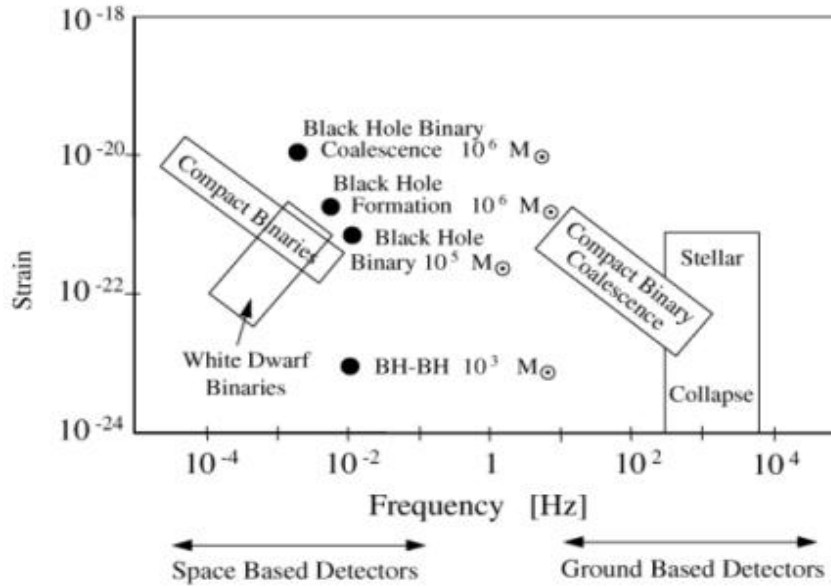


Fig. 1.8: The enlarged observational field of the newly proposed AdvLIGO interferometer (From www.ligo.caltech.edu).

LIGO (and AdvLIGO) will allow the observer to detect high frequency GWs from astrophysical sources such as spinning stars and binary merging events. These detectors provide the possibility of verifying the existence of black holes through their interactions with one another and their GW signatures that they produce. Furthermore, it will be able to detect GWs from other astrophysical objects such as magnetars and supernovae. The GW spectra they produce could be linked to their electromagnetic counterparts (as part of a multi-messenger network) (Matthew Pitkin et al., 2012).

The new SKA project will be the most sensitive and fastest surveying radio telescope available (Aharonian et al., 2013). The SKA will detect dipole electromagnetic radiation in the frequency range of between 70 MHz to 10 GHz with an angular resolution of less than 0.1 arcsecond. The SKA is aiming to detect stochastic GW backgrounds (see the low frequency ($f \sim 10^{-8} - 10^{-6}$ Hz) part of the sensitivity curve in Fig. 1.8b) via the precise timing of pulsars.

(a)



(b)

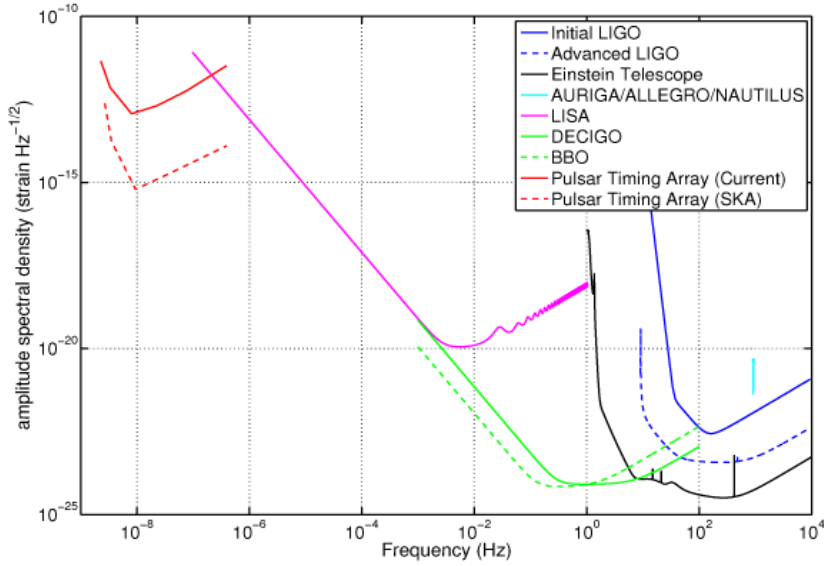


Fig. 1.9 (a,b): Benchmark sensitivity curves for several modern ground and space interferometers (from Matthew Pitkin et al., 2012). LIGO's frequency band spans the range between 3-3000 Hz and is sensitive for GWs with typical strains ranging between $h \sim 10^{-21} - 10^{-20}$.

Gravitational wave astronomy, being radically different from all electromagnetic wave observations, can create a new spectrum of observations to link with the SKA project. Phenomena under investigation (Aharonian et al., 2013) include: The in-spiral and coalescence of pairs of neutron stars, the merging of super massive binary black holes (Taylor et al., 1982) and glitches in neutron stars. These glitches change the spinning star's magnetic field, moment of inertia and spin configuration, modifying the dynamics and effectively changing the GW spectrum. LIGO will be searching for these neutron star glitch signatures in the GW spectra.

Einstein showed the existence of GWs in a 1916 paper (Einstein, 1915), but later corrected all the mathematical errors in his 1918 paper (Einstein, 1916). We shall only mention the recent development in the field of GW astronomy. Throughout the 1960s, Chandrasekhar developed his own slow-motion formalism, dealing with extended fluid bodies (as opposed to point masses) at one post-Newtonian order after another (Chandrasekhar, 1970). Burke and Thorne derived the quadrupole formalism for the GW emission from binary systems (Burke and Thorne, 1970). The field of GW astronomy consists of the numerical simulation (and analytical modelling) of waves produced by binary interactions and transient sources (together with the associated electromagnetic counterparts). Huge efforts are being done in the field of the Post Newtonian theory to describe the orbits (and essentially the GW signature) of mergers to a very high accuracy (Blanchet, 1989). Numerical relativists design and construct complicated codes to solve Einstein equations to produce GW signatures generated by stellar core collapse (Reiswig, 2011) and binary mergers (Hughes, 2009). A great deal of effort is going into understanding the transient GW sky. This includes: GW population predictions, GW signature production and instrumental design (Anderson, 2013).

The purpose of this thesis is to understand the basic GW signatures from various sources that could be observed by LIGO and the SKA. In this thesis we investigated numerical and analytical models for GW signatures produced by several astrophysical objects. We

extended the GADGET (Springel, 2005) code to include a GW module (without GW back reaction). With the SKA coming online in the near future, we investigated GW signatures from stochastic backgrounds and debated the idea of a multi-detector system consisting of LIGO, the SKA and high energy telescopes such as CHANDRA or FERMI.

One of the most exciting hosts of exotic gravitating objects is the galactic centre (GC). It possibly contains many GW sources. Modern-day formation rate studies predict the existence of a few hundred millisecond pulsar (MSP)-Black hole (BH) binaries in the GC. It also predicts the possibility of MSPs orbiting the SMBH (SgrA*) in the GC. This provides a great opportunity to combine GW and radio astronomy to investigate some theories associated with black holes and star (or pulsar) formation rates. The SKA will be a good tool for this endeavour since it can potentially reveal a collection of several thousand pulsars (Aharonian et al., 2013). However, since most of the GW observations of the transient galactic sources fall into the LIGO (more recently the AvdLIGO) band, the SKA will play a major role in the field of GW astronomy through pulsar observations and Pulsar Timing Arrays (PTAs). Supernovae events also support the possibility of multi-detector systems. Supernovae core bounce events could be detected by LIGO (that serves as an early trigger), followed moments after by follow-up observations by other detectors. This process will explore and exploit the physics of astrophysical objects in a unique way.

Chapter 2 gives a mathematical review of the properties of GWs within the frameworks of General Relativity and the Post Newtonian Theory. Chapter 3 and Chapter 4 outline the application of the quadrupole formalism to various transient LIGO sources (both analytical and numerical modelling). Chapter 5 outlines the prospects of detecting GWs with the new and upcoming SKA and the possibility of detecting GWs from the galactic center. Lastly, Chapter 6 presents a discussion of the results presented in this study.

Chapter 2

A mathematical review of the properties of GWs within the frameworks of General Relativity and the Post Newtonian Theory

2.1 Introduction to the weak field limit and the quadrupole formalism

Einstein showed that the existence of GWs is a natural consequence of GR. He showed that when flat spacetime is perturbed slightly, the field equations lead to a wave equation for perturbation. This wave equation has solutions that behave like “transverse” waves, and propagate non-dispersively through spacetime.

It was mentioned in Chapter 1 that spacetime itself is very rigid. In order to produce a weak field limit approximation and derive an equation to relate a gravitational wave to a possible source (typically being the stress energy tensor $T^{\mu\nu}$) a very small perturbation ($\|h_{\mu\nu}\| \ll 1$) can be introduced to the background metric ($g_{\mu\nu}$). The justification of the small perturbation comes from the fact that spacetime is so rigid. Starting with a Lorentz (local inertial) coordinate system

$$g_{\mu\nu} = \eta_{\mu\nu} + h_{\mu\nu}. \quad (2.1)$$

This perturbation leads to a wave equation (see Appendix A for detailed derivation)

$$\square \bar{h}_{\mu\nu} = -\frac{16\pi G}{c^4} T_{\mu\nu}, \quad (2.2)$$

where \square represents the D'Alembertian operator. The solution of Eq. (2.2) is a wave equation which is similar to the electromagnetic wave equation. Electromagnetic radiation is produced whenever charge is accelerated through space and is dipolar in nature (only the leading contribution). Gravitational radiation differs from this in the sense that its leading contribution is that of the quadrupole mass moment associated with the mass distribution. Using the basic principles of the Green's solution (analogous to electromagnetic radiation), a solution of the wave equation could be

$$\bar{h}_{\mu\nu}(t, \bar{x}) = \frac{4G}{c^4} \int \frac{T_{\mu\nu}(t - |\bar{x} - \bar{y}|, \bar{y})}{|\bar{x} - \bar{y}|} d^4y. \quad (2.3)$$

where \bar{x} and \bar{y} represents the spatial coordinates of the field point and the source, respectively, and $|\bar{x} - \bar{y}|$ represents the distance between the source and the field point. If we assume that the source is moving relatively slowly ($v/c \ll 1$) and that the internal field is weak, then the GWs emitted by the physical systems can be approximated; this is the origin of the quadrupole formalism. The quadrupole tensor is defined as

$$Q^{ij} = \int y^i y^j T^{00} d^3y \quad (2.4)$$

The general expression for $h_{ij}^{TT}(t, d)$ was derived by solving the wave equation in the far field limit and implementing the transverse-traceless (TT) gauge on the solution ($h_{ij} \rightarrow h_{ij}^{TT}$). The traceless part of the gauge insures that that metric is trace-free and the transverse part of the gauge projects the tensor components into a plane that is orthogonal to the direction of propagation. This operation produces the quadrupole GW signature approximation formula of a system evolving with time:

$$\bar{h}_{ij}^{TT} = \frac{2G}{rc^4} \Lambda_{ijkl} \hat{\dot{Q}}^{kl} \quad (2.5)$$

Here $\Lambda_{ijkl} = P_i^k P_j^l - \frac{1}{2} P^{kl} P_{ij}$ represents the projection tensor (orthogonal to the direction of wave propagation), with r being the distance to the source and where $\hat{\dot{Q}}^{kl} = Q^{kl} - \frac{1}{3} \delta_{kl} Q$ represents the reduced quadrupole tensor. Also we have that $P_{ij} = \delta_{ij} - \hat{x}_i \hat{x}_j$. The reader is referred to Appendix A for detailed derivations of this main result which includes the use of the relevant gauges.

The quadrupole mass moment is generated by decomposing the mass distribution (or source) into spherical harmonics (if we wish to work in spherical harmonics)

$$F(\theta, \phi) = C + C_i n^i + C_{ij} n^i n^j + \dots \quad (2.6)$$

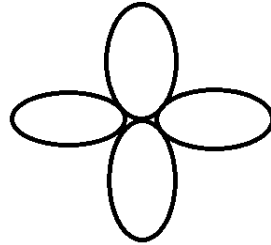


Fig. 2.1: Visualization of the quadrupole mass distribution that allow physicists to approximate certain complex systems and extract GW from the accelerating mass distributions.

Here $C_i n^i$ corresponds to the monopole moments and $C_{ij} n^i n^j$ to the quadrupole moments in the general multi-pole expansions of a mass distribution. This formalism could be applied to several systems, analytical and numerical, to extract GW signatures from the evolving system. In this thesis the strain spectra will be computed (analytical and

numerical) for SN core bounce, rigid deformed rotating bodies, and compact binaries, representing the possible LIGO GW sources (see Chapter 3).

To illustrate the use of the quadrupole formalism, consider a binary system of masses M_1 and M_2 respectively, with reduced mass $\mu = M_1 M_2 / (M_1 + M_2)$. In the xy-plane, the binary system has a angular frequency of ω , hence coordinates $x = r \cos \omega t$ and $y = r \sin \omega t$, see Fig. 2.2.

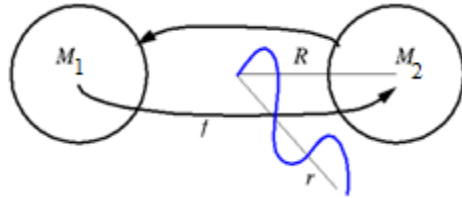


Fig. 2.2: The visualization of a binary system that emits GWs with a frequency of $f_{GW} \sim 2f_{orbital}$ (from Alan Weinstein CGWAS 2013). CGWAS (Caltech Gravitational Wave Astrophysics School) was held in July 2013 at Caltech in Pasadena.

Using the standard formula for the quadrupole tensor, some of the components of Q^{ij} were calculated for this system, using Eq. (2.5).

$$\begin{aligned}
 Q^{11} &= \mu r^2 (\cos^2 \omega t - \frac{1}{3}) \\
 Q^{22} &= \mu r^2 (\sin^2 \omega t - \frac{1}{3}) \\
 Q^{33} &= -\frac{1}{3} \\
 Q^{21} &= \sin 2\omega t / 2 \\
 Q^{12} &= \sin 2\omega t / 2.
 \end{aligned} \tag{2.7}$$

Here the projection operators (used to construct the projection tensor Λ_{ijkl}) are $P_{11} = P_{22} = 1$ and $P_{33} = 0$, if the binary rotates around the z-axis. One could derive a

general formula for the GW emitted by such a binary system; if the separation distance of the binary is a and the source is located at a distance d , then Eq. (2.5) reduces to

$$h_{ij}^{TT}(t, d) = \frac{4\mu MG^2}{dc^4 a} K_{ij}^{TT}. \quad (2.8)$$

Where the tensor K_{ij}^{TT} contains the polarized oscillatory part (containing either $\cos 2\omega t$ or $\sin 2\omega t$) and $h_0 = 4\mu MG^2 / adc^4$ plays the role as the amplitude of the wave. The upper limit for h_0 is the amplitude h (mentioned in Chapter 1), where M represents the total mass, d the distance to the source and a the binary separation.

Fig. 2.3 illustrates a typical GW signature produced by merging binary neutron stars. Simulation methods used to produce the GW signature includes: Post Newtonian (PN) frameworks, numerical relativity (NR) and hybrid (HYB) techniques. The hybrid method combines both Post Newtonian techniques and numerical relativity to produce a fast (and computationally cheap) algorithm to obtain GW signatures from merging binary neutron stars and merging black holes. Noticeable from Fig. 2.3 is the correlation between the two polarizations of the merging binary GW signature, h_+ and h_\times . These two polarizations are out of phase, but still represent all the parts of the signature: the “chirp” signature (pre-merger) and the ring-down signature (post-merger). The merger signature illustrated in Fig. 2.3 was produced by using numerical relativistic algorithms (Kiuchi, 2012).

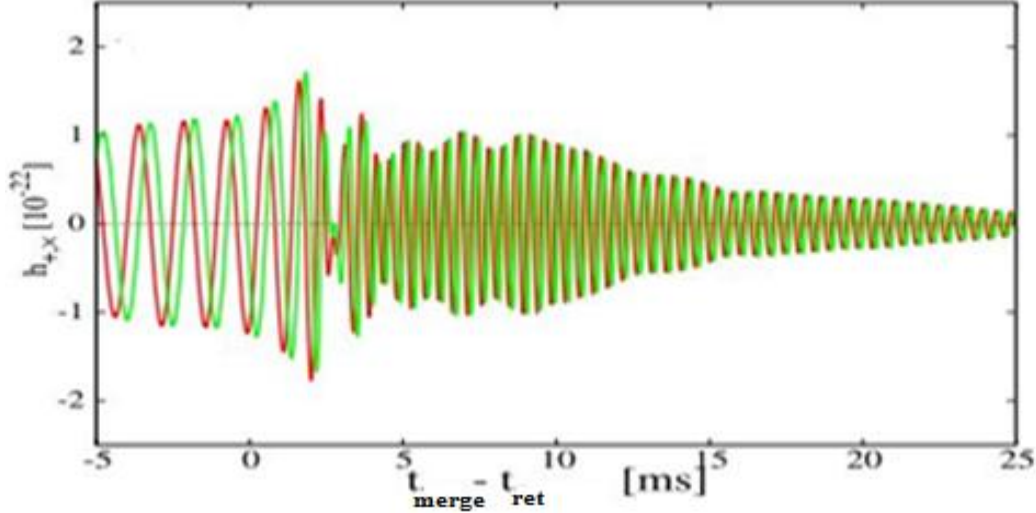


Fig. 2.3: The typical “chirp” (the GW signal translates to an audible chirp sound) and rung-down GW spectrum of young compact binaries (from Kiuchi, 2012).

The example above illustrates a GW template for equal-mass binary neutron star mergers. This implies that the GW signature produced by binary systems (such as the binary system PSR913+16 (King, 1986) which has orbital parameters: $m_1 \sim m_2 \sim 1.4M_{\odot}$, $a \sim 10^{12}$ cm, $T \sim 7$ h 45 min and orbital eccentricity $e \sim 0.617$) will resemble the signature illustrated in Fig. 2.3. The fundamental methodology depicted in this example will be followed throughout this thesis when predicting GW upper limits for various galactic sources.

The GW signature produced by the coalescence of binary neutron stars (see Fig. 2.3) illustrates the main methods used to predict these chirp waveforms (using numerical, hybrid or Post Newtonian methods). Thus, the following sections will outline fundamental methods used in Post Newtonian and Numerical Relativity theories to extract GWs from astrophysical systems.

2.2 The Post Newtonian approximation of Gravitation in flat space through the use of the in-house developed pipeline NEWSOR

2.2.1 Introduction

For the PN theory the source is regarded as a perfect fluid; and is characterized by its velocity (v), density (ρ), pressure (P) and the normalized internal energy density of the system (Π). The parameters of interest are

$$\left\{ v, P, \rho, \Pi, \frac{P}{\rho} \right\}. \quad (2.9)$$

This set of PN parameters completely characterizes the weak-field behaviour of the PN theory. We use two metric potentials to ensure a unique solution in the PN framework

$$U(x^i, t) = k \int \frac{\rho(x^i, t)}{|x - x^i|} dx^i, \quad (2.10)$$

which is the gravitational potential and

$$V^\mu(x^i, t) = k \int \frac{\rho(x^i, t) v^\mu(x^i, t)}{|x - x^i|} dx^i. \quad (2.11)$$

Where k and $v^\mu(x^i, t)$ represent the gravitational constant and the four velocity of the system respectively. To keep the system Newtonian (slow moving and small internal energy) the following conditions must hold (Petry, 1979): $v^2 < U$, $\frac{P}{\rho} < U$ and $\Pi < U$.

Since $\Pi = \frac{\text{internal energy}}{\text{mass}} \sim 10^{-5}$ the order of the parameter set becomes

$$\left\{ v^2, U, \Pi, \frac{P}{\rho} \right\} \sim O(2).$$

As in the theory of Relativity, orbits of particles are determined by calculating the Lagrangian (L) of particle. The starting point of this theory is the Newtonian Lagrangian of a particle

$$L_M \sim -\rho g^{\mu\nu} \frac{P_\mu}{m_0} \frac{P_\nu}{m_0}. \quad (2.12)$$

Writing this in metric form $\left(L_M = -m_0 \int (-g_{00} - 2g_{0j}v^j - 2g_{jk}v^jv^k)^{0.5} dt \right)$ it becomes evident that $L \sim O(2)$, since the Newtonian metric has components

$$g^{\mu\nu} = \begin{bmatrix} 1 - \frac{2}{c^2}U & 0 & 0 & 0 \\ 0 & 1 - \frac{2}{c^2}U & 0 & 0 \\ 0 & 0 & 1 - \frac{2}{c^2}U & 0 \\ 0 & 0 & 0 & 1 + \frac{2}{c^2}U \end{bmatrix}. \quad (2.13)$$

To construct a Post Newtonian Lagrangian ($L \sim O(4)$), we need to expand the components of the metric respectively:

$$\begin{aligned} g_{00} &\sim O(4) \\ g_{0j} &\sim O(3) \\ g_{jk} &\sim O(2). \end{aligned} \quad (2.14)$$

This is analogous to Einstein's theory. The description (or “accuracy”) of the metric determines whether the gravitational field of the source is present and determines the accuracy of particle orbits.

The Post Newtonian (PN) expansion is useful for describing the motion of binary systems and the GW signatures for a complete range of binary compact objects. One could use this theory to model the solar system properties, predict GW radiation from systems and accurately describe the properties of compact objects to reveal certain orbital dynamics which cannot be determined by Newtonian theories (such as the precession of Mercury around the Sun and the shrinking of an elliptical orbit due to GW emission).

The methodology followed in this chapter we transformed a two particle system into a center mass problem (one particle orbiting around an equivalent central massive object). The objects have position vectors \bar{x}_1 and \bar{x}_2 , with the separation vector being $\bar{x} = \bar{x}_1 - \bar{x}_2$.

The Post Newtonian theory investigates the acceleration of this separation vector, $\ddot{\bar{x}}$. This vector can be written in the form $\ddot{\bar{x}} = \ddot{\bar{x}}_N + \ddot{\bar{x}}_{PN} + \ddot{\bar{x}}_{2PN} \dots$. Here $\ddot{\bar{x}}_N$ and $\ddot{\bar{x}}_{PN}$ are derived from the standard Newtonian potential and the Post Newtonian potential. Investigating all these effects could give some insight into all the corrections needed to model a realistic particle orbit. One example of these Post Newtonian orbital corrections is the geodesic effect (Precession of orbits), see Fig. 2.4. The geodesic effect occurs when the particle's orbit is expanded to the order c^{-2} . See Blanchet et al. (1989) for an overview of the Post Newtonian theory. This will now be investigated by determining the PN orbital corrections. I will use the galactic center as an example (see Fig. 2.4).

The main use of the PN theory in modern gravitation research is the prediction of higher accuracy orbits of binary systems (whether it is merging binary black holes or neutron stars). This process requires a PN expansion of the Hamiltonian ($H = H_N + H_{PN} + H_{2PN} \dots$). We also need to calculate the conserved quantities (such as the energy and the angular momentum of the system). These can then be used to setup the equations governing the trajectory of the particle (or star) to order c^{-2} . See Fig. 2.4.

The clover-like orbit of the timelike particle (neutron star) orbiting a super-massive object (Sgr A*) in Fig. 2.4, was produced by solving the Euler-Lagrange equation

$$\frac{d}{d\lambda} \frac{\partial L}{\partial \dot{x}^\alpha} - \frac{\partial L}{\partial x^\alpha} = 0, \quad (2.15)$$

where λ represents an affine parameter along the world-line of the particle. In the Newtonian limit we have that $d\lambda = dt = d\tau$. Here $L = g_{tt}\dot{t}^2 + g_{\theta\theta}\dot{\theta}^2 + g_{\phi\phi}\dot{\phi}^2 + g_{rr}\dot{r}^2$ in Schwarzschild spacetime. The Schwarzschild metric describes the spacetime surrounding a spherical mass and have metric components $g_{tt} = -(1 - M/r)$, $g_{\theta\theta} = r^2$, $g_{\phi\phi} = r^2 \sin^2 \theta$ and $g_{rr} = (1 + M/r)^{-1}$. Here M represents the Schwarzschild radius ($M = \frac{2Gm_{object}}{c^2}$) of the gravitating object. We solved this set of equations analytically the assumptions that the motion is in the equatorial plane ($\theta = \pi/2$) and using the fact that for timelike particles $L = 1$ ($L = G = 1$).

$$\dot{r}(\phi) = \sqrt{-\frac{m^2}{l_z} r^4 + \frac{m^2}{l_z} Mr^3 - r^2 + Mr} = \sqrt{g(r)}, \quad (2.16)$$

where m , l_z and M represents the mass of the smaller companion (such as a neutron star), the angular momentum of the smaller companion and the Schwarzschild radius of central super massive black hole (such as Sgr A*). Solution of Eq. (2.16) was written in a numerical form for a binary containing SgrA* and a neutron star (Scharf, 2011)

$$r(\phi) = \frac{1}{4\xi(\phi, -19.72, 3.69) + \sqrt[3]{3}}. \quad (2.17)$$

Here we used Eq. (2.17) and assumed that $m=1.4M_{\odot}$, $M=1$ (in normalized units) and $l_z=1$ (in normalized units). Also ξ represents the Weierstrass function whose values can be found in tables of mathematical functions. Eq. (2.17) was evaluated numerically for $\phi \in \{0, 16\pi\}$ to produce the trajectory of a timelike particle (neutron star) around Sgr A* (in the center) represented by Fig. 2.4.

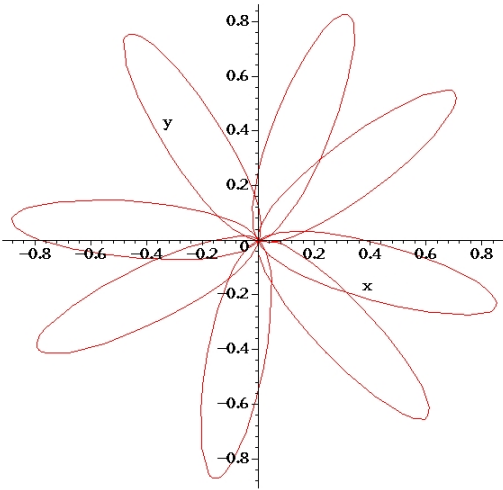


Fig. 2.4: The geodesic effect (precession) of the orbit of timelike particles (such as a neutron star) around a central massive object (such as Sgr A*) represented in normalized units (also known as extreme mass ratio inspirals). The same trajectory is also followed when a stellar black hole orbits a super massive galactic black hole.

This theory is also computationally cheap when compared to the full Numerical simulations, which occupy months of computational time (Reisswig et al, 2011). A schematic of the procedure followed for the rest of this thesis is presented Fig. 2.5.

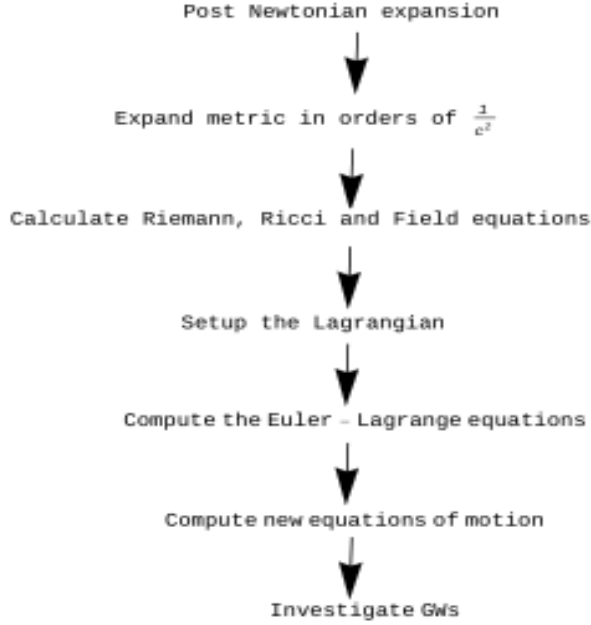


Fig. 2.5: A flow diagram of the PN theory.

The above schematic explains the methodology used in this section. Each step was symbolically tested with a MAPLE pipeline which we developed and which we will explain in following sections. If the metric is needed to an order higher than the Newtonian approximation, then the main process involves the expansion of the metric in orders of c^{-2} . These expansions will have a physical effect on the equations of motion (see Fig. 2.4).

The other component that contributes to the total Lagragian is the gravitational field (L_G).

Similar to the mass energy-momentum tensor T_μ^ν , there also exist a tensor for the gravitational field, T_μ^G . Calculating these tensors would contribute to the total stress tensor $T_\mu^\nu = T_\mu^G + T_\mu^M$. Petry (1979) showed that

$$L_G = -F(G)g_{\nu\mu}g_{\gamma\delta}\left(g^{\alpha\beta}g^{\nu\gamma}_{;\alpha}g^{\mu\delta}_{;\beta} + Lg^{\alpha\beta}g^{\nu\mu}_{;\alpha}g^{\gamma\delta}_{;\beta}\right). \quad (2.18)$$

The total Lagrangian is therefore (Petry, 1979)

$$L_0 = L_G + E\varphi L_M. \quad (2.19)$$

Here E and φ are both scaling constants. Using the conservation condition of

$$\frac{\partial}{\partial x^\alpha} \left(g^{\alpha\beta} \left(T_{\mu\beta}^G + T_{\mu\beta}^M \right) \right) = 0,$$

we solved the set of unknowns E, L, φ , and $F(G)$, which has a

solution of $E = 8, L = -0.5, \varphi = \frac{4\pi k}{c^4}$ and $F(G) = G^{0.5}$ (Petry, 1979). Then L_G becomes

$$L_G = -G^{0.5} g_{\nu\mu} g_{\gamma\delta} \left(g^{\alpha\beta} g^{\nu\gamma}_{;\alpha} g^{\mu\delta}_{;\beta} + 8g^{\alpha\beta} g^{\nu\mu}_{;\alpha} g^{\gamma\delta}_{;\beta} \right). \quad (2.20)$$

The corresponding gravitational tensor is

$$T_{\mu\nu}^G = \frac{1}{E\varphi} \left[F(G) g_{\nu\mu} g_{\gamma\delta} \left(g^{\nu\gamma}_{;\alpha} g^{\mu\delta}_{;\beta} + L g^{\nu\mu}_{;\alpha} g^{\gamma\delta}_{;\beta} \right) \right] + 0.5 g_{\mu\nu} L_G. \quad (2.21)$$

The mass energy momentum tensor obtained from GR is $T_{\mu\nu}^M = \rho g_{\mu\alpha} g_{\nu\beta} \frac{dx^\alpha}{d\tau} \frac{dx^\beta}{d\tau}$. The

next step will be to construct the field equations for this total stress tensor, $T_{\mu\nu} = T_{\mu\nu}^G + T_{\mu\nu}^M$.

It is also important to keep track of the fundamental quantities such as: $g = \det(g_{\mu\nu})$ and $\eta = \det(\eta_{\mu\nu})$. All of these components will be calculated in proceeding sections using a self-developed pipeline (it will also be consistently checked with the derivations done by Petry (1979, 1981 and 1992). The purpose of the program NEWSOR is to verify these equations and develop a symbolic metric based PN calculation toolkit. We wrote this program in MAPLE that uses its own tensor analysis package.

2.2.2 Calculating the metric, mass and gravity tensors with the use of NEWSOR

I developed a program called NEWSOR that performs tensor calculations in the framework of the Post Newtonian framework. The name NEWSOR was derived from a combination of the words “tensor” and “Newtonian”. The code is a MAPLE based pipeline that can perform tensor calculations in symbolic form. This is a self-developed pipeline and only uses MAPLE’s ability to construct a tensor object. The only restriction to the pipeline is the fact it requires the user to truncate the calculated terms to some order. The basic operation of the code is based on a one dimensional analysis in the

indices of the tensor. The program calculates $\left\{ \overset{M}{T}_i^i, \overset{G}{T}_i^i, \overset{M}{T}_0^i, \overset{G}{T}_0^i, \overset{M}{T}_j^0, \overset{G}{T}_j^0, G, dt/d\tau \right\}$. Then the

user can derive expressions for $\overset{M}{T}_1^1, \overset{M}{T}_2^2$, and $\overset{M}{T}_3^3$ etc. The operation of the code depends on the metric to the chosen PN order. Using the fact that $g_{00} \sim O(4)$, $g_{0j} \sim O(3)$ and

$g_{jk} \sim O(2)$; the order of the parameters v^2, P, ρ, U, Π and $\frac{P}{\rho}$ changes to $O(4)$ with

elements $v \sim O(2)$, $V_\mu(x^i, t) = k \int \frac{\rho(x^i, t) v^\mu(x^i, t)}{|x - x'|} dx^i \sim O(1)$ and $S \sim O(1)$ as calculated by

Petry (1979). The constant k represents the gravitational constant. In Petry (1979, 1981 and 1992) the PN metric was constructed

$$g_{\mu\nu} = \begin{bmatrix} \left(1 + \frac{2U}{c^2}\right)\delta_{\mu\nu} & 0 & 0 & -\frac{4V_\nu}{c^3} \\ 0 & \left(1 + \frac{2U}{c^2}\right)\delta_{\mu\nu} & 0 & -\frac{4V_\nu}{c^3} \\ 0 & 0 & \left(1 + \frac{2U}{c^2}\right)\delta_{\mu\nu} & -\frac{4V_\nu}{c^3} \\ -\frac{4V_\mu}{c^3} & -\frac{4V_\mu}{c^3} & -\frac{4V_\mu}{c^3} & -\left(1 - \frac{2U}{c^2} + \frac{S}{c^4}\right) \end{bmatrix}. \quad (2.22)$$

Having an inverse of

$$g^{\mu\nu} = \begin{bmatrix} \left(1 - \frac{2U}{c^2}\right)\delta_{\mu\nu} & 0 & 0 & -\frac{4V_\nu}{c^3} \\ 0 & \left(1 - \frac{2U}{c^2}\right)\delta_{\mu\nu} & 0 & -\frac{4V_\nu}{c^3} \\ 0 & 0 & \left(1 - \frac{2U}{c^2}\right)\delta_{\mu\nu} & -\frac{4V_\nu}{c^3} \\ -\frac{4V_\mu}{c^3} & -\frac{4V_\mu}{c^3} & -\frac{4V_\mu}{c^3} & -\left(1 + \frac{2U}{c^2} - \frac{S}{c^4}\right) \end{bmatrix}. \quad (2.23)$$

The following few pages contain output blocks from the program NEWSOR, generated by using the Post Newtonian metric which is approximated to the order c^{-2} . These modules are used to construct the tensor components to model GW emission using this approach.

Starting the program NEWSOR, the only input needed is the metric (Appendix C). After the metric was defined, some of the mass and gravity tensor components were determined.

From there, the formal total tensor, $T_{\mu\nu} = T_{\mu\nu}^G + T_{\mu\nu}^M$, see Appendix (C.6) and Appendix (C.7).

The tensors $T_{\mu\nu}^M$ and $T_{\mu\nu}^G$ were also explicitly calculated by Petry (1979, 1981 and 1992).

The velocity (v) in the expression should not be confused with the counter ν (in brackets on the right)).

$$\overset{M}{T}_{\mu}^{\nu} = \begin{cases} \rho v^{\mu} v^{\nu} + P c^2 \delta_{\mu\nu}, \text{ for } \{\mu = \nu = (1, 2, 3)\} \\ \rho c v^{\mu} \left(1 + \frac{\Pi}{c^2} + \frac{2U}{c^2} + \left(\frac{v}{c} \right)^2 + \frac{P}{\rho} \right), \text{ for } \{\mu = (1, 2, 3), \nu = 0\} \\ -\rho c v^{\nu} \left(1 + \frac{\Pi}{c^2} + \frac{6U}{c^2} + \left(\frac{v}{c} \right)^2 + \frac{P}{\rho} \right) + \frac{4}{c} \rho V_{\nu}, \text{ for } \{\nu = (1, 2, 3), \mu = 0\} \\ -\rho c^2 \left(1 + \frac{\Pi}{c^2} + \frac{2U}{c^2} + \left(\frac{v}{c} \right)^2 \right), \text{ for } \{\nu = 0, \mu = 0\} \end{cases}. \quad (2.24)$$

The scalar form of the mass tensor was determined by using the tensor transformation

$$\text{law } \overset{M}{T}_{\alpha}^{\alpha} = g^{\mu\alpha} g_{\alpha\nu} \overset{M}{T}_{\mu}^{\nu}$$

$$\overset{M}{T}_{\alpha}^{\alpha} = -\rho c^2 \left(1 + \frac{\Pi}{c^2} + \frac{2U}{c^2} - 3 \frac{P}{\rho} \right). \quad (2.25)$$

Extracting the results (the output blocks) produced by NEWSOR for the tensor $\overset{G}{T}_{\mu}^{\nu}$ we have

$$\overset{G}{T}_{\mu}^{\nu} = \left\{ \begin{array}{l} \frac{1}{\varphi c^4} \left(\frac{\partial U}{\partial x^\mu} \frac{\partial U}{\partial x^\nu} - \frac{1}{2} \delta_{\nu}^{\mu} \sum_{k=1}^3 \frac{\partial U}{\partial x^k} \frac{\partial U}{\partial x^k} \right), \text{ for } \{\mu = \nu = (1, 2, 3)\} \\ \\ \frac{1}{\varphi c^4} \frac{\partial U}{\partial x^\mu} \frac{\partial U}{\partial ct}, \text{ for } \{\mu = (1, 2, 3), \nu = 0\} \\ \\ -\frac{1}{\varphi c^4} \frac{\partial U}{\partial ct} \frac{\partial U}{\partial x^\nu}, \text{ for } \{\nu = (1, 2, 3), \mu = 0\} \\ \\ -\frac{1}{2\varphi c^4} \sum_{k=1}^3 \frac{\partial U}{\partial x^k} \frac{\partial U}{\partial x^k}, \text{ for } \{\nu = 0, \mu = 0\} \end{array} \right\}. \quad (2.26)$$

After having calculated both parts of the total tensor ($\overset{G}{T}_{\mu}^{\nu}$ and $\overset{M}{T}_{\mu}^{\nu}$) in this section, we then determined the energy loss due to GW radiation of a binary system (PSR913+16) within the PN framework. This will be illustrated in the next section.

2.2.3 Post Newtonian Gravitational Waves

The first thing that needs to be calculated is the symmetric metric $\left(f^{\mu\nu} = \begin{pmatrix} -g \\ -\eta \end{pmatrix} g^{\mu\nu} \right)$
 (Petry, 1979, 1981 and 1992)

$$f^{\mu\nu} = \begin{bmatrix} \delta_{\mu\nu} & 0 & 0 & -\frac{4V_\mu}{c^3} \\ 0 & \delta_{\mu\nu} & 0 & -\frac{4V_\mu}{c^3} \\ 0 & 0 & \delta_{\mu\nu} & -\frac{4V_\mu}{c^3} \\ -\frac{4V_\nu}{c^3} & -\frac{4V_\nu}{c^3} & -\frac{4V_\nu}{c^3} & -\left(1 + \frac{4U}{c^2}\right) \end{bmatrix} \quad (2.27)$$

Here $\eta = \det(\eta_{\mu\nu})$. The condition of a symmetric metric ($f^{\mu\nu}$) has its origin from the perturbation analysis ($g^{\mu\nu} = \eta^{\mu\nu} + h^{\mu\nu}$) in GR which mathematically produces GWs. This perturbation is performed on a symmetric tensor ($g^{\mu\nu}$), thus $f^{\mu\nu}$ also needs to be symmetric. Performing the perturbation ($f^{\mu\nu} = \eta^{\mu\nu} + \varsigma^{\mu\nu}$) through a process that is analogous to the metric perturbation of flatspace in GR, a well-known wave propagation tensor was produced by Petry (1979, 1981 and 1992)

$$\tau^{\mu\nu} = \eta^{\beta\alpha} \varsigma^{\mu\nu}_{;\beta;\alpha}. \quad (2.28)$$

The tensor $\varsigma^{\mu\nu}$ has identical characteristics to the perturbation metric ($h^{\mu\nu}$) in the GR analysis, with the well-known wave solution

$$\varsigma^{\mu\nu}(x, t) = -\frac{1}{4\pi} \int \frac{\tau^{\mu\nu}\left(x', t - \frac{|x' - x|}{c}\right)}{|x' - x|} d^3x'. \quad (2.29)$$

The connection between the tensors $\tau^{\mu\nu}$ and $\varsigma^{\mu\nu}$ was derived (Petry, 1992) by using the PN metric ($f^{\mu\nu}$) in the derivation of the PN equations for the gravitational field in flat space ($G_\nu^\mu = kT_\nu^\mu \rightarrow (f^{\beta\alpha} f_{\nu\gamma} f^{\gamma\mu}_{;\alpha})_{;\beta} = kT_\nu^\mu$). This connection was completed by introducing the substitution of $\tau^{\mu\nu}$ in the expanded form of $(f^{\beta\alpha} f_{\nu\gamma} f^{\gamma\mu}_{;\alpha})_{;\beta} = kT_\nu^\mu$, namely $(\tau^{\mu\nu} = -(\varsigma^{\beta\alpha} \varsigma^{\mu\nu}_{;\beta})_{;\alpha} + f^{\alpha\beta} f_{\varepsilon\delta} \varsigma^{\mu\varepsilon}_{;\alpha} \varsigma^{\nu\delta}_{;\beta} + 4kf^{\mu\alpha} T_\alpha^\nu)$. Here k is the gravitational constant. As in GR, one can derive an expression for the loss of energy due to GW emission from the system (also see Eq. 18 in Petry (1992))

$$\dot{E}_{GW} = c |x|^2 \int_{\Omega} T_0^i(|x| r, t) r^i d\Omega. \quad (2.30)$$

Here Ω corresponds the unit solid angle and $r^i = \frac{x^i}{|x|}$ is the unit separation vector.

The resultant energy loss rate (Petry, 1992) is

$$-\langle \dot{E} \rangle = \frac{4\kappa}{15c^5} \left\langle 3 \frac{\partial J^{ij}}{\partial t} \frac{\partial J^{ij}}{\partial t} - \left(\frac{\partial J^{ij}}{\partial t} \right)^2 \right\rangle. \quad (2.31)$$

Where $\kappa = \frac{4\pi k}{c^4}$ and $J^{ij} = \int \eta^{iv} T_v^j dx^i$.

This is a familiar result as predicted in the framework of GR. We also have that

$$n^i n^j D^2(Q^{ij}) = n^i n^j J^{ij}. \quad (2.32)$$

Then the equation for the energy loss due to GW radiation is

$$\langle \dot{E}_{GW} \rangle = -\frac{\kappa}{15c^5} \left\langle 3 \frac{\partial}{\partial t} \left(\frac{\partial^2 Q^{ij}}{\partial (ct)^2} \right) \frac{\partial}{\partial t} \left(\frac{\partial^2 Q^{ij}}{\partial (ct)^2} \right) - \left(\frac{\partial}{\partial t} \left(\frac{\partial^2 Q^{ii}}{\partial (ct)^2} \right) \right)^2 \right\rangle. \quad (2.33)$$

To convert the problem to an N-body system, the quadrupole tensor needs to be handled in an N-body framework (Petry, 1992)

$$\frac{\partial^2 Q^{ij}}{\partial (ct)^2} = \frac{\partial^2}{\partial (ct)^2} \sum_N m_N x_N^i x_N^j = \sum_N m_N \left(2v_N^i v_N^j + \dot{v}_N^i x_N^j + x_N^i \dot{v}_N^j \right). \quad (2.34)$$

For a binary system (such as two neutron stars) it is known that $N=2$. Using the standard two body framework (with $\psi = x_2 - x_1$, $\zeta = v_2 - v_1$, $\epsilon = m_1 m_2 / (m_1 + m_2)$ and $m = m_2 + m_1$), it follows that

$$\frac{\partial^2 Q^{ij}}{\partial(ct)^2} = \varepsilon \left(2\zeta^i \zeta^j + \dot{\zeta}^i \psi^j + \psi^i \dot{\zeta}^j \right). \quad (2.35)$$

Using the Newton's law of Universal gravity $\left(a = \dot{\zeta}^i = \dot{v} = km \bigg/ r \middle| r^3 \right)$, the familiar GR result for binary systems was obtained (Petry, 1992)

$$\dot{E}_{GW} = -\frac{8}{15} \frac{k^3 \varepsilon^2 m^2}{c^5 r^4} (12 |v|^2 - 11 \dot{r}^2). \quad (2.36)$$

For the GW energy radiated from a binary system, the same results will be obtained for the Hulse-Taylor pulsar when considering the post Newtonian Theory against the General Theory of Relativity. NEWSOR also proved to be a helpful tool for calculating the necessary PN elements and tensors. These were calculated in a manner similar to that of Petry (1979, 1981 and 1992).

In this chapter only a very brief description was presented of the manner in which the properties of GWs are treated mathematically within the Einstein quadrupole and Post Newtonian (PN) formalisms. In the next chapter a more quantitative discussion of the GW signatures of several classes of astrophysical sources will be presented.

Chapter 3

LIGO Sources of Gravitational Waves within the quadrupole formalism and the Post Newtonian (PN) approximations

In this chapter a brief discussion will be presented of the various classes of LIGO GW signatures presented using the quadrupole and Post Newtonian approximations. As mentioned earlier the AdvLIGO detector will probably be sensitive to the high frequency end of the GW emission between 3-3000 Hz, with strain amplitudes between $h \sim 10^{-21} - 10^{-20}$.

3.1 Introduction to LIGO sources

GWs are emitted when non-spherical mass distributions are accelerated in spacetime such as collapsing or spinning stars). Chandrasekhar (1970a and 1970b) investigated GWs from mathematical spinning objects to investigate instabilities and unique signatures. He described analytically certain natural instabilities occurring in spinning massive stars. Each rigid spinning source is characterized by a spin-down time (the time during which gravitational waves and other forms of radiation are emitted until all the irregularities and deformations are radiated away). These spinning dynamics directly influence the GW signatures (just after birth of the astrophysical source) and influence the detectability of these sources by ground based interferometers such as LIGO. The frequency detection window of AdvLIGO spans several hertz to kilohertz (see Chapter 1); this window includes rapidly spinning and core collapsing objects that have dynamical time scales of the order of milliseconds.

Astrophysical objects that could be observed with LIGO include: spinning neutron stars, supernovae core collapse events, rotating deformed magnetars, and coalescing binary neutron star systems or binary black hole systems. All of these objects are classified as transient events (Anderson et al., 2013); see Fig 3.1 for examples of astrophysical objects that could emit LIGO detectable GWs.

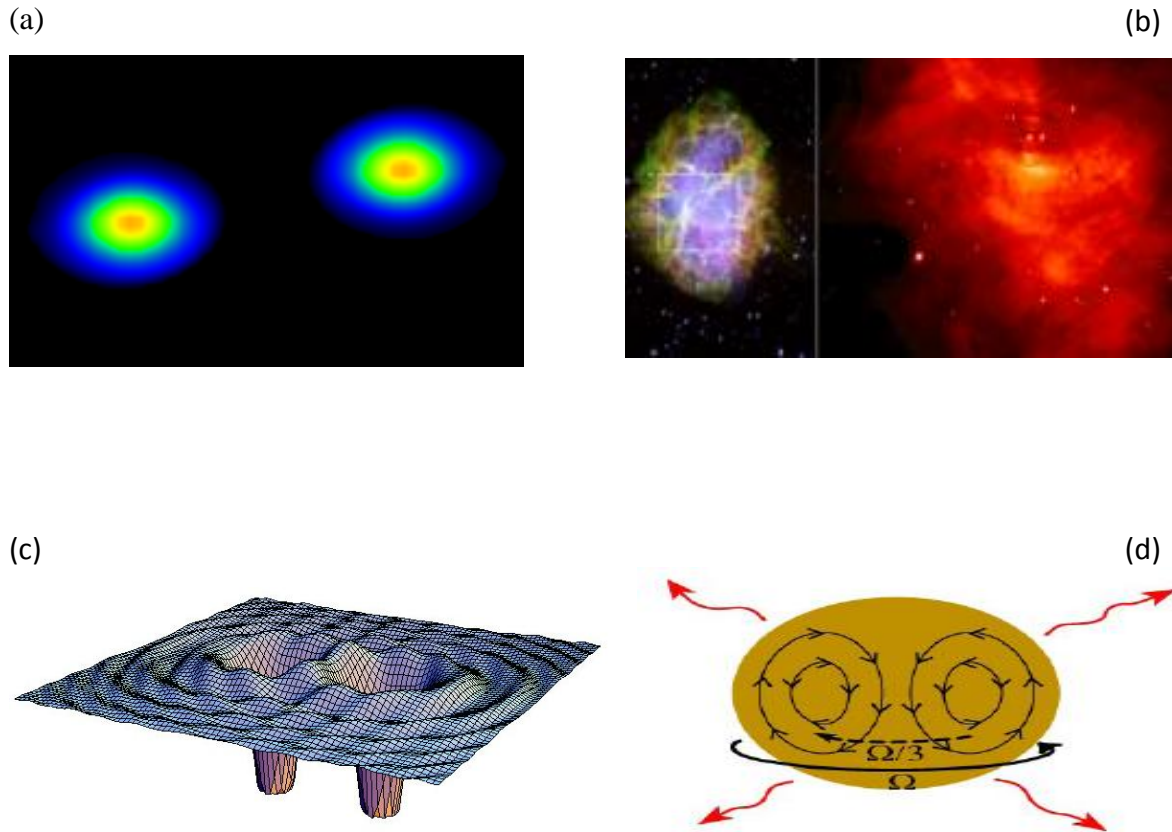


Fig 3.1: (a) Simulation of the merging of two neutron stars (b) Supernovae events (Crab Nebula) as seen by Hubble and Chandra (X-ray) (c) A merging binary black hole system (d) Young rotating neutron star objects with internal magnetic fields that deforms the star (Adapted from Fryer et al., 2011).

Each of these events can produce GW signatures with distinguishable frequencies and amplitudes (see Table 3.1 for a summary of the GW signatures produced by several exotic binary mergers). These compact objects are considered to be the prime transient

targets for ground based (terrestrial) interferometers and are contained in the high frequency (3-3000 Hz) part of Fig 3.2 that represents the sensitivity curve of the LIGO GW detector.

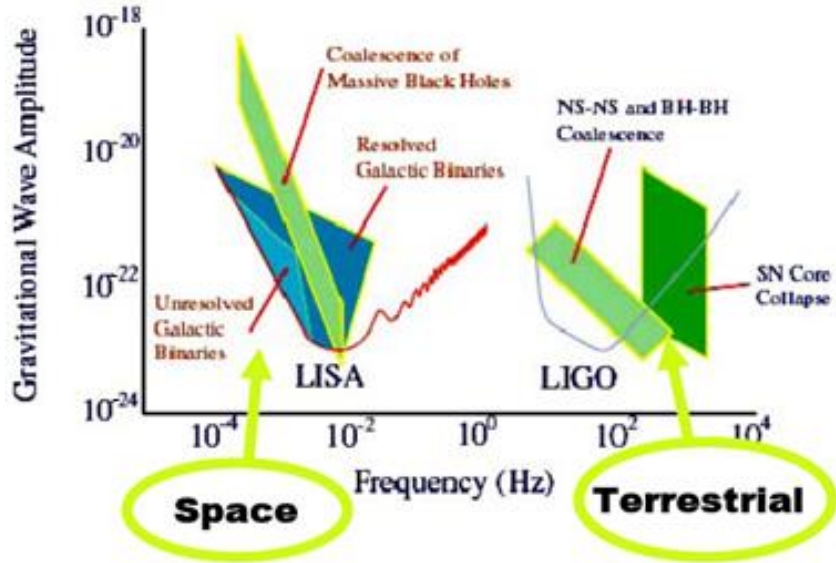


Fig 3.2: Typical GW strains produced by the above mentioned LIGO sources (see the frequency window 3-3000 Hz); the graph does not include the Advanced LIGO sensitivities. AdvLIGO will be in the testing phase in a few years (from Fryer et al., 2011). See Fig 1.9 (a,b) in Chapter 1 for additional supporting sensitivity diagrams.

Table 3.1: GW signature summary of the galactic binary compact transient sources (Adapted from Anderson et al., 2013)

Source	Mass distribution (M_{\odot})	Peak GW emission times scales (t)	GW amplitude(h)
NS-NS	$1.4 M_{\odot}$	days-ms	$h > 10^{-21}$
NS-BH	$1.4 M_{\odot}$	days-ms	$h > 10^{-21}$
BH-BH	$10^6 M_{\odot}$	days-ms	$h < 10^{-21}$
SN core collapse	$1.6 M_{\odot}$	ms	$h > 10^{-21}$
Spinning objects	$1.4 M_{\odot}$	ms	$h > 10^{-21}$

Fig. 3.2 differs from Fig. 1.7 (Chapter 1) is that the GW signature is characterized by GW amplitude (A) in Fig. 3.2 (on the y-axis), while it is characterized by amplitude (or power) spectral density (ASD) with units ($h \text{ Hz}^{-0.5}$) on the y-axis in Fig. 1.7, since it represents the amplitude (or the GW signal power) per frequency bin. AdvLIGO could make GW detection from these galactic sources a routine occurrence.

The majority of the numerical work done in the LIGO scientific collaboration (LSC) consists of the production of GW signature templates. Analytical studies are also being done in the field of GW source modeling and instrument optimization. There exist several numerical codes for solving problems in General Relativity or the N-Body framework. These codes include: GADGET, VULCAN2D, WHISKY, 1DGR and CACTUS (see Dimmelmeier et al. (2010) for a GR code overview). These simulation platforms can predict in great detail the evolution of certain astrophysical events (such as Supernova evolution and compact binary merging events). These codes also allow the users to generate the GW strain spectra (GW amplitude evolution spectra). See Fig. 3.3 and Fig. 3.4 for examples of GW signatures produced by these codes. Fig. 3.3 illustrates the GW signatures that are associated with supernovae (SN) core bounce (the characteristic burst GW signature). Fig. 3.4 illustrates various code outputs of binary merging events (Hydrodynamical) and core bounce SN GW signatures. Both GW signatures illustrated in Fig. 3.3 and Fig. 3.4(a), were produced by full General Relativistic codes (Dimmelmeier et al., 2002). Fig. 3.3 illustrates a core collapse GW signature (with adiabatic index $\gamma = \frac{4}{3}$ and density $\rho = 10^{14} \text{ g cm}^{-3}$) and Fig. 3.4(a) illustrates core collapse GW signatures (where model $A_1B_3G_1$ is associated with an adiabatic index $\gamma = 1.325$ and model $A_1B_3G_2$ with an adiabatic index $\gamma = 1.320$). The amplitude (A_{20}^{E2}) of the GW signature illustrated in Fig. 3.3 and Fig. 3.4 is the quadrupole GW amplitude.

Investigating these GW signatures prior to any modeling attempt proves useful when deciding what initial model parameters to use and what the simulation timescales will be in the simulation/model; this helps when searching for GW signatures in the data that will be predicted by the various models.

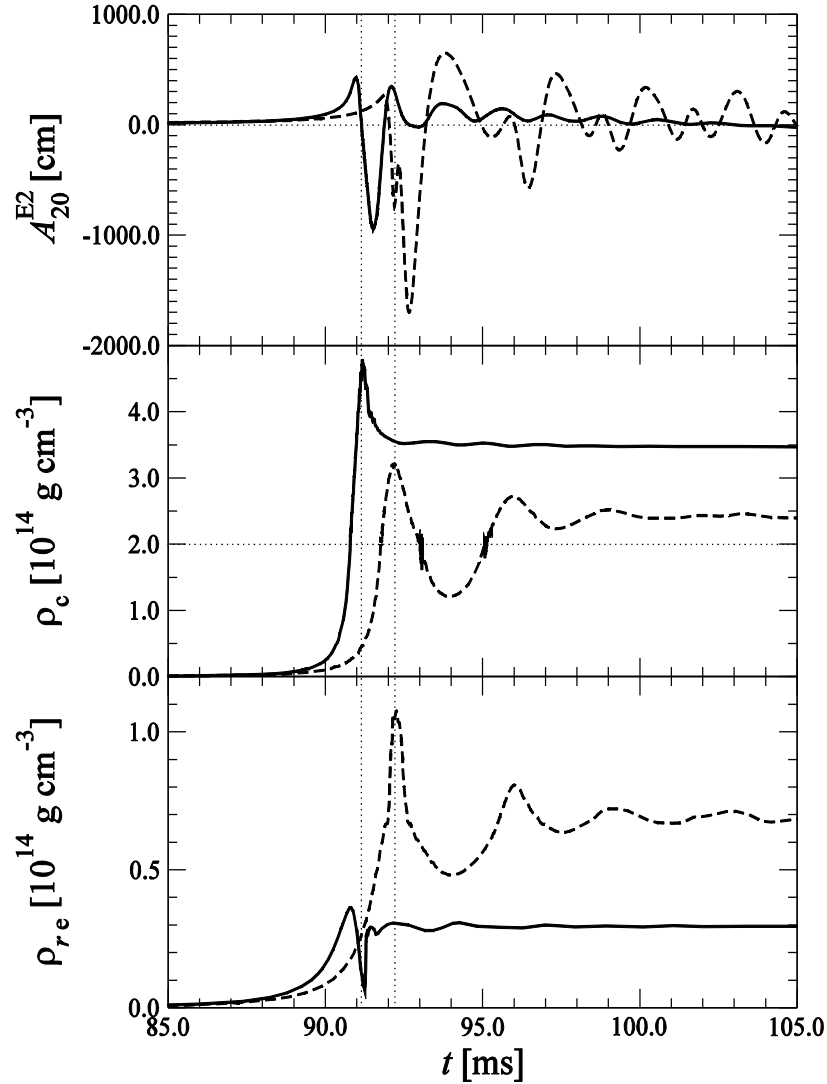


Fig. 3.3: Supernovae core bounce models produced by Dimmelmeier et al. (2002), clearly showing the core collapsing (at $t \sim 93$ ms) and then producing unique GW signals. This is a full relativistic (GR) simulation. The quantity A_{20}^{E2} represents the amplitude of the GW. The dashed line represents the GW signature produced by Newtonian codes; it is evident that both the GR and the Newtonian GW signatures are different from one another, but contain a unique characteristic core bounce signature (at $t \sim 93$ ms).

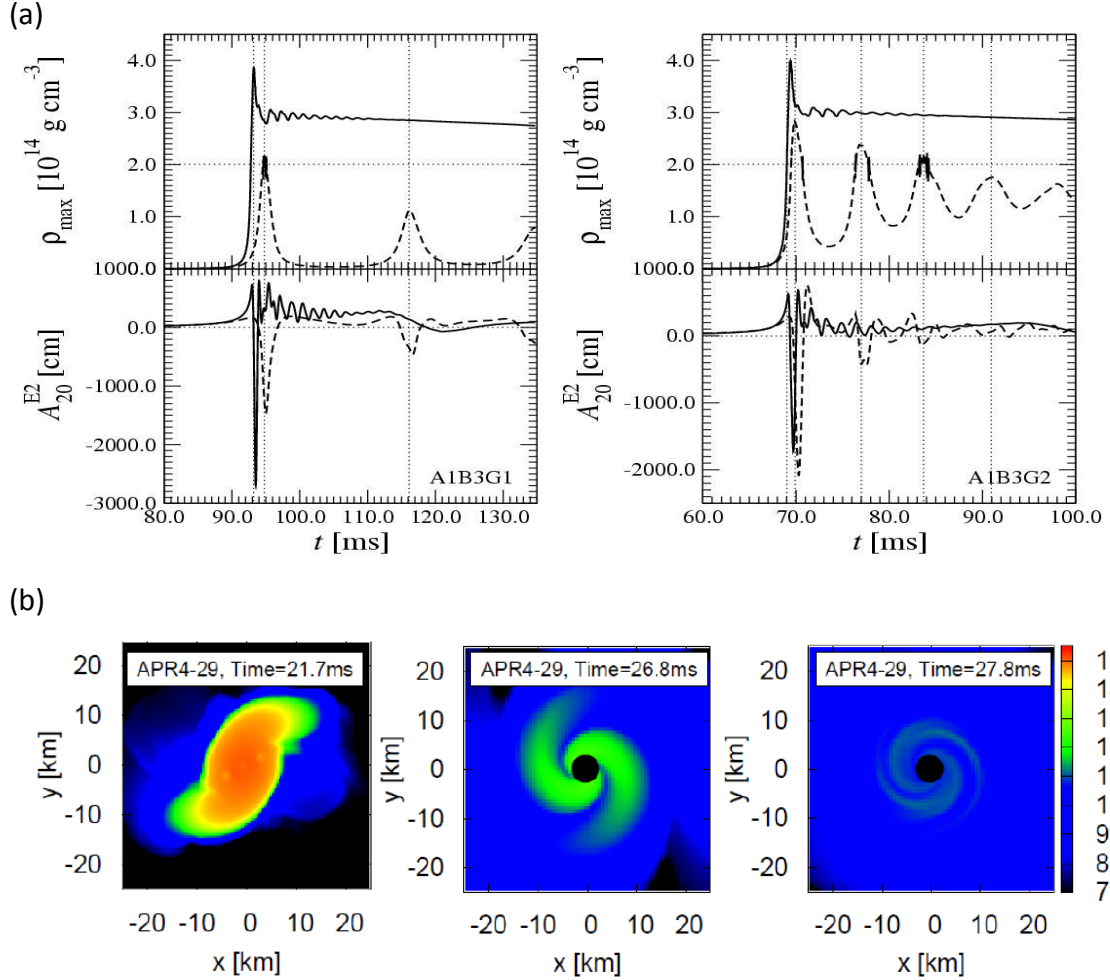


Fig. 3.4 (a,b): (a) Core bounce simulation using the Vulcan2D code (from Dimmelmeier et al., 2002), the dashed line represents the Newtonian GW signature. (b) the simulation of merging neutron stars forming either a black hole (at $t=27.8$ ms) or a Hyper Massive Neutron Star (HMNS) (at $t = 21.7$ ms) (from Hotokezaka, 2011).

Both Fig. 3.3 and Fig. 3.4(a,b) reveal useful information (in the GW signatures) in the way that if one wishes to compute upper limits of GW signatures for SN core bounce events (or merging binary neutron stars), one could construct Newtonian models that could produce approximated GW signatures for various GW sources. Full GR codes are needed to obtain high accuracy GW signatures of SN core bounce and merging events. Accordingly the following sections will focus on the process of obtaining GW signatures for various galactic sources using Newtonian methods.

The remainder of this chapter will focus on the different transient sources that produce oscillating and bursts of GWs. This will be done by considering the characteristic timescales on which GW radiation is emitted and how the frequency of the signal changes over time. Most of the analysis is based on the derivation of the transverse-traceless ($h_{ij}^{TT} = C\hat{Q}_{ij}$) part of the metric perturbation (specifically for collapsing cores and rotating objects), obtained using the quadrupole formalism (see Chapter 2 and Appendix A). All our models will be accompanied by several algorithms that we developed to will perform all the necessary calculations.

3.2 Supernovae core bounce

If a star with mass ($M > 8 - 10M_\odot$) burns up all its fuel; the gravitational force over powers the nuclear force in the core and a dramatic collapse quickly follows (Anderson et al., 2013) resulting in a dramatic explosion whereby the outer envelope of the star is blown away into space, see Fig 3.5 for examples of SNs. The final outcome of this process could be the formation of neutron stars or black holes (compact remnants). One of the GW producing mechanisms of supernovae is the core collapsing bounce phase. GWs will be emitted during the collapse due to the core's changing quadrupole moment (see Table 3.2 for a summary of the SN core collapse process and the associated change of the quadrupole tensor at various time steps in the collapse process). The bounce phase occurs on a dynamical timescale of the order of milliseconds. Initial rotational energy in the progenitor core could extend the collapse by a few milliseconds. The final GW signature is strongly influenced by the initial progenitor star's mass distribution deformations in the structure of the core, the total bounce timescale and the initial rotational energy of the core (see Table 3.2 and Fig. 3.6).

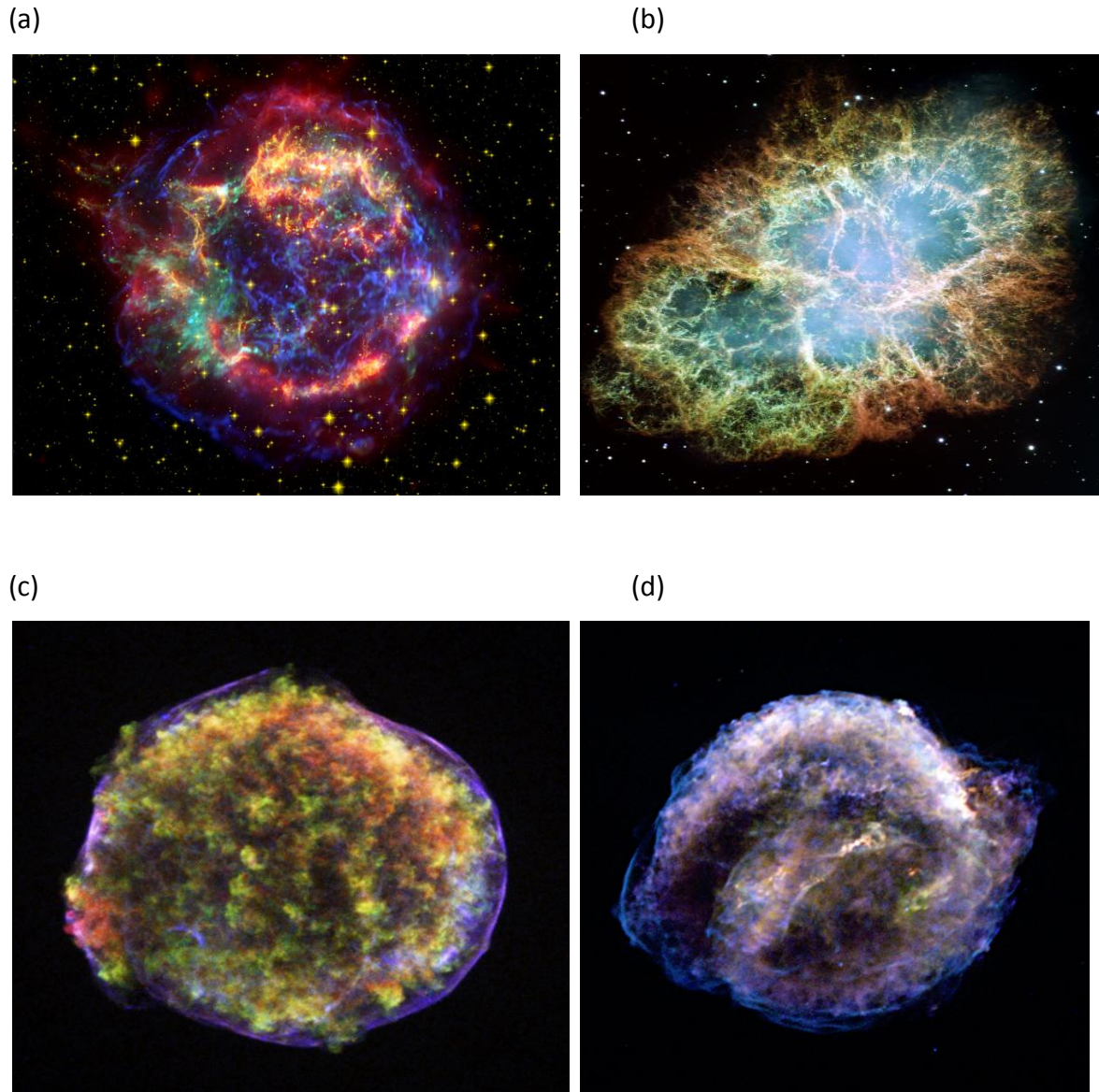


Fig. 3.5: (a) Cas A (Chandra/Spitzer/HST) (b) Crab (Chandra/Spitzer/HST) (c) Tycho's SN 1572 (Chandra and Spitzer) (d) Kepler's SN 1604 (Chandra) (Christian Ott, CGWAS 2013).

Table 3.2: Summary of the evolution of the quadrupole tensor associated with core collapse supernovae (from Anderson et al., 2013).

Event	Time scale	$ \Delta I_{jk} $
Core collapse	100 - 250 (ms)	increase
Shrinking in size	next 20 ms	decrease
Core bounce (nuclear pressure)	< 1 ms	Increase rapidly (Epoch of GW production)

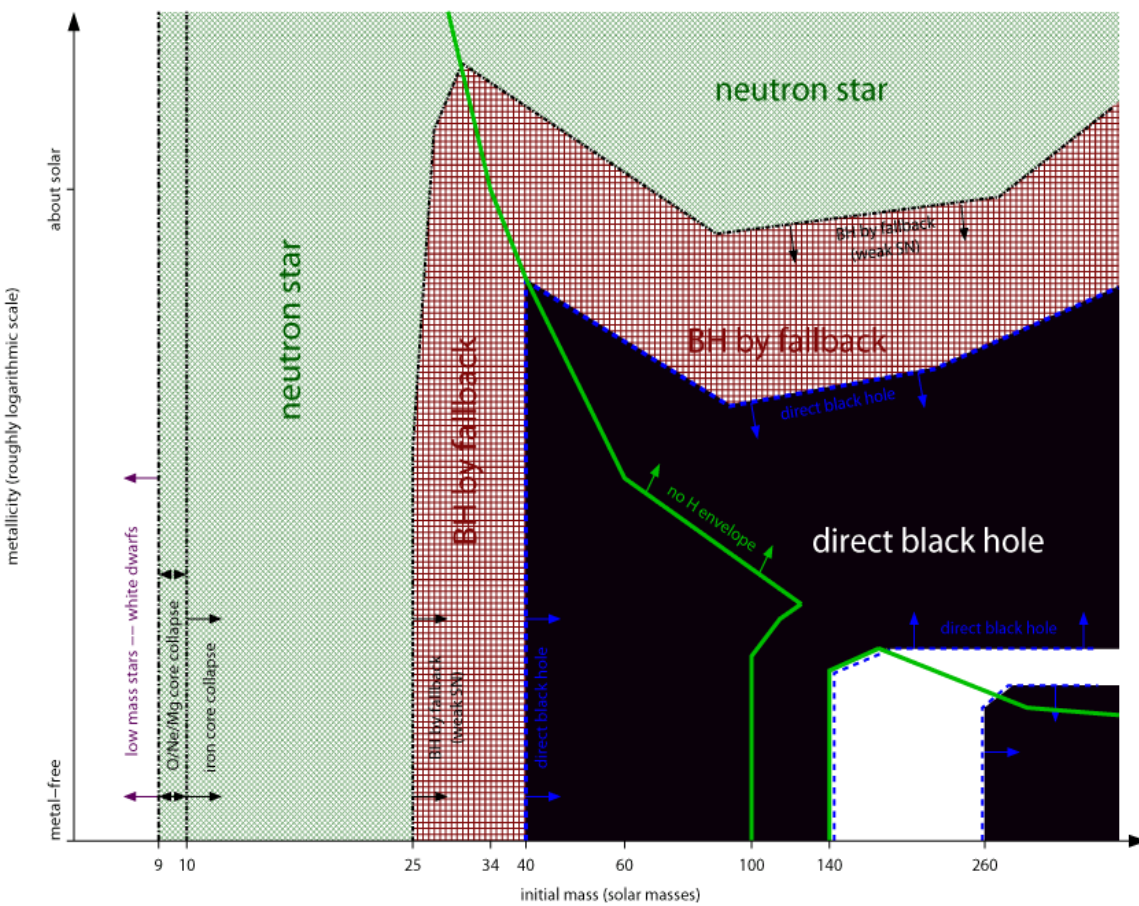


Fig. 3.6: Different progenitor stars collapsing and evolving into different compact remnants (from Fryer, 2011).

Fig. 3.6 illustrates possible outcomes of progenitor stars with different masses and metallicity; we are interested in the relation between the progenitor mass and the different compact objects that could be formed. Fig. 3.6 will prove helpful in later sections when we attempt to simulate core collapse SNe using different progenitor models, thus initial conditions for collapsing SN.

After the core collapse phase neutrino driven convection and shock formation (or perhaps an alternative mechanism such as rotational or magneto-rotational instability) generates enough energy to blow away the star's envelope in a beautiful display of power and brilliant colours (see Fig. 3.5). This explosion results in the birth of a compact object that might emit GWs that are detectable by LIGO (see Fig. 1.7 in Chapter 1). In this subsection, we focus on the GW signature produced by the bounce phase of core collapse supernovae; we will also provide motivation as to why LIGO must be included in the global network of detector systems together with GRB, neutrino and optical detectors. LIGO will be focusing on the detection of GW from compact objects which are remnants of SN events. See Fig. 3.7 for a mind map of what a multi-messenger network entails. Also, see Fig 3.8 for a detailed collapse of a $10M_{\odot}$ progenitor star; the collapse suggests that convection occurs at time $t > 500$ ms (Fryer, 2011).

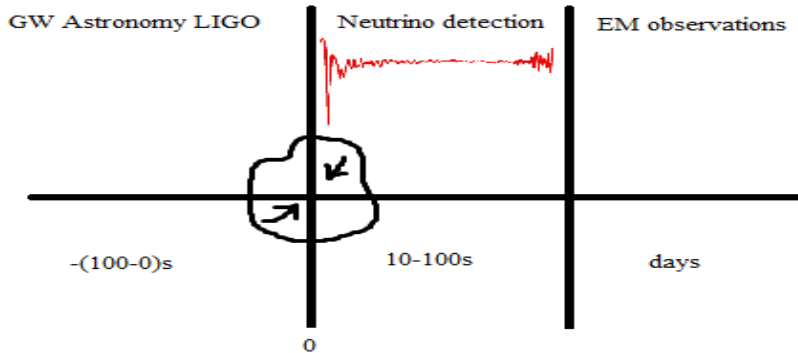


Fig. 3.7: LIGO's place in the global detector network system. Core bounce acts as the “unseen” trigger that should be detectable by GW ground based interferometers. This should be followed by neutrino and electromagnetic observations. LIGO could trigger the SKA to perform follow up radio observations and source localization.

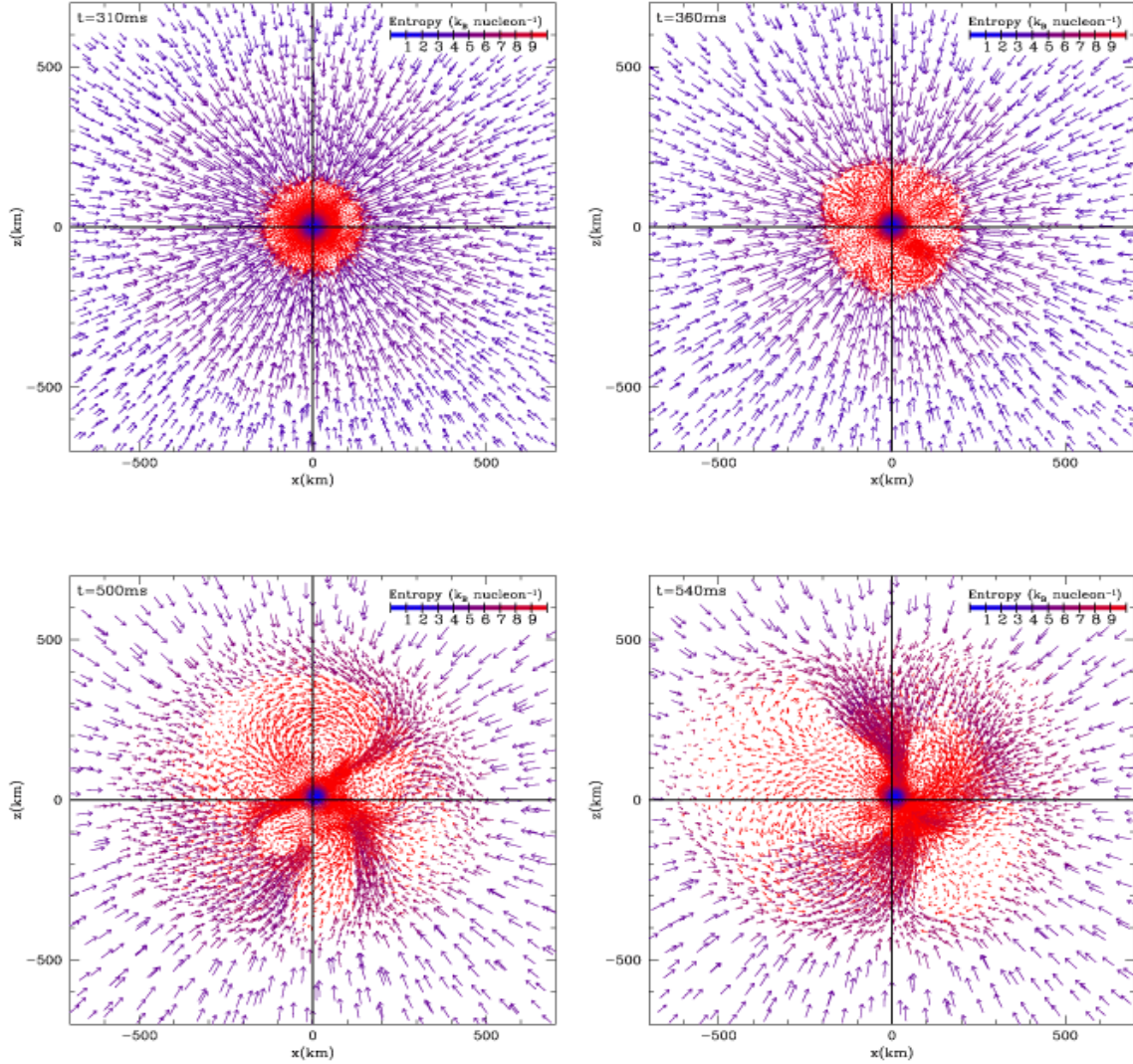


Fig. 3.8: (Top left) Induced core collapsed at $t = 310$ ms , (Bottom right) at $t \sim 500$ ms convection starts the explosion that will fatally blow away the core's envelope (from Fryer, 2011). From the point of view of GW astronomy, both the core bounce phase and the convection phase are expected to produce detectable GW signatures.

To investigate the evolution of the density profile associated with the core of a collapsing star, we simulated (using a GR code called “1DGR”) the collapse of two different progenitor stars (one with mass of $15M_\odot$ and the other with mass of $75M_\odot$) to investigate the possibility of forming either neutron stars or black holes as compact SN remnants. The results of this simulation are illustrated in Fig. 3.9 and Fig. 3.10.

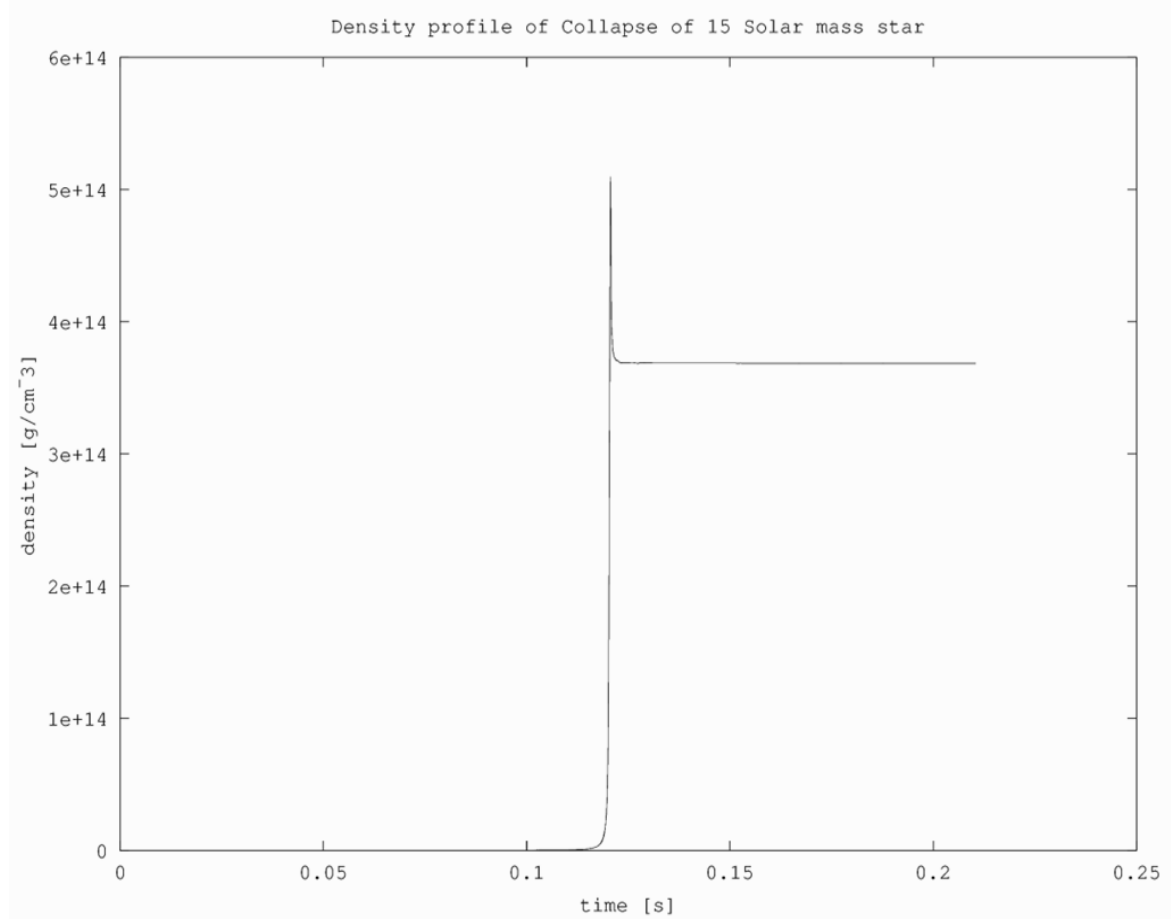


Fig 3.9: A General Relativistic core collapse density profile of a $M = 15M_{\odot}$ star produced with the 1DGR code (used during CGWAS 2013). According to this code, a stable compact remnant is formed.

Both density profiles illustrated in Fig. 3.9 and Fig. 3.10 have unique core bounce signatures at $t > 0.1 \text{ s}$. This prominent signature in the density evolution of the collapsing core could produce well-defined GW signatures at the time of SN core bounce. A stable remnant is formed in Fig. 3.9 since the density profile remains stable. Fig. 3.10 illustrates the collapse of a core into a stellar ($10 M_{\odot}$) black hole since the density profile increases to infinity after core bounce.

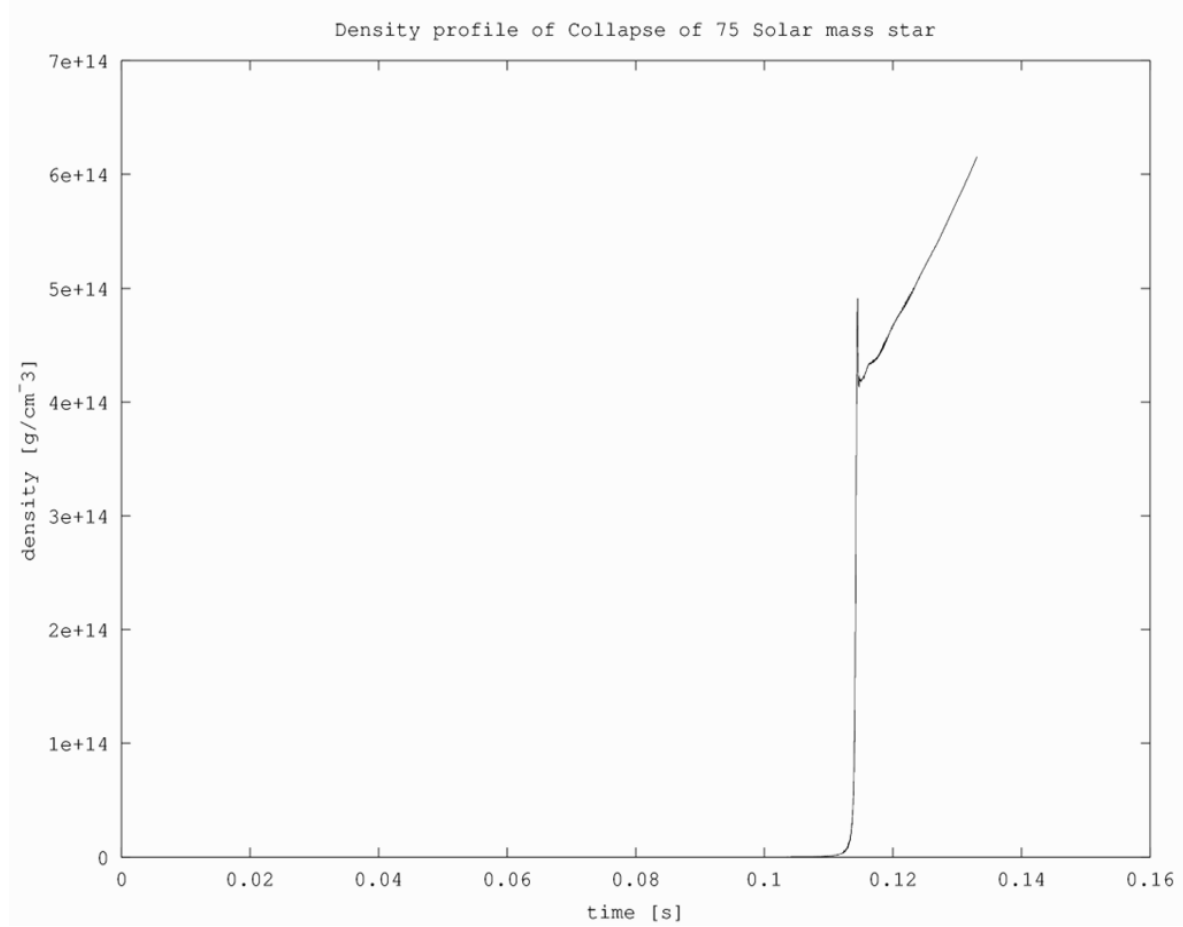


Fig. 3.10: A General Relativistic core collapse density profile of a $M = 75M_{\odot}$ star produced with the 1DGR code (used during CGWAS 2013). The collapse is followed by prompt black hole formation (represented by the increasing density profile, which increases to infinity as the singularity forms).

Mechanisms for possible GW emission in core collapse systems include: neutrino mechanisms that cause instabilities, magnetorotational mechanisms that influence the dynamics of the collapsing rotating core (which amplifies the magnetic field) and the acoustic mechanisms that excite pulsations in the rotating core which could produce recognizable GW signatures (Anderson et al., 2013). The supernovae rate in a Milky-Way-sized galaxy is $\sim SN / (30 - 50)$ years (Fryer, 2011), which proves exiting for future GW detectors. The mechanism that drives the core collapse GW emission is the rapidly

changing quadrupole moment (\ddot{Q}_{ij}). The changes are produced by the changing mass distribution (see Chapter 2). The end product of the collapse scales very sensitively to the initial conditions of the progenitor star; these conditions include: core mass, core rotation and the equation of state (EOS) of the star.

There are several theoretical methods for deriving the amplitude of GWs produced by such galactic events. These include: multipole expansion of the metric perturbation or the mass distribution and the classic 2-body explosion method (Alder, 1975). This section implements the methods proposed by Thorne (1978), implemented by Muller (1991). Which are based on the multipole expansions of the GW amplitude by Wagoner (1977). Muller (1991) implemented these formulations in the form of hydro-dynamical simulations of supernovae. The basis for the Thorne (1978) approach is the transverse-traceless part of the perturbation of the metric that characterizes the GW radiation completely, written in a compact form (Misner, Thorne and Wheeler (MTW), 1970)

$$h_{jk}^{TT} = r^{-1} A_{jk}(t-r, \theta, \phi). \quad (3.1)$$

Here h_{jk}^{TT} is the strain of the wave in the TT gauge, which is symmetric and time dependent. Indices used here are $i, j, k, l, m \in \{1, 2, 3\}$. The amplitude A_{jk} has an angular dependence and is decoupled from this dependence by using spherical harmonics T_{lm}^{E2} and T_{lm}^{B2} . These spherical harmonics represent the angular portion of a set of solutions to Laplace's equation. Ideally the perturbation can be represented in the following way (see Chapter 2 Eq. (2.6) for the general multipole expansion)

$$h^{TT} = r^{-1} \sum_l \sum_m \left\{ A_{lm}^{E2}(t-r) T_{lm}^{E2}(\theta, \phi) + T_{lm}^{B2}(\theta, \phi) A_{lm}^{B2}(t-r) \right\}. \quad (3.2)$$

The spherical harmonics allows the solution to be evaluated in spherical coordinates. The multipole amplitudes A_{lm}^{E2} and A_{lm}^{B2} were obtained by Wagoner (1977) and the first non-

zero terms that appear in the expansion are the quadrupole terms A_{20}^{E2} and A_{30}^{B2} . After constructing a sphere with radius r and Newtonian parameters ρ and v^ϕ representing the mass density distribution and the Eulerian velocity field, Muller (1991) constructed the following quantities

$$\begin{aligned} M_{20}^{E2} &= \frac{32\pi^{\frac{3}{2}}}{\sqrt{15}} \int_0^\infty \int_0^\infty \rho(r, x, t) \left(\frac{3}{2}x^2 - 1 \right) r^4 dr dx \\ M_{30}^{B2} &= \frac{8\pi^{\frac{3}{2}}}{\sqrt{105}} \int_0^\infty \int_0^\infty v^\phi \rho(r, x, t) (1-x^2)^{0.5} (5x^2 - 1) r^2 dr dx. \end{aligned} \quad (3.3)$$

The data needed for the calculation of these quantities were obtained directly through the hydro-dynamical simulations of the supernovae collapse event and represent quantities that are nothing other than the numerically defined quadrupole (M_{20}^{E2}) and octopole moments (M_{30}^{B2}) (other numerical quadrupole moments will be defined in Chapter 4).

Muller (1991) showed that these quantities determine the amplitudes A_{20}^{E2} and A_{30}^{B2}

$$\begin{aligned} A_{20}^{E2} &= \frac{d^2}{dt^2} M_{20}^{E2} \equiv \frac{d^2}{dt^2} Q_{numerical}^{ij} \\ A_{30}^{B2} &= \frac{d^3}{dt^3} M_{30}^{B2}. \end{aligned} \quad (3.4)$$

The components of h^{TT} are given by

$$h_{\theta\theta}^{TT} = \left(\sqrt{15} \sin^2 \theta A_{20}^{E2} \right) / 8\sqrt{\pi} d. \quad (3.5)$$

Here d is the distance to the source and the transverse traceless part of the strain has the symmetry of $-h_{\theta\theta}^{TT} = h_{\phi\phi}^{TT}$. All that remains is to calculate the equations for the energy

carried away by the GWs. Knowing that the power radiated (see Appendix A) by GWs scales with the change in the Quadrupole moment (or the second derivative of the strain)

$$\langle \dot{E}_{GW} \rangle \sim C \langle \ddot{h}_{TT}^{ij} \ddot{h}_{ij}^{TT} \rangle, \quad (3.6)$$

Or by using the amplitudes A_{20}^{E2} and A_{30}^{B2}

$$\dot{E}_{GW} = \frac{c^3}{32\pi G} \sum_{l,m} \int \left\{ \left| \frac{dA_{lm}^{E2}}{dt} \right|^2 + \left| \frac{dA_{lm}^{B2}}{dt} \right|^2 \right\} dt. \quad (3.7)$$

Transforming to the Fourier space (Muller, 1991),

$$\frac{d\dot{E}_{GW}}{d\omega} = \frac{c^3}{16\pi G} \sum_{l,m} \left(|A_{lm}^{E2}(\omega)|^2 + |A_{lm}^{B2}(\omega)|^2 \right) \omega^2. \quad (3.8)$$

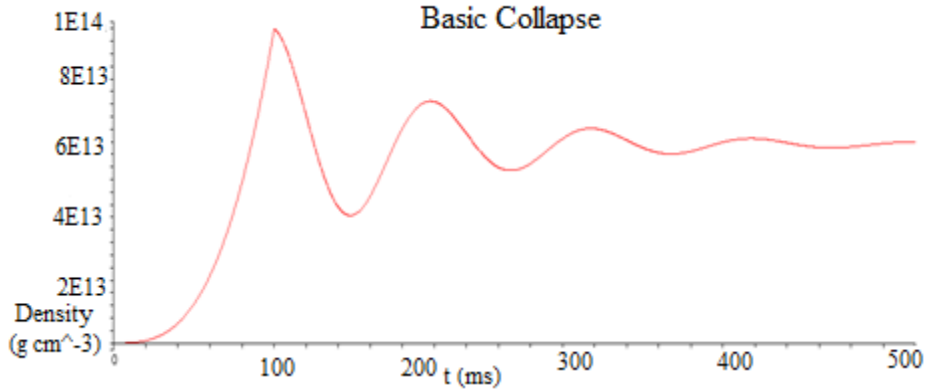
Here $|A_{lm}^{E2}(\omega)| = \int A_{lm}^{E2}(t) e^{i\omega t} dt$.

To test Eqs. (3.4) - (3.8), we investigated a case study in which we engineered the density function for such a core collapse was engineered (see Fig 3.11 (a,b)). We used the density function

$$\rho(g.cm^{-3}) = \begin{cases} 10^{14} t^3, & t < 1\text{ms} \\ 10^{14} \exp(-t) \cos(2\pi t), & t > 1\text{ms} \end{cases}. \quad (3.9)$$

This resulted in the following density profiles,

(a)



(b)

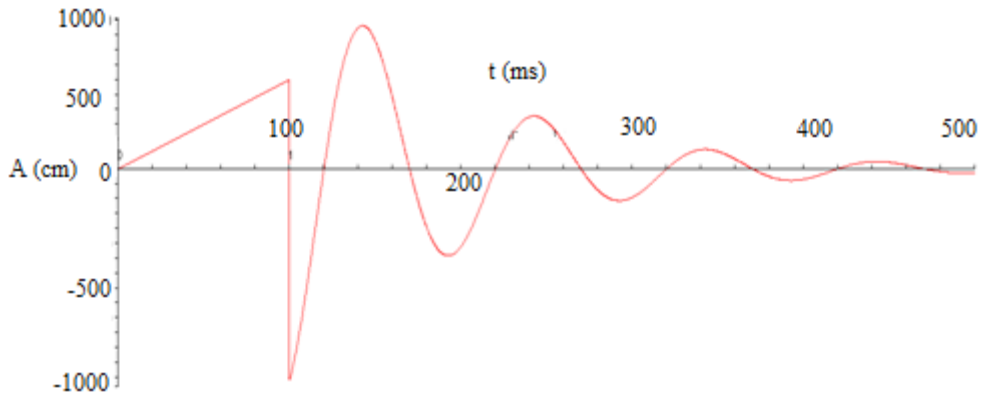


Fig. 3.11 (a,b): Basic engineered collapse: assume a density profile for a supernovae core collapse, and generate the GW amplitude associated with this event. Only the quadrupole amplitude was used for the calculation. The signature consists of a prominent bounce and ringing phase.

Fig. 3.11 shows that the bounce interval lasts for $t \sim 50$ ms and the corresponding GW amplitude was $A \sim 1500$ cm. The power output is $\dot{E} \sim 10^{44}$ erg s $^{-1}$ (which is $\sim 10^{-9}$ % of the total rest-mass energy of a $1M_{\odot}$ star) and generates (at a distance of 2 kPc), it generates a strain of (Muller, 1991)

$$\begin{aligned}
h &\sim 8.8 \times 10^{-21} \left(\frac{A_{20}^{E2}}{1000 \text{ cm}} \right) \left(\frac{10kPc}{d} \right) \\
&\sim 5 \times 10^{-20} \left(\frac{A_{20}^{E2}}{1000 \text{ cm}} \right) \left(\frac{d}{2 \text{ kPc}} \right)^{-1}.
\end{aligned} \tag{3.10}$$

To predict an upper limit for the output of GW power from supernovae core bounce, we developed a signal extraction algorithm to retrieve the GW signature. We used the data set obtained numerically by (Muller, 1991) using hydro-dynamical simulations of collapsing stars to test the algorithm. See Model B in Table 3.3 (Muller, 1991). This will be detectable with AdvLIGO for all frequencies less than 1000 Hz.

Table 3.3: Stellar models for supernovae and the GW amplitude produced by each collapse (from Muller, 1991). We used this table to decide what initial conditions to use to model SN core collapse.

Model		A	B	C	D
ρ_c^b	$[10^{14} \text{ gcm}^{-3}]$	2.57	0.36	2.11	1.51
ρ_c^{eq}	$[10^{14} \text{ gcm}^{-3}]$	2.10	0.21	1.30	0.75
M_{ic}^b	$[\text{M}_\odot]$	0.97	1.12	1.01	1.02
K_{ic}^b	$[10^{51} \text{ erg}]$	3.3	0.7	2.1	1.7
E_{rot}^{eq}	$[10^{51} \text{ erg}]$	9.3	7.3	8.3	6.5
$E_{rot}^{eq,ic}$	$[10^{51} \text{ erg}]$	6.5	5.2	7.0	5.3
β^{eq}		0.085	0.140	0.094	0.096
T_{osc}^I	[ms]	3.1	15.0	4.9	14.0
T_{osc}^{II}	[ms]	2.5	10.0	4.0	9.0
t^b	[ms]	189	308	202	221

Model	A	B	C	D
A_{20}^{E2} [cm]	$-2.0 \cdot 10^3$	$-4.1 \cdot 10^2$	$-1.2 \cdot 10^3$	$-1.5 \cdot 10^3$
A_{30}^{B2} [cm]	-7.0	-3.6	-3.5	-2.7
A_{40}^{E2} [cm]	-1.7	-0.4	-1.1	+0.4

We used the data from Muller's Model B (1991) because its initial conditions that are closest to those used in other simulations by Dimmelmeier et al. (2010).

Our aim was to produce the profile spectrum of M_{20}^{E2} for Model B in the above table. Only the leading order moment (the quadrupole moment, M_{20}^{E2}) was used. The octopole moment was not used since $M_{20}^{E2} \sim 16\sqrt{7}M_{30}^{B2}$. The data set for M_{20}^{E2} spans several milliseconds and contains a prominent bounce phase. See Fig. 3.12. This data set, produced by Muller (1991), was then used as input for our GW signal extraction model.

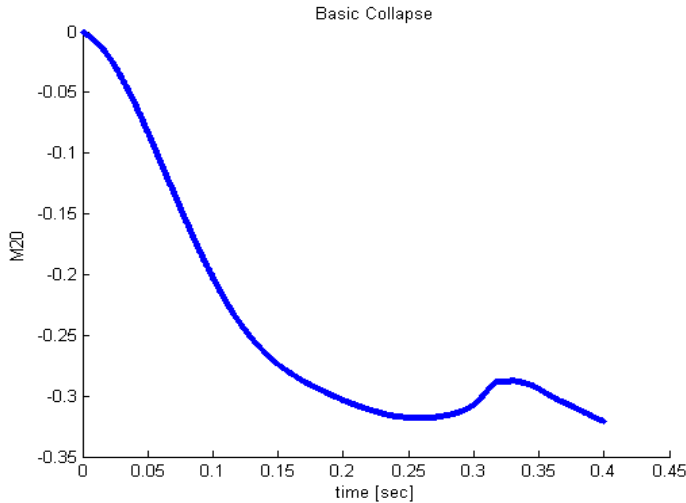


Fig. 3.12: The data set for M_{20}^{E2} of model B (from Muller, 1991).

The above figure illustrates a typical core collapse event, lasting for $t \sim 50$ ms. The core bounce interval lasts for $t \sim 10$ ms. The hydro-dynamical simulations produce globally smooth data, but locally the data set is not smooth and this generates a problem since $A_{20}^{E2} = \frac{d^2}{dt^2} M_{20}^{E2}$. Any noise present in the data will be amplified due to the second derivative operator on the data set. See Fig. 3.13 for a representation of a very noisy dataset of A_{20}^{E2}). Our algorithm was used to eliminate the simulation-induced noise and to extract the core bounce signal.

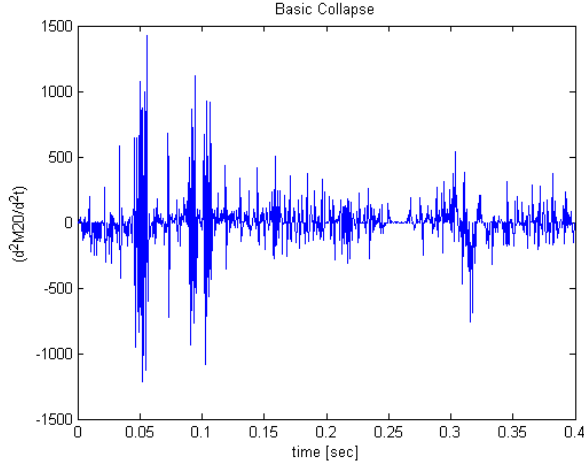


Fig. 3.13: A very noisy data set of $\frac{d^2}{dt^2} M_{20}^{E2}$. The data represented by this graph was produced by our signal extraction algorithm. The core bounce has a frequency of 10 Hertz and all high frequency noise was eliminated. An good alternative to our algorithm is that of LoWESS and LoESS. See <http://www.mathworks.com>.

To extract the core bounce signal from the noisy data $\frac{d^2}{dt^2} M_{20}^{E2}$, the signal was Fourier transformed. The unwanted frequencies were removed and the transformed signal was inverse-Fourier transformed, to obtain a clear signal which contains an evident and clear core bounce signal, see Fig. 3.14; the prominent thick line represents the extracted signal and the bounce signature located at the time of $t = 350$ ms.

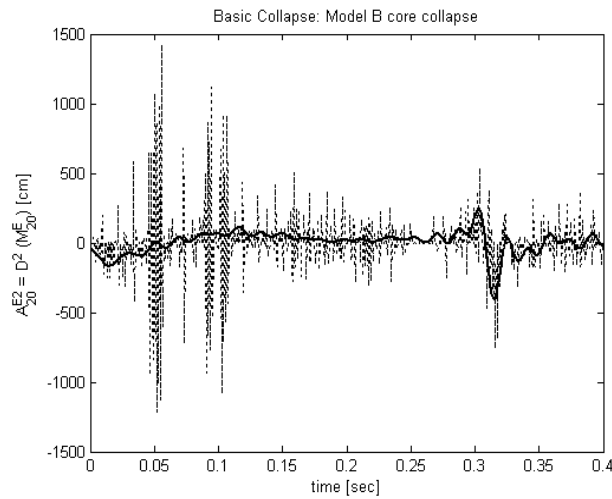


Fig. 3.14: Fourier transformed signal and the extracted core bounce signal produced by our GW signature extraction algorithm.

The extracted signal consists of the prominent core bounce and a ring-down following the bounce. Model B (with core mass $M_{core} \sim 1.12M_{\odot}$) produced a GW with amplitude of $A \sim 400$ cm and a strain of $h \sim 3.54 \times 10^{-21}$ (at a distance of 10 kPc). This is detectable with AdvLIGO for frequencies of less than 1000 Hz. This implies that SN in the galaxy anywhere between the sun and the galactic center will be detectable by AdvLIGO.

GW observations of stellar collapse probe the mechanism behind core-collapse of supernovae. GWs provide one of the more valuable windows into the heart of the core-collapse supernova mechanism. Other than GWs, neutrinos could escape the core totally unhindered (non-dispersive) during collapse, bringing with them valuable information regarding the core dynamics and structure evolution. The core bounce GW signal will also modeled numerically in Chapter 4.

3.3 Spinning objects

If a perfect sphere without any deformation spins, the reduced quadrupole moment does not change with time and no GWs are emitted. In the vast nursery of the universe, we expect non-spherical rotating objects to be born from supernovae explosions or reborn when accretion disks from the material of companions in a binary system. These rotating objects can be oblate or prolate, depending on the circumstances and properties of the objects (such as magnetic field strength and the existence of dynamical instabilities). Spinning or merging objects produce signals of longer duration that could be integrated (or observed) for longer time windows (recurring events) compared to acquisition time scales of burst events (once off event). The GW signal produced by a spinning gravitar (objects emitting GWs) is an excellent candidate for signature matching (the process of finding GWs in set of noisy LIGO data).

Neutron stars and magnetars are modeled numerically to include all the relevant macro and micro physics in order to obtain accurate GW signatures. We will investigate

analytically GWs from these exotic objects, treating them as spinning objects of ellipsoid, to produce an upper limit for the possible observed GW amplitudes. These models assume that there are no glitches in the rotational characteristics of the spinning object.

Spinning objects that radiate undergo a spin-down over long time periods. Accordingly the associated GW signatures must also change with time. The model described quantitatively in this sub-section explains the spin-down of pulsars and magnetars and the corresponding GW signatures. To solve this problem, a mathematical object (such as an ellipsoid) needs to be chosen that approximates the shape of the spinning objects, also \hat{Q}_{ij} needs to be evaluated for these objects. This formulation will approximate the energy that is radiated away by GWs. To illustrate, we chose to use an ellipsoid for this task since an ellipsoid is a slightly deformed spheroid and is mathematically well-defined. Following (Chandrasekhar, 1970a and 1970b), if an ellipsoid with semi-axis a_1, a_2 and a_3 is spinning around its principle axis, then the calculation involves the inertia tensor (I_{ij}). The inertia tensor has a well-defined form. It is symmetric with the form

$$I_{ij} = \begin{bmatrix} I_{11} & 0 & 0 \\ 0 & I_{22} & 0 \\ 0 & 0 & I_{33} \end{bmatrix}. \quad (3.11)$$

With I being the trace of I_{ij} . The components of the tensor are unique and incorporates the mass M and the semi-axis (a) of the rotating object with uniform density

$$\begin{aligned} I_{11} &= \frac{(a_2^2 + a_3^2)}{5M} \\ I_{22} &= \frac{(a_3^2 + a_1^2)}{5M} \\ I_{33} &= \frac{(a_1^2 + a_2^2)}{5M}. \end{aligned} \quad (3.12)$$

The equatorial deformation (or eccentricity) of the ellipse is $e = (I_{11} - I_{22})/I$. The magnitude of the components of the inertia tensor for a $1M_\odot$ object with average cross section $\bar{a} = 10 \text{ km}$, is $I_{11} \sim 10^{36} \text{ kg m}^2$.

If the object rotates with an angular velocity Ω , and has quadrupole tensor Q_{ij} and inertia tensor I_{ij} (see Fig. 3.15 for the basic geometrical assumptions of the rotator model), then the power radiated due to gravitational wave emission is (Bonazzola et al., 1996. See Chapter 2)

$$\langle \dot{E}_{GW} \rangle = -\frac{G}{45c^5} \langle \ddot{\hat{Q}}_{ij} \ddot{\hat{Q}}^{ij} \rangle. \quad (3.13)$$

The quantity $\ddot{\hat{Q}}_{ij}$ (the third derivative of the reduced Quadrupole moment) was calculated for a spinning rod ($\langle \ddot{Q}_{ij} \rangle \sim I\Omega^3$) and for a spinning ellipsoid ($\langle \ddot{Q}_{ij} \rangle \sim Ie\Omega^3$). The total power radiated due to GW radiation is therefore

$$-\dot{E}_{GW} = \frac{G}{45c^5} \langle \ddot{Q}_{ij} \ddot{Q}^{ij} \rangle = 10^7 \frac{32G}{5c^5} I^2 e^2 \Omega^6 \text{ erg s}^{-1}. \quad (3.14)$$

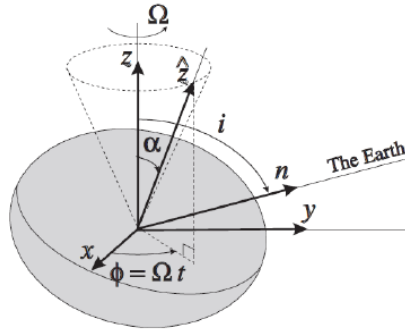


Fig. 3.15: Basic visual setup for spinning objects, the angle i is the line of sight of the observer, and α the wobble angle. This is an oblate ellipsoid (Chandrasekhar, 1970a and 1970b).

We will show that a slightly deformed rotating neutron star will emit GWs that could be detected with modern day detectors such as LIGO (see Fig.1.7 in Chapter 1 for LIGO sensitivities). Typically these spinning neutron stars have masses of $1.4M_{\odot}$ and spin-periods of the order of ms, producing GW signatures with high frequencies (more than 1 kHz) that could be detected by AdvLIGO within galactic distances. There are several properties that influence the emission of GWs. The ideal scenario is when the object rotates with a constant Ω and the shape does not change at all, but realistically this is far from the truth, since supernovae remnants contain magnetic fields and several torque mechanisms that reduce the rotational kinetic energy of the rotating object. Other effects such as dynamical instabilities also play a significant role (also known as the rotating bar-modes).

Magnetic fields, poloidal or toroidal, can deform the rotating object to an ellipsoidal star (such as magnetars that can undergo dramatic stresses and deformations). Following along the lines of Haskell (2008), if an $n=1$ polytropic equation of state object has a poloidal field, then the deformation of the object is

$$\varepsilon_p \sim 2 \times 10^{-10} \left(\frac{R}{10 \text{ km}} \right)^4 \left(\frac{M}{1.4M_{\odot}} \right)^{-2} \left(\frac{0.54B_p}{10^{12} \text{ G}} \right)^2. \quad (3.15)$$

If an $n=1$ polytrope object has a toroidal field, the deformation on the object is

$$\varepsilon_t \sim -2 \times 10^{-12} \left(\frac{R}{10 \text{ km}} \right)^4 \left(\frac{M}{1.4M_{\odot}} \right)^{-2} \left(\frac{0.17B_t}{10^{12} \text{ G}} \right)^2. \quad (3.16)$$

The sign difference is to distinguish between the oblate and prolate object. Ideally, if the deformation is large enough then the neutron star could deform or grow small irregularities on the surface (this is expressed by saying that the neutron stars are growing mountains), Fig. 3.16 for an illustrates this “deformation” process of a sphere with a size of 10 km by an internal magnetic field of 10^{15} G.

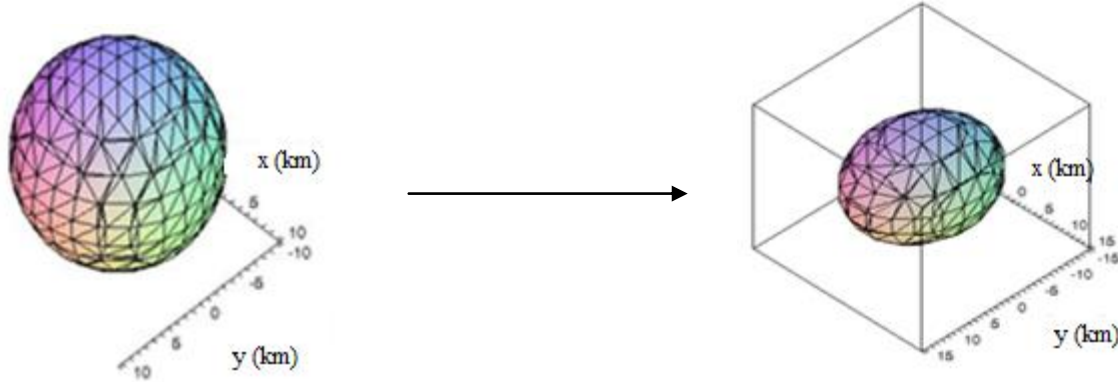


Fig. 3.16: Deforming of a spheroid into an ellipsoid due to strong internal magnetic fields.

To illustrate the size of the deformation expected, consider pulsar PSR J2124-3358 (Jones, 2002). This is a millisecond pulsar with mass $M \sim 1.4M_{\odot}$ and an equatorial radius $R \sim 7.8$ km. The upper limit for the current rotation rate of the pulsar is $f \sim 202$ Hz. Assuming that the pulsar has a purely toroidal field of $B_t \sim 8 \times 10^{14}$ G. Then the corresponding deformation is $\varepsilon_t \sim 10^{-7}$. This deformation shrinks one of the semi-axis and effectively grows a mountain (or an irregularity on the surface of the neutron star) with height of a fraction of a centimeter. Using these values, the power emitted by GWs is roughly $\dot{E}_{GW} \sim 10^{43}$ erg s⁻¹.

The initial spin period and wobble angle of the rotating object also contributes to the magnitude of \dot{E}_{GW} (see Fig. 3.17 for a representation of this relationship). The wobble angle was incorporated into \dot{E}_{GW} using the method described by Stella (2005), resulting in a total power output of

$$-\langle \dot{E}_{GW} \rangle = \frac{G}{45c^5} \langle \ddot{Q}_{ij} \ddot{Q}^{ij} \rangle = 10^7 \frac{32G}{5c^5} I^2 e^2 \Omega^6 (\sin^2 \alpha) (1 + 15 \sin^2 \alpha) \text{ erg s}^{-1}. \quad (3.17)$$

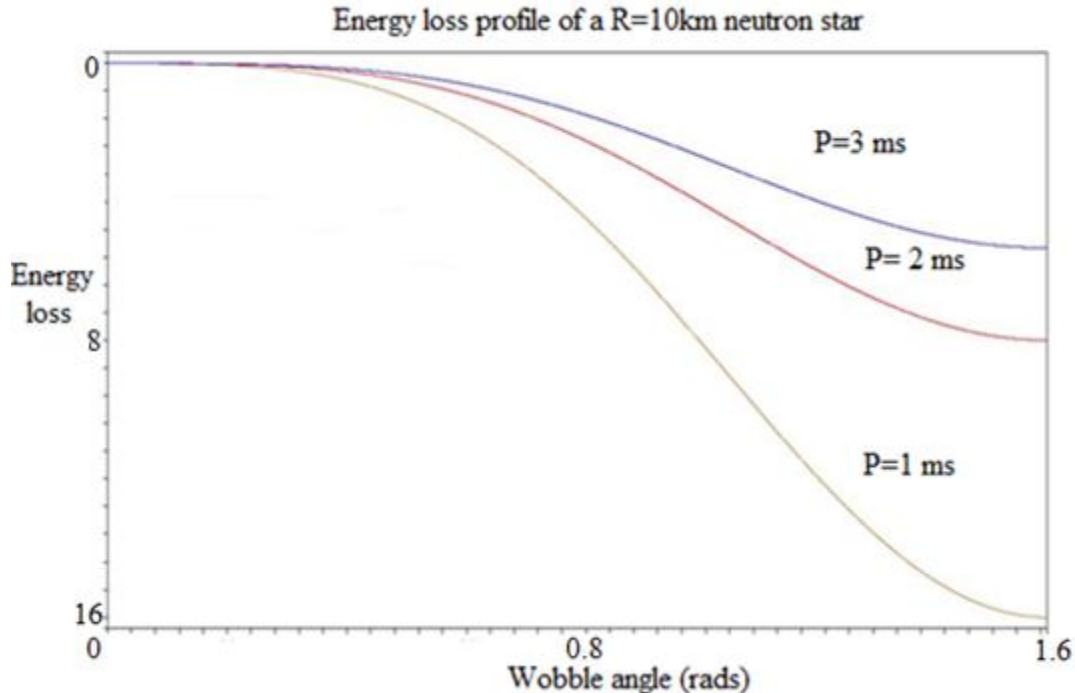


Fig. 3.17: Illustrating the influence of the wobble angle and the initial spin period of the rotating object on the magnitude of \dot{E}_{GW} (the x-axis is in normalized units).

Fig. 3.17 clearly illustrates the fact that faster spinning (more deformed) rotating objects loses energy faster due to GW radiation. If the initial spin period and wobble angle α are varied, then the main factors influencing the rotating object would also influence the ability of LIGO detectors to observe GWs (since these factors influence the spin-down and magnitude of the GWs). To investigate this influence, we use the elegant relation derived by Stella (2005) that relates the critical strain (h) to the initial spin period, the components of the magnetic field and the distance from earth to the rotating object

$$h \sim 6 \times 10^{-22} \frac{\left(\frac{B_t}{10^{16} \text{ G}}\right)^2}{\left(\frac{d}{20 \text{ kPc}}\right)\left(\frac{P_i}{2 \text{ ms}}\right)^{3/2} \left(\left(\frac{B_p}{10^{14} \text{ G}}\right)^2 + 1.15 \left(\frac{B_t}{10^{16} \text{ G}}\right)^4 \left(\frac{P_i}{2 \text{ ms}}\right)^{-2}\right)^{0.5}}. \quad (3.18)$$

This relation could be illustrated using a mesh-plot of the parameter space,

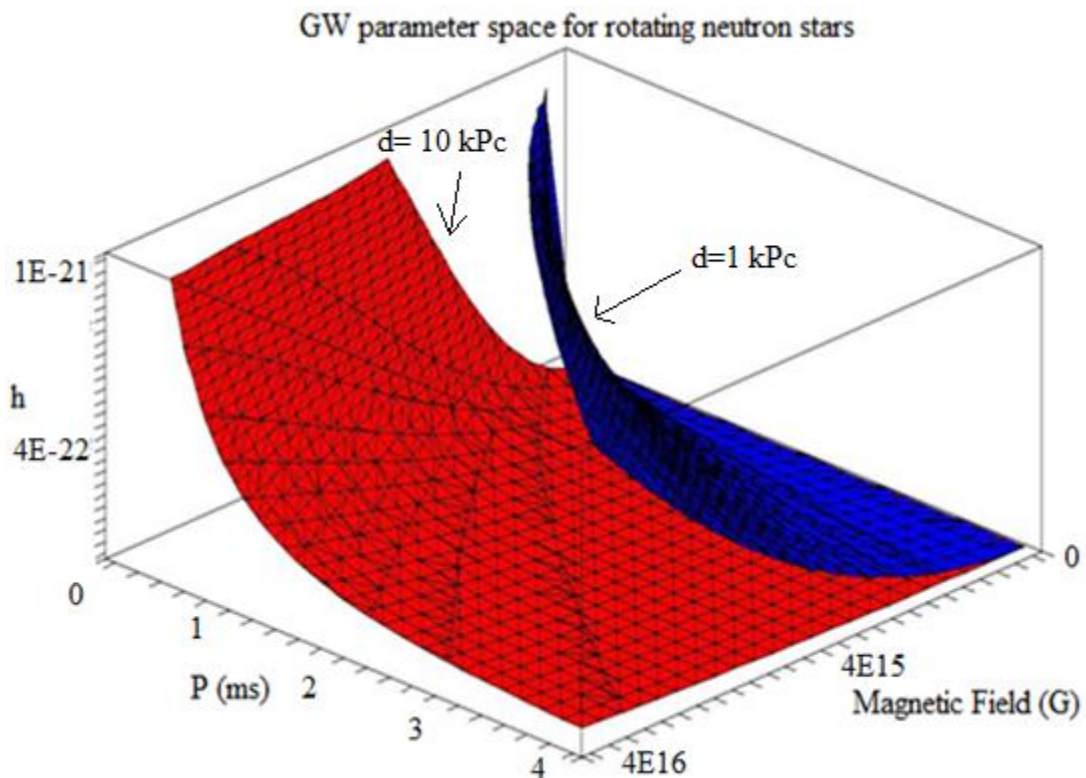


Fig. 3.18: Red surface (least steep): strains for different initial conditions, Blue surface (most steep): the distance of the object to Earth was made smaller.

Fig. 3.18 shows that the best candidates for LIGO observation are those with large magnetic fields, short spin periods, and which are closest to the detector, e.g. within the distance of 20 kPc. Candidates for observation by AvdLIGO could include pulsars,

supernovae, and magnetars up to the distance of the Hercules supercluster (see Fig. 1.8 in Chapter 1). The only part remaining is classifying the torque mechanisms that act upon the relativistically rotating object. The principle mechanisms that contribute to the spin-down include: dipole electromagnetic radiation, magnetic winds and gravitational GW reaction. We considered only the mechanisms of dipole radiation and gravitational wave emission first, two scenarios were investigated: a rotating object with and without dipole radiation, but with the GW torque mechanism present in both.

When only GW torque mechanisms are assumed, we follow along the lines of Chandrasekhar (1969). He proposed that a rotating ellipsoid that is subjected to GW radiation would tend to deform to its original state, a spheroid, and start spinning faster during the process. Chandrasekhar (1953, 1970a and 1970b) proposed that a Jacobi ellipsoid is governed by one geometrical formula and one virial equation

$$\begin{bmatrix} a_1^2 a_2^2 A_{12} = a_3^2 A_3 \\ \Omega^2 = 2B_{12}\pi G\rho \end{bmatrix}. \quad (3.19)$$

Here A_{12} , A_3 and B_{12} are Newtonian Potentials which are defined in general by

$$\begin{aligned} A_{ijk} &= a_1 a_2 a_3 \int_0^\infty \frac{du}{\Delta(a_i^2 + u)(a_j^2 + u)(a_k^2 + u)} \\ B_{ijk} &= a_1 a_2 a_3 \int_0^\infty \frac{udu}{\Delta(a_i^2 + u)(a_j^2 + u)(a_k^2 + u)}. \end{aligned} \quad (3.20)$$

Here Δ represents permutations of the terms $(a_{i,j,k}^2 + u)^{1/2}$. This formalism illustrates the phenomena that for each unique equilibrium figure there exists a unique angular velocity associated with the object. The equations of interest for this problem are:

$$\left[\begin{array}{l} a_1^2 a_2^2 A_{12} = a_3^2 A_3 \\ \Omega^2 = 2B_{12}\pi G\rho \\ \frac{d}{dt}((a_1^2 + a_2^2)\Omega) = -\frac{32}{25}\frac{GM}{c^5}(a_1^2 + a_2^2)\Omega^5 \\ e = \frac{I_{11} - I_{22}}{I} \end{array} \right]. \quad (3.21)$$

Chandrasekhar (1970a) proposed initial conditions of $(a_2)_0 = 4.3$ km, $\bar{a} = 10$ km and $\Omega_0 \sim 0.53(\pi G\rho)^{0.5}$. The effect of GW radiation can be seen in Fig. 3.19 and Fig. 3.20.

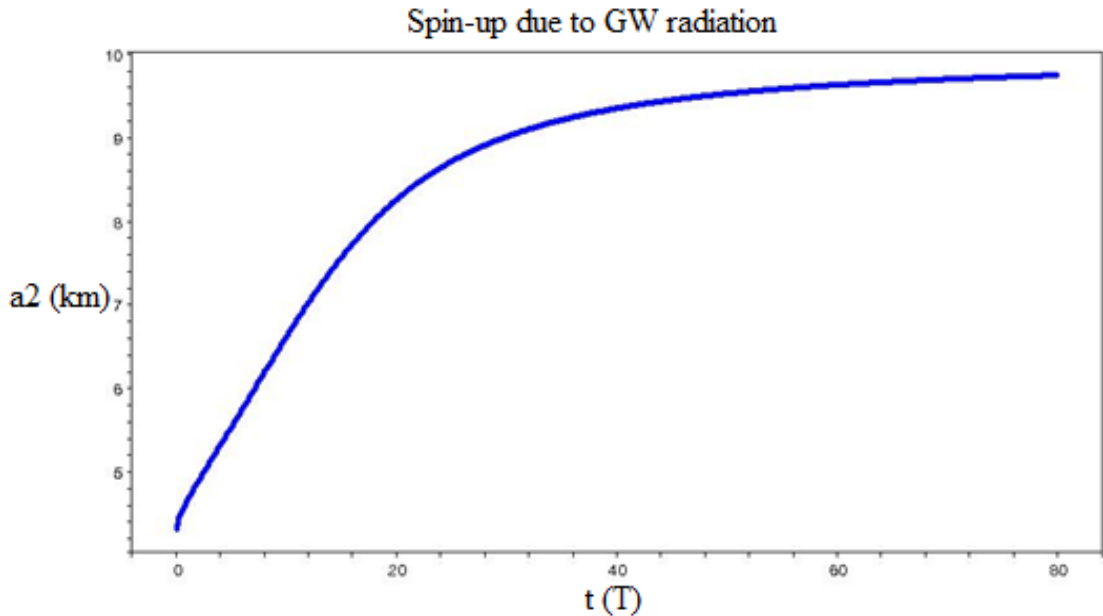


Fig. 3.19: The evolution of the semi-axis a_2 to the original state of a spheroid with a radius of 10 km. The unit of time, $T = \frac{25}{18} \left(\frac{\bar{a}}{R_s} \right)^3 \frac{\bar{a}}{c} \sim 3.23 \times 10^{-5} s$, that governs the dynamics of the spinning ellipse can be found in Chandrasekhar (1970a) Eq. (14).

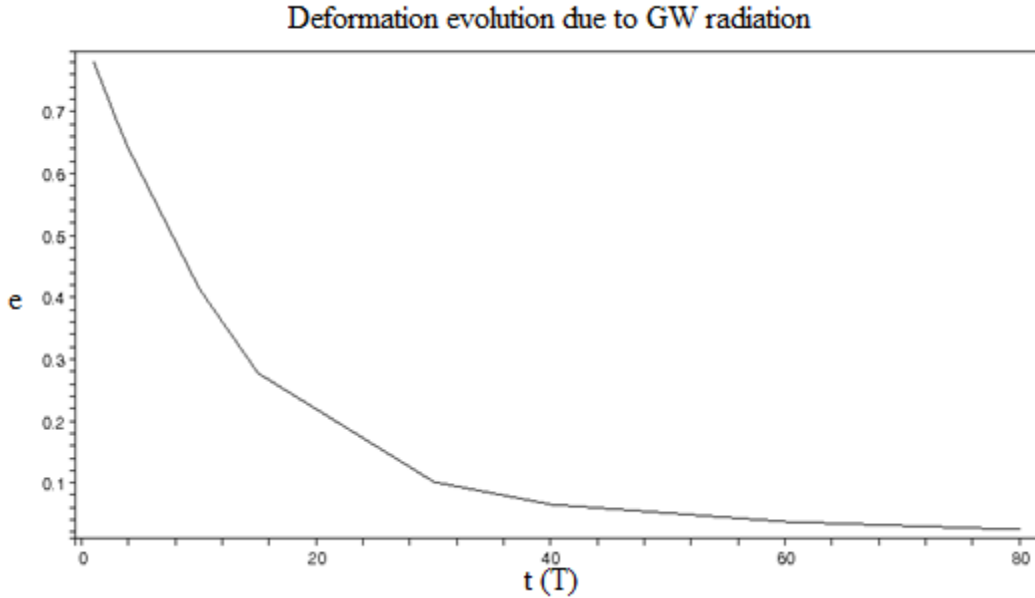


Fig. 3.20: The evolution of the deformation factor e with time.

Fig. 3.19 and 3.20 illustrate the effect of GW radiation on a rotating deformed sphere (it could be a deformed rotating neutron star); over time the deformation is radiated away and the object spins up, in an ideally sense the ellipsoid changes back to a spheroid and increases its rotational kinetic energy. The integrals of A_{ijk} and B_{ijk} are part of a special family of integrals called the Legendre elliptical integrals (Carlson, 2002)

$$Q = \int_y^x \frac{dt}{\sqrt{(a_1 + b_1 t)(a_2 + b_2 t)(a_3 + b_3 t)(a_4 + b_4 t)}}. \quad (3.22)$$

The integral is transformed into a well-known integral

$$R_F(\alpha, \beta, \gamma) = 0.5 \int_0^\infty \frac{dt}{\sqrt{(t + \alpha)(t + \beta)(t + \gamma)}}. \quad (3.23)$$

Here $R_F(\alpha, \beta, \gamma)$ is an elliptical function of the first kind and can be estimated from mathematical tables and (α, β, γ) could be any real number entry. In general any integral of the form

$$Q = \int_y^x \frac{dt}{\sqrt{\prod_{i=1}^4 (a_i + b_i t)}}, \quad (3.24)$$

has a solution of

$$Q = 2R_F(U_{12}^2, U_{13}^2, U_{14}^2). \quad (3.25)$$

Here $U_{ij} = (X_i X_j Y_k Y_m + Y_i Y_j X_k X_m) / (x - y)$, $X_i = (a_i + b_i x)^{0.5}$ and $Y_i = (a_i + b_i y)^{0.5}$, with $\{i, j, k, m\}$ representing a set of four indices, namely $\{1, 2, 3, 4\}$. These solutions have interesting symmetric characteristics

$$\begin{aligned} R_F(\alpha\lambda, \beta\lambda, \gamma\lambda) &= \lambda^{-0.5} R_F(\alpha, \beta, \gamma) \\ R_F(\alpha, \alpha, \alpha) &= \alpha^{-0.5}. \end{aligned} \quad (3.26)$$

Here $(\alpha, \beta, \gamma, \lambda)$ are any real number values. Considering the relation $\Omega^2 = 2B_{12}\pi G\rho$, we developed a relationship (see Fig. 3.21 for a representation of this relation between the spin period and the semi-axis) between Ω and the ratios of the axis, $k = \frac{a_3}{a_1}$ and

$$l = \frac{a_2}{a_1}, \text{ i.e.}$$

$$\Omega^2 = (2\pi G\rho)a_1 a_2 a_3 \int_0^\infty \frac{udu}{\Delta(a_1^2 + u)(a_2^2 + u)(a_3^2 + u)}. \quad (3.27)$$

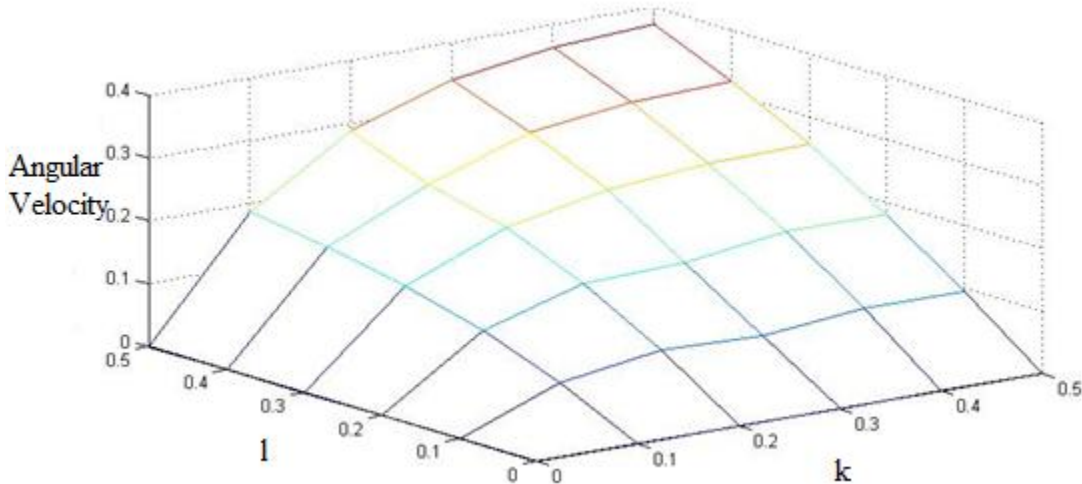


Fig. 3.21: Angular velocity as a function of distortion. The emission of GWs slowly changes the ellipsoid to a spheroid. The angular velocity is presented in normalized units with initial values that were proposed by Chandrasekhar (1970a).

Fig. 3.21 illustrates the phenomena of the effect of GW radiation on a rotating ellipsoid; the end-result is a faster rotating spheroid (Eq. (2.27) was solved in MATLAB). GW emission radiates away any deformation of the object over long enough time periods.

The torque mechanism for EM dipole radiation is similar to that of GW spin-down mechanisms (Stella, 2008)

$$\dot{\Omega}_{dipole} = -\frac{2Gle^2\Omega^5}{5c^5} \sin^2(\alpha)(1+15\sin^2(\alpha)). \quad (3.28)$$

Where e represents the deformation of the star. If one considers the case of maximal GW emission (where α is a maximum), then it follows by inspection that $\dot{\Omega}_{dipole} \gg \dot{\Omega}_{GWs}$.

Returning to the main relation of this sub-section $\left(\dot{E}_{GW} = -10^7 \frac{32G}{5c^5} I^2 e^2 \Omega^6 \text{ erg s}^{-1} \right)$ it

directly follows that $\dot{E}_{GW} \sim I^2 e^2 \Omega^6$. A realistic model for the GW signature from these spinning objects needs to be developed (including all the leading order spin-down

effects), to develop accurate templates for LIGO for use in searches for GWs from these objects. This will be the task of the next section, to investigate a primitive magnetar spin-down model.

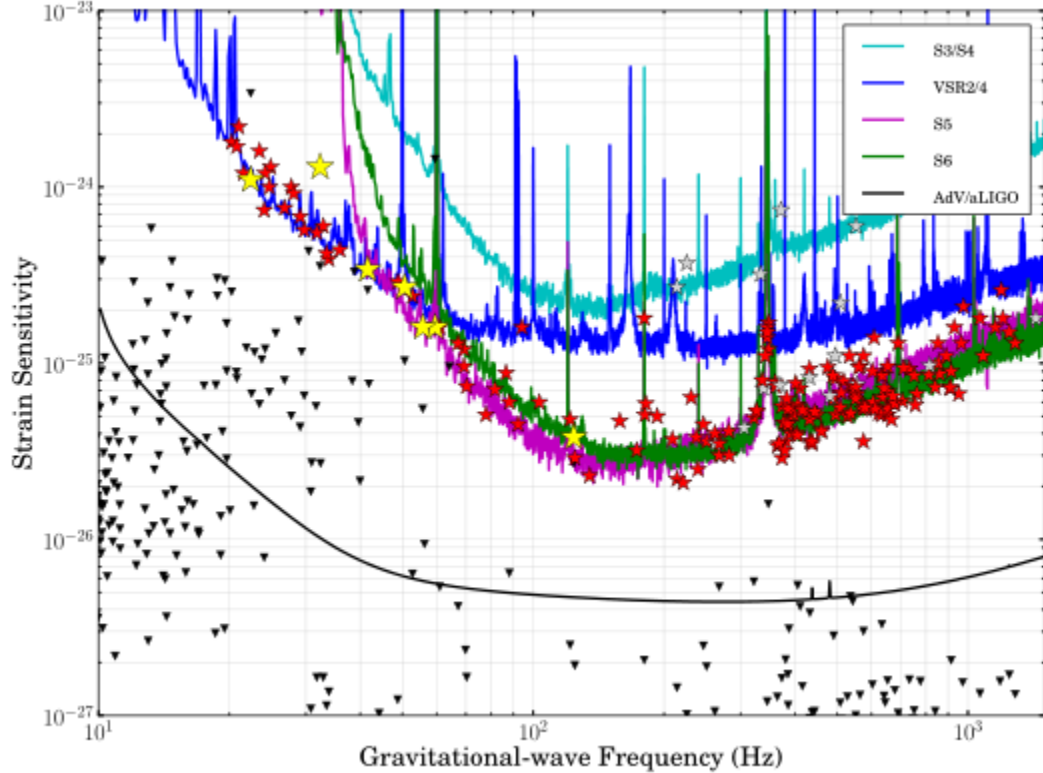


Fig. 3.22: GW strain upper limits for several pulsars with respect to the sensitivity (black solid line) aimed at AdvLIGO (from Aasi et al., 2013). The reader can refer to the paper of Aasi et al. (2013) for another overview on GWs from spinning objects. The “stars” are the strain upper limits of the pulsars and the “triangles” are spin-down upper limits for various pulsars from the catalogue. For background on this figure see Table 8 and Fig. 1 in the paper of Aasi et al. (2013). Readers who wish to calculate the GW upper limits for various known pulsars can use the ATNF pulsar catalog (<http://www.atnf.csiro.au/people/pulsar/psrcat/>).

Why is it so important to have these astrophysical objects in the GW template banks of LIGO and other ground based interferometers? The answer to this question was presented in a recent paper by Aasi et al. (2013) where the authors calculated the GW upper limits for a large number of pulsars. They also plot the GW contributions of these pulsars and the sensitivity lines of LIGO including AdvLIGO). See Fig. 3.22.

3.4 A primitive magnetar model and an application

To introduce this sub-section on GWs from magnetars, we refer the reader to a recent paper that contains radio pulse broadening measurements for the recently discovered galactic center pulsar J1745-2900 (Spitler et al., 2013). This pulsar is a magnetar that was discovered 3 arcseconds away from Sgr A* by using the Effelsberg 100-m Radio Telescope (together with independent detections by other radio telescopes). This magnetar has a magnetic field of $B \sim 10^{14}$ G and could be used measure the effect of the galactic interstellar plasma screen on emitted pulses or flares (the pulse smearing effect).

Magnetars are neutron stars that acquire really large magnetic field strengths through a process of differential rotation and amplification of the initial magnetic field of the spinning object. It is evident from the previous sections that these objects must have fast initial rotational spin periods or large magnetic fields to justify the observed spin-down rate. The magnetic fields range between 10^{14} G – 10^{17} G (Stella, 2005). The massive magnetic field produces a slight deformation of the object, which makes it unstable and oblate (Chandrasekhar, 1970a).

Due to the enormous initial spin rates and magnetic fields, the object loses rotational energy very rapidly and the spin-down rate is unusually large. There are several prominent mechanisms that torque the spin-down of the infant magnetar. These include:

dipole radiation due to the pole magnetic fields (see Fig. 3.23), magnetic winds and, less prominent, gravitational wave emission. Gravitational Waves contribute least to the total radiated energy from the spinning object, but Gravitational Wave (GW) signatures accompany every small kink, core collapse, gamma ray burst, transition to other classes of compact objects and final stellar end-points such as black hole formation. GW signatures can provide useful information about the object.

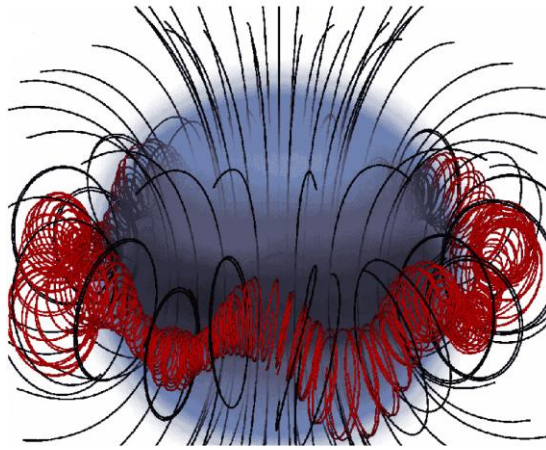


Fig. 3.23: Growing MHD (Magneto Hydro Dynamical) instability in magnetars that might cause the exotic magnetic field arrangements in the rapidly spinning magnetars (from Aharonian et al., 2013).

To produce a primitive magnetar model, it is necessary to investigate all the mechanisms that act on the spinning object. This was done in the previous section for the GW radiation and the dipole radiation, both being very distinct, but dipole radiation dominates as the leading torque mechanism. The model is based on a few assumptions (see Fig. 3.24 for the geometrical assumptions of the magnetar model): the spinning magnetar is an orthogonal rotator, the main torque mechanism is dipole electromagnetic radiation, any deformation in the object is due to the internal magnetic field configuration, any kinks (like star quakes or glitches) are ignored, and finally, the line of sight and the wobble angle are optimal (that is $\alpha = \pi/2$ and $i = 0$).

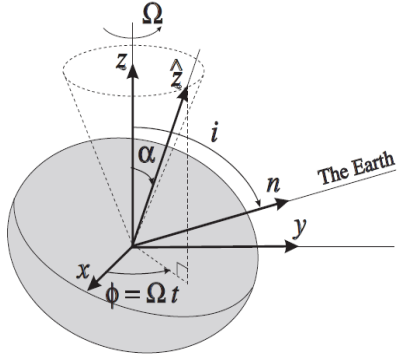


Fig. 3.24: Geometrical assumptions for the spinning magnetar, deformed by a magnetic field (from Bonnazzola, 1996).

We applied this model to three different magnetars with identical spin periods, masses, and distances from the Earth, but different magnetic field configurations. The parameters for these three cases were:

$$\begin{cases} a = (B_t \sim 10^{15} \text{ G}, B_p \sim 10^{14} \text{ G}, e \sim 10^{-6}) \\ b = (B_t \sim 10^{16} \text{ G}, B_p \sim 10^{15} \text{ G}, e \sim 10^{-4}) \\ c = (B_t \sim 10^{17} \text{ G}, B_p \sim 10^{16} \text{ G}, e \sim 0.01) \end{cases}. \quad (3.29)$$

Assuming that the three magnetars all have spin periods of $P_i = 2$ ms, neutron star sizes of $\bar{a} = 10$ km, masses of $1M_\odot$ and are at a distance of 10 kPc (Galactic distance) from Earth, then the GW signature, derived from the quadrupole formalism (Haskell, 2008), is given by

$$h_x = 2h_0 \sin(2\Omega t)$$

$$h_0 = 10^{-27} \left(\frac{I}{10^{38} \text{ kg m}^2} \right) \left(\frac{10 \text{ kPc}}{\text{d}} \right) \left(\frac{\Omega}{100 \text{ Hz}} \right) \left(\frac{e}{10^{-6}} \right), \quad (3.30)$$

with I , d , Ω and e representing the moment of inertia of the neutron star, the distance to the source, the angular velocity and the eccentricity respectively.

Ideally the object would spin without losing any energy and the spin rate would remain constant, but realistically seconds after birth some magnetars loses a large part of its energy reservoir (see Fig. 3.25). To construct the model, all torque mechanisms need to be included

$$\begin{aligned}\dot{\Omega}_{total} &= \dot{\Omega}_{GW} + \dot{\Omega}_{dipole} + \dot{\Omega}_{MW} \text{ (sec}^{-2}\text{)} \\ &= -\frac{2GIe^2\Omega^5}{5c^5} \sin^2(\alpha)(1+15\sin^2(\alpha)) - \frac{1}{6} \frac{B_d^2 R^6}{I c^3} \Omega^3 \sin^2(\alpha) - \frac{B_{pole}^2 R^6 \Omega^3}{3c^3 I} \left(\frac{R_{LC}}{r_{open}} \right)^2.\end{aligned}\quad (3.31)$$

This total spin-down formula includes dipole radiation ($\dot{\Omega}_{dipole}$), magnetic winds ($\dot{\Omega}_{MW}$) and GW radiation ($\dot{\Omega}_{GW}$) spin-down rates (MTW, 1970). We derived the equations for the power emitted, incorporating losses through GWs, magnetic dipole radiation and magnetic winds

$$\begin{aligned}\dot{E}_{tot} &= \dot{E}_{GW} + \dot{E}_{dipole} + \dot{E}_{MW} = I\Omega \dot{\Omega}_{GW} + I\Omega \dot{\Omega}_{dipole} + I\Omega \dot{\Omega}_{MW} \\ &= -\frac{2GI^2 e^2 \Omega^6}{5c^5} \sin^2(\alpha)(1+15\sin^2(\alpha)) - \frac{1}{6} \frac{B_d^2 R^6}{c^3} \Omega^4 \sin^2(\alpha) - \frac{B_{pole}^2 R^6 \Omega^4}{3c^3} \left(\frac{R_{LC}}{r_{open}} \right)^2,\end{aligned}\quad (3.32)$$

where $B_{pole} = B_d$, R , R_{LC} and r_{open} represents the neutron star magnetic field at the polar cap, radius of the neutron star, radius of the light cylinder and the radius of the polar cap of the neutron star respectively. The light cylinder radius (R_{LC}) is the distance from the neutron star to where magnetic fields sweep around at the speed of light.

Fig. 3.25 illustrates the fact that EM dipole radiation dominates the spin-down in the early life of the Magnetar. This effect will influence the spin-down profile of the Magnetar and the associated GW signature profile.

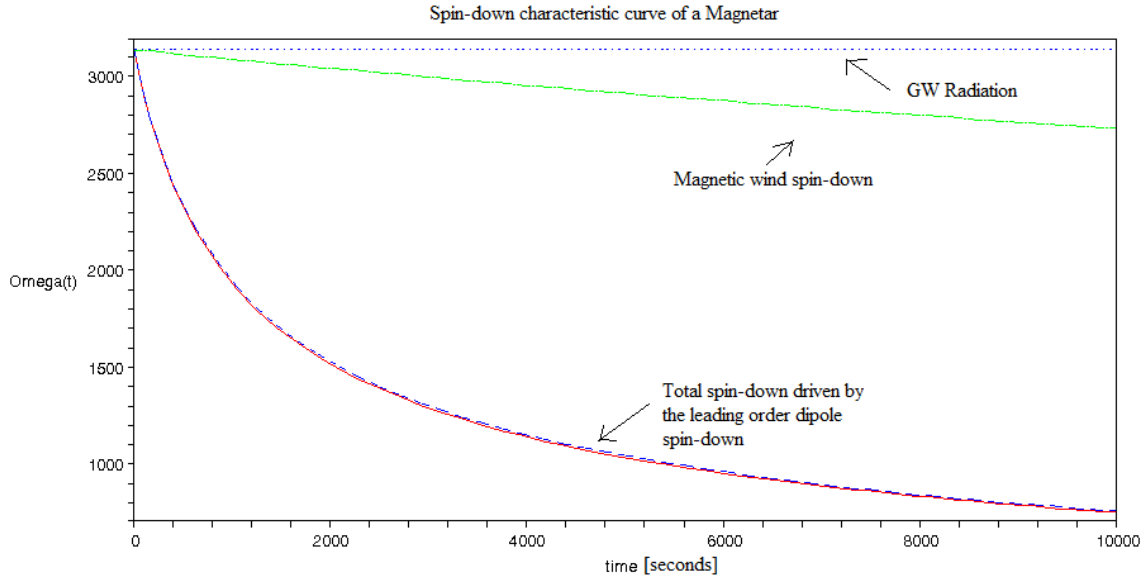
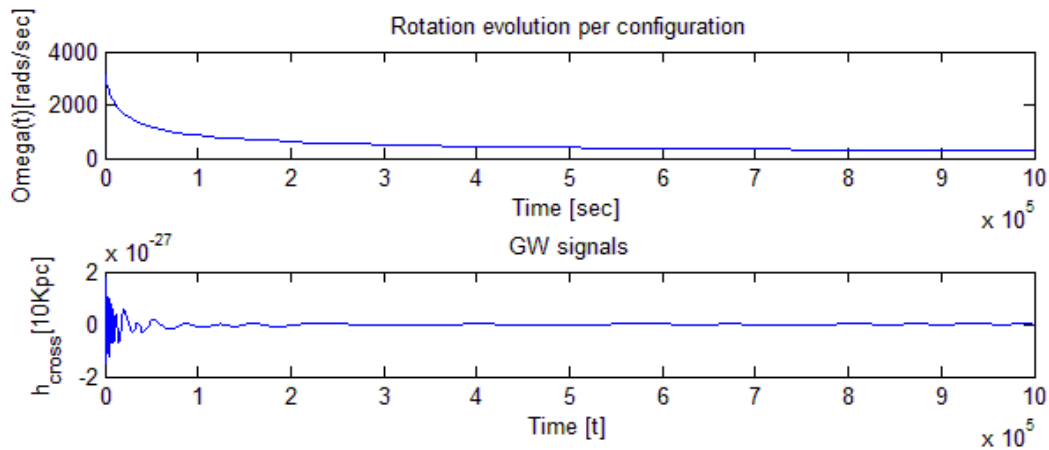


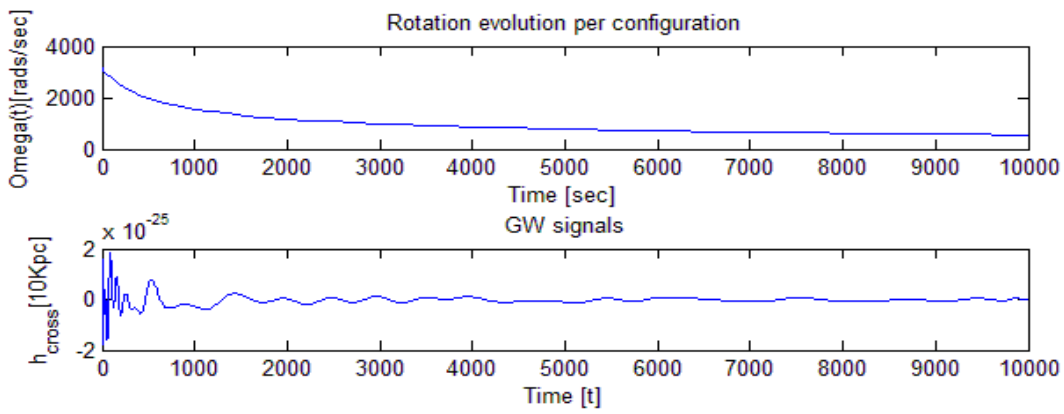
Fig. 3.25: Evolution of Ω , due to each spin-down mechanism for initial conditions of $B_t \sim 10^{16}$ G, $B_{pole} \sim 10^{15}$ G, $R \sim 10$ km, $e \sim 10^{-4}$, $I \sim 10^{36}$ kg m² and $P_i \sim 2$ ms. The time (t) is in seconds. GWs contribute least to the spin-down over this time interval and become increasingly less dominant for spun-down pulsars.

I used MATLAB to evolve the dynamical system consisting of h_x , $\dot{\Omega}_{total}$ and t . This algorithm enabled us to calculate the individual signature formations of the produced GWs from such spinning objects. The model was applied to magnetars of different magnetic configurations. Fig. 3.26 shows the signatures produced by the algorithm for different magnetars. GW signatures displayed in Fig. 3.26 and Fig. 3.27 were produced by modeling rapidly spinning magnetars (Stella, 2005) with initial periods of $P_i = 2$ ms (this is the period associated with young magnetars shortly after birth), but with different magnetic fields and eccentricities.

(a)



(b)



(c)

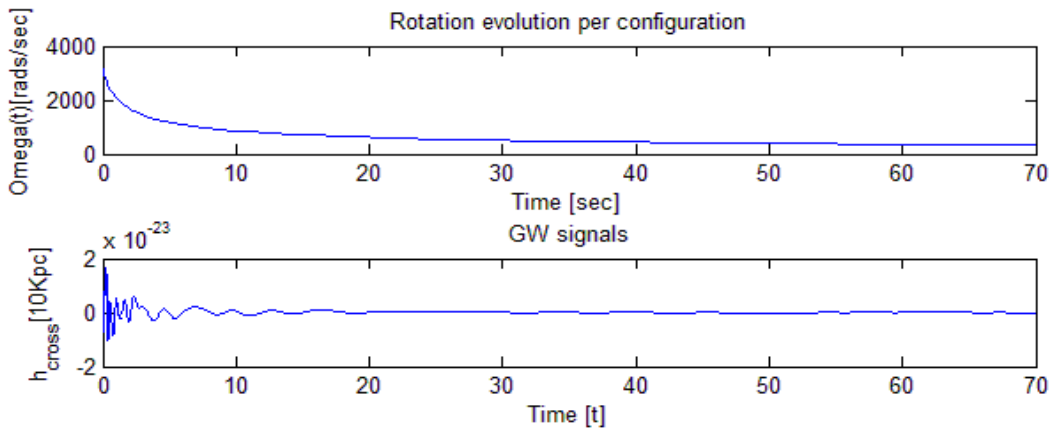


Fig. 3.26: Evolution of the GW waveform for $a = (B_t \sim 10^{15} G, B_p \sim 10^{14} G, e \sim 10^{-6})$,
 $b = (B_t \sim 10^{16} G, B_p \sim 10^{15} G, e \sim 10^{-4})$ and $c = (B_t \sim 10^{17} G, B_p \sim 10^{16} G, e \sim 0.01)$.

Fig. 3.26 illustrates the spin-down evolution of magnetars with time; these figures show that the magnetars are most active (from the view point of their GW signature evolution) for a short time after birth. AdvLIGO could detect the GWs produced by these magnetars within galactic distances, since just after birth they produce GWs with frequencies of several kHz and strains of $h \sim 10^{-23}$ (see Fig. 1.7 in Chapter 1).

We also applied this model to a known magnetar, SGR 1806-20 (see Fig. 3.27). It was discovered in 1979 and has been identified as a soft gamma repeater. SGR 1806-20 is located about 14.5 kPc (50,000 light-years) from Earth on the far side of our Milky Way galaxy in the constellation of Sagittarius. It has a diameter of no more than 20 kilometers and rotates about its axis every 7.5 seconds (Aharonian et al., 2013). This specific magnetar application is different from those in Fig. 3.26, in that the magnetar (SGR 1806-20) possesses more realistic parameters that could set upper limits for LIGO magnetar GW detections.

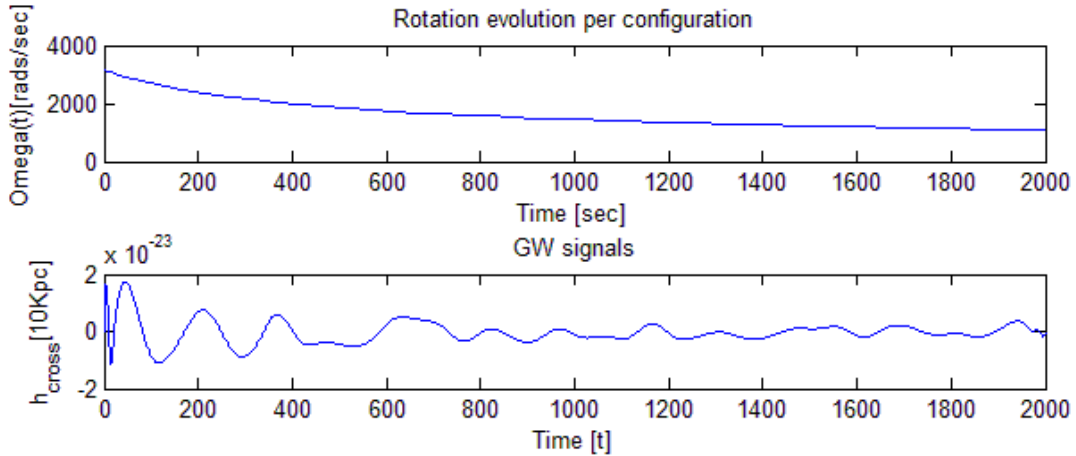


Fig. 3.27: The evolution of the GW waveform of SGR 1806-20 with parameters of $P_i = 2$ ms, $\bar{a} = 12$ km, $M = 1.4M_{\odot}$ and $d = 14.5$ kPc.

Fig. 3.27 illustrates typical GW signatures for realistic magnetars at a distance of a few kPc (galactic magnetars). Typical spin-down time scales for a, b, and c (see Fig. 3.26) spinning down to a frequency of 10 Hz are: 0.85 years, 3 days and 0.77 hours. The model represents realistic spin-down time scales (Stella, 2005). The initial frequency,

size, and deformation influence the evolution of the dynamic system and the spin-down rates. AdvLIGO could readily detect these GWs with frequencies of several kHz and strains of $h \sim 10^{-23}$ (see Fig. 1.7 in Chapter 1).

3.5 Binary neutron star mergers

This upper limit model was modified for a further application to binary neutron star mergers. Hotokezaka (2011) showed using relativistic simulations of the merging objects, how the merger occurs and investigated its evolution after, either collapsing into a black hole or the formation of Hyper Massive Neutron Stars (HMNS). These merging events are the most important sources of GWs and hold secrets to unlocking the questions of how the equation of state (EoS) of exotic objects influences the evolution of the star. See Table 3.4 and Fig. 3.28 for simulations by Hotokezaka (2011) of several different mergers. We used data presented in Hotokezaka (2011) to decide what initial conditions needed in our modified model for mergers.

Table 3.4: Different EoSs producing mergers with different masses and sizes (Adapted from Hotokezaka, 2011).

EOS	Mass (M_{\odot})	R (km)
APR4	2.213	11.428
Sly	2.047	11.736
H3	1.788	13.840
H4	2.032	13.759

Here APR4, Sly and H3 are EoSs derived by a variational method applied to a core consisting of neutrons and protons, an effective potential applied to the same type of core as APR4, and a relativistic mean-field method applied to a core consisting of neutrons,

protons and hyperons. The EoS H4 is identical to that of H3, but with a different nucleon-meson coupling coefficient (Hotokezaka, 2011). These different EOSs produce HMNS with different sizes.

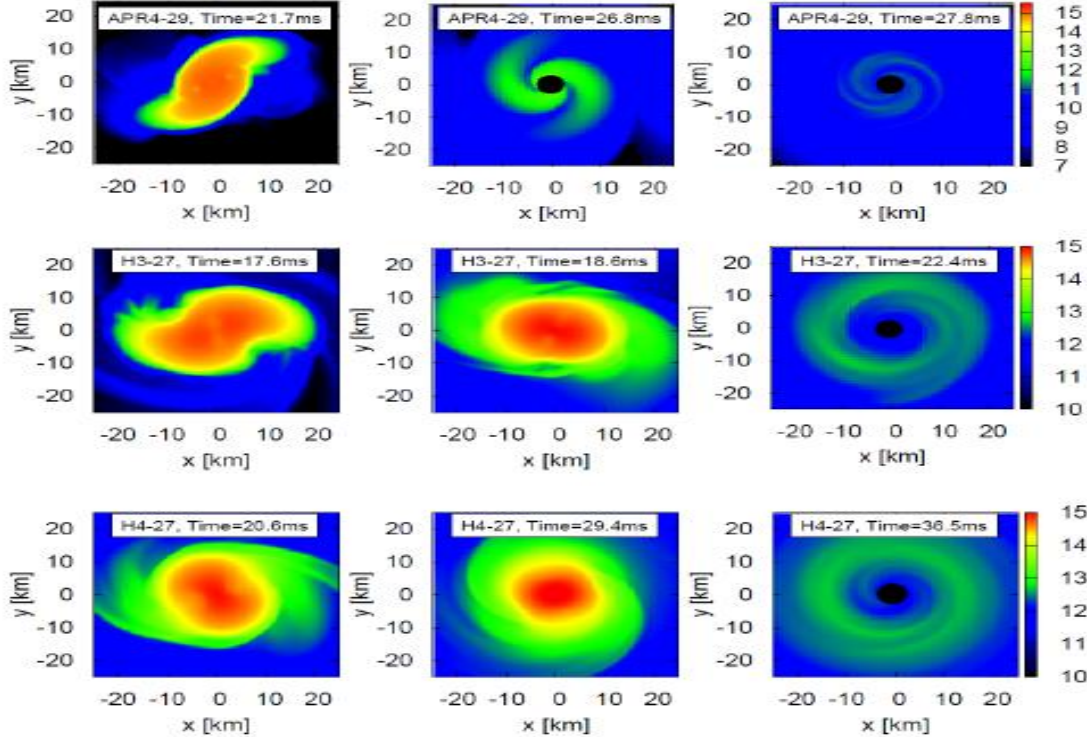


Fig. 3.28: The evolution of several mergers with different EOSs resulting in different scenarios (HMNS or BH formation) (from Hotokezaka, 2011)

The final cataclysmic moments of binary neutron star mergers last for about $t \sim 100$ ms. Hyper massive neutron star (HMNS) formation last only several miliseconds. In these events the merging soup of particles is subjected to a plethora of forces and rotation. Energy is emitted away quickly, making these objects prime candidates for Gamma Ray Bursts (GRB) and Short Gamma Ray Bursts (SGRB). Important to this thesis are the accompanying GWs.

To modify our algorithm for this application, the torque mechanisms must be included that deals with the changing structure of the rotating object resulting from mass shedding, GW energy radiation and EM dipole radiation. The point of departure is the spin-down $\dot{\Omega}_{total}$ (Shibata, 2002)

$$\begin{aligned} \dot{\Omega}_{total} &= \dot{\Omega}_{GW} + \dot{\Omega}_{shedding} + \dot{\Omega}_{dipole} \\ &= -\frac{2Gle^2\Omega^5}{5c^5} \sin^2(\alpha)(1+15\sin^2(\alpha)) - I^{-1} \left(10^{41} \left(\frac{B_{pole}}{10^{13}} \right)^2 \left(\frac{R}{10 \text{ km}} \right)^3 + 10^{40} \left(\frac{B_{pole}}{10^{13}} \right)^2 \left(\frac{R}{10 \text{ km}} \right)^3 \right). \end{aligned} \quad (3.33)$$

For this scenario, deformation plays a significant role. The model was constructed together with the Maclaurin Spheroid sequence ($-2A_1I_{11} + \Omega^2I_{11} = -2A_3I_{33}; \Omega^2 = 2e^2B_{13}$) which states that for every object with unique rotation (Ω) there exists a corresponding deformation factor e (with A_1, A_3 and B_{13} being the Newtonian ellipsoidal potentials). As in the previous sub-section of spinning objects, this application produces a new modified dynamical system that needs to be solved

$$\begin{aligned} -2A_1I_{11} + \Omega^2I_{11} &= -2A_3I_{33} \\ \Omega^2 &= 2e^2B_{13} \\ \dot{\Omega}_{total} &= \dot{\Omega}_{GW} + \dot{\Omega}_{matter} + \dot{\Omega}_{dipole} \\ e &= \frac{a_2 - a_1}{\sqrt{a_1a_2}} \\ I &= \frac{1}{5}M(a_1^2 + a_2^2 + a_3^2). \end{aligned} \quad (3.34)$$

We have used several EOSs (APR4, Sly, H3 and H4 in Hotokezaka, 2011) to investigate their influence on the GW signature of merger. These objects were assigned an initial deformation of $e \sim 0.8$ and placed a distance of 100 Mpc from Earth. The new model was solved, using a modified algorithm, to predict the first 10 ms of such an event. See Fig.

3.29 and Fig. 3.30 for a representation of the GW signature produced by these different mergers.

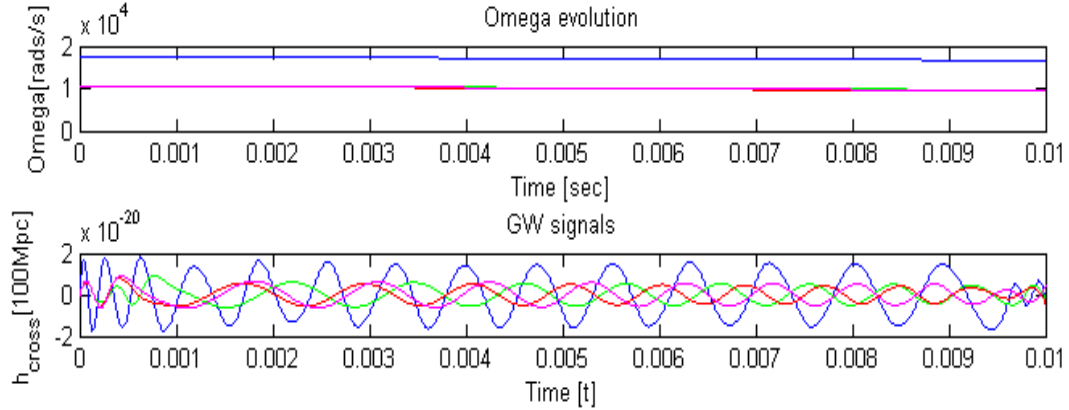


Fig. 3.29: GW signature of HMNS during binary neutron star merging. The EOS APR4, which is a variational method with neutron-proton composition, emits the maximum GW signal. The colour legends can be found in Fig. 3.30.

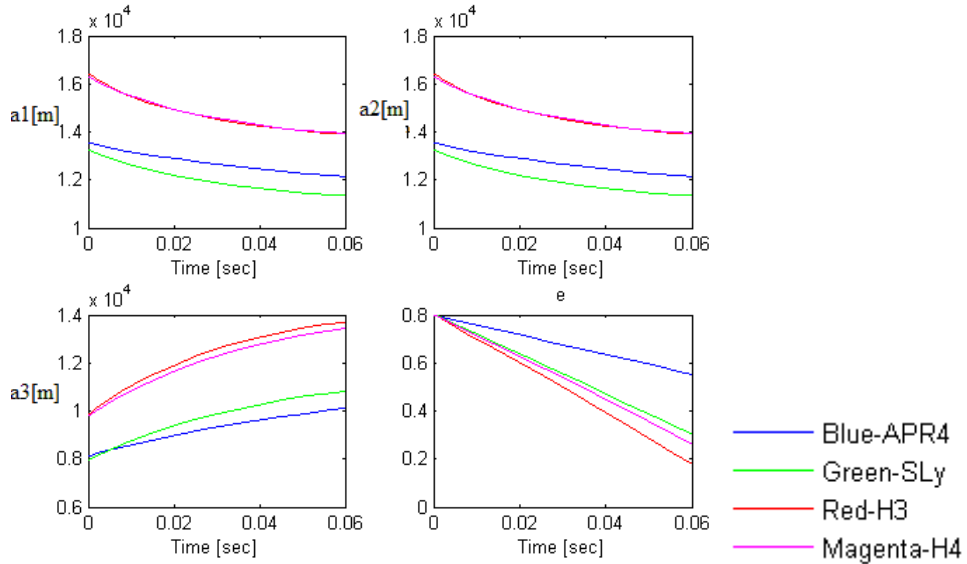


Fig. 3.30: The time evolution of the semi-axis and the deformation factor for the first 10 ms for several HMNS evolutions, the Maclaurin sequence tends to a spheroid ($e \rightarrow 0$) over time.

The EoS plays a major role in the maximum strain produced by such an event, it allows the existence of unique objects (HMNS) and objects with unique size, rotation and life cycles, also showed in Hotokezaka (2011). There exist distinct GW signatures for each EOS, and the evolution of the instability evolve uniquely. For this event the EOS APR4 produced the most prominent strain which can be observed by the LIGO or AdvLIGO detectors (in the upper limit case). Our algorithm dynamically evolves the geometrical form of the merging objects, through the process of calculating the Maclaurin sequence associated with these objects (see Eq. 3.34).

Fig. 3.29 and Fig. 3.30 show the upper limits for the GW signatures produced by our algorithm, for several mergers that evolve in the first few milliseconds after the merging event. Different EoSs were used to simulate merger objects of different sizes (see Table 3.4). Read et al., (2013) studied the influence of the EOS on the tidal fields produced by each merging companion in the last few orbits before merging. The tidal field warps the spacetime and produces GWs. Supernovae core bounce events, magnetars and binary neutron star mergers are all possible sources of GWs, depending on their initial spin periods, EOS, magnetic fields, mass and structural deformations. Due to the torque mechanisms that are present, the maximum GW activity windows of these objects occur only in the earliest stages of the evolution. Due to the fast energy deposition rates of the above investigated remnants, GRB events are associated with merging neutron stars and other remnants, and these events could be observed by modern large array radio-telescopes such as the SKA, in an attempt to unify GW detectors with radio and optical telescopes.

3.6 Binary neutron stars (NSNS)

Another application of the GW quadrupole formalism is to GWs produced by compact binary systems (see Chapter 1 and Chapter 2). These objects could be young or old binaries, located in the galaxy with elliptical or circular orbits. It is possible to formulate the change in the parameters of such systems due to GW radiation (Peters et al., 1963).

The change in the semi-axis (a) of a binary system (with total mass $M = M_1 + M_2$ and eccentricity e) is

$$-\frac{da}{dt} = \frac{64G^3\mu M^2}{5c^5 a^3 (1-e^2)^{-\frac{7}{2}}} \left(1 + \frac{73}{24}e^2 + \frac{37}{96}e^4 \right). \quad (3.35)$$

Using Kepler's Law (with chirp mass denoted by $\Upsilon = \mu^{3/5}M^{2/5}$ and $\mu = \frac{M_1 M_2}{M}$). Then, applying Kepler's law, the rate of frequency is given by

$$\frac{df}{dt} = \frac{96G^{5/3}\pi^{8/3}}{5c^5} \Upsilon^{5/3} f^{11/3}. \quad (3.36)$$

Here f represents the frequency of the GW, which is $f_{GW} = 2f_{orbital}$. If the binary consists of two equal mass companions; the chirp mass reduces to $\Upsilon \sim M_{NS}$ for binary neutron stars, and $\Upsilon \sim M_{BH}$ for binary black holes. The typical GW strains for these binary systems were calculated using the quadrupole formalism and Kepler's law by Peters et al., (1963) and were found to be

$$h_x = \frac{4\mu G^2 M}{c^4 ad} \cos 2\omega t. \quad (3.37)$$

Here d , a and ω correspond respectively to the distance to the GW source, the separation distance and the Keplerian frequency, given by $\omega = \sqrt{\frac{GM}{a^3}}$.

Using a Taylor (Taylor-T1) expansion for the GW reaction ($\dot{E}_{GW} = -F(\nu) \propto \Omega^6$) (see for example Landau and Lifschitz., 1975), and performing orbital speed (ν) and phase (φ) modulation for a binary system with two equal neutron star like objects, a chirp GW

signal was investigated to illustrate the effectiveness of the Taylor approximations (Konstantin et al., 2006). The Taylor T1 method is based on an adiabatic circular approximation of the orbit (assuming that the orbit shrinks only because of GW energy loss).

The phase modulation is $\dot{\phi}(t) = \frac{v^3}{GM}$, the orbital velocity modulation is

$$\dot{v}(t) = -F(v) \left(\frac{dE}{dv} \right)^{-1} \quad (\text{the function } F(v) = \frac{32}{5} \frac{G^{7/3}}{c^5} (M\pi f_{GW})^{10/3} \text{ is the GW flux}).$$

These results reduce the problem to the solution of two differential equations for the functions of $v(t)$ and $\phi(t)$. We now have all the necessary elements to determine the GW signature h_x (defined in Eq. 3.37) of a typical binary neutron star system. See Fig. 3.31 for an illustration of the merging process of two neutron stars. The GW signal represents a chirp signal that could be detected by AdvLIGO several days before the merging process occurs. See the high frequency domain of Fig. 1.9(a,b).

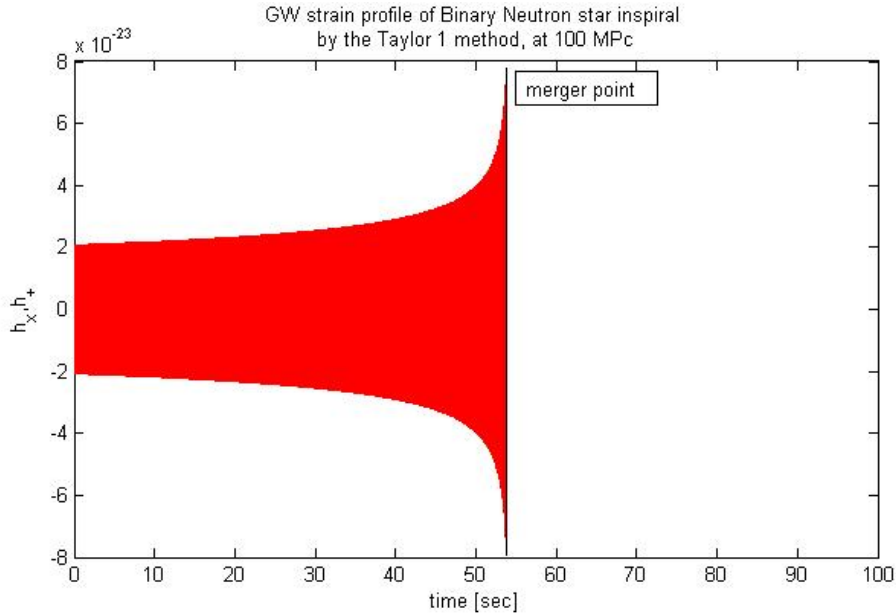


Fig. 3.31: This graph represents the strain evolution of a merger of two equal mass neutron star moments before the actual merger.

Compact binary coalescence also enters the LIGO band ($f \sim \text{kHz}$) when the two companions get relatively close to one another. Binary neutron star mergers produce a unique GW spectrum that consists of burst and ring-down large amplitude GW signals (see Chapter 1). It is for this reason that NSNSs are the most likely to be observed with LIGO. These sources govern most of the templates of GW signatures produced by simulations in the field of Numerical relativity. The usefulness of these sources goes beyond the limit of ground based interferometers. The SKA will be able to observe the pulsars in these binary systems and also the indirect effect of GWs (such as the Hulse-Taylor binary pulsar (Landau and Lifschitz., 1975)). The chirp mass $(\gamma = \mu^{3/5} M^{2/5})$ strictly determines the merger time and the GW chirp waveform moments before merging. Approximation techniques could be used to determine the waveform for the regime where $\frac{\nu}{c} \ll 1$. Otherwise numerical recipes can be used to approximate the merger GW waveform (Landau and Lifschitz, 1975).

In this Chapter we used analytical methods to construct upper limit models for the GW signatures emitted by several galactic sources that might be detected by AdvLIGO. In Chapter 4, we will use numerical methods to predict approximate GW signatures for SN core bounce. We will compare the results to that what we found analytically in Chapter 3. In the next Chapter we will formulate the quadrupole tensor (see Chapter 2) in a numerical framework for a mass distribution containing a finite number of particles. This will be done by using the N-body Newtonian code GADGET.

Chapter 4

The quadrupole formalism in the numerical framework

4.1 Gravitational Wave signatures from supernovae core bounce using Smooth Particle Hydrodynamics (SPH)

In the previous sections the GWs produced by SN core bounce were investigated using an analytical method (multipole expansion of the mass distribution). In this chapter we produce core bounce GW signatures using a Newtonian numerical scheme (a scheme that ignores GR). The Smooth Particle hydrodynamic Newtonian numerical code, GADGET, was used to approximate the typical GW amplitude and the wave frequency range of core bounce events. This chapter aims at introducing readers to the numerical side of GW simulations; retrieving and running parallel code, as well as visualizing results. Full GR codes operate on the same principle. We use Newtonian codes to retrieve first order GW amplitude approximations for SN core bounce, it must also be mentioned that Newtonian codes can be used to generate crude upper limits for the GW strain produced by several systems and that full GR codes must rather be used if the user wishes to produce GW signatures in greater detail.

To retrieve the GADGET N-body code we refer the reader to the GADGET's web-site (<http://www.mpa-garching.mpg.de/gadget>). From this site the reader will find everything that is needed to get the code up and running (including examples). The reader must also note the technical side of the installation process (included in the supporting documents). This chapter does not include the detailed use of GADGET (such as the syntax or inputs).

To simulate a Newtonian sphere collapsing under gravity and bouncing due to resistant internal pressures, we use a formalism that is analogous to that of the quadrupole formalism. Smooth particle simulations are generally classified under N-Body numerical schemes, which are used for cosmological studies and the merging of binary compact objects. The code essentially uses a collection (or group) of particles to represent a fluid or an object. Unfortunately the code has shortcomings; in the field of subsonic turbulence the code fails to predict densities and GW signatures accurately (Springel, 2005; Abel, 2011). However, the code is an excellent hydrodynamical solver and appears to be robust. The code is also used to generate upper limits for the GW signatures from merging binary white dwarfs (detectable by LISA) or merging NSNS.

Let Γ be collection of particles (or a Newtonian sphere). In the SPH formalism Γ contains i discrete particles with certain masses (see Fig. 4.1 for a representation of such collection of particles). SPH allows one to define a smoothing function (W_{ij}) that smoothes out any disturbance (“action”) radially as an inverse function of radius (r^{-1}). The function W_{ij} represents a sampling kernel that selects and acts on a certain collection (or domain) of particles, also, this function is monotonically decreasing with relative distance and insures smooth derivatives per integration time step (it is this function the causes the code to fail in the field of subsonic shocks) (Springel, 2005).

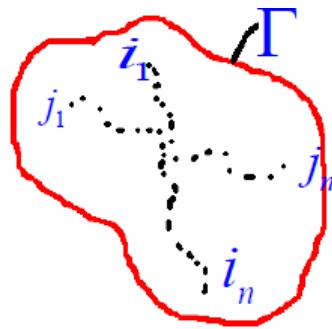


Fig. 4.1: The mass distribution Γ contains i discrete particles with certain masses. Typically the distribution could contain n pairs of neighbours (i_n, j_n).

The code allows the user to calculate some physical characteristics of the mass distribution such as the density of the system ($Dens(\Gamma) = \sum m_{ij} W_{ij}$) and the equations of motion of each particle (this is used to obtain the pressure and density of the system Γ). The code is based on the principle that the user defines the geometry of the mass distribution and the EOS, using the simple polytropic relation $P = k\rho^\gamma$. The code needs certain conditions as input: the total computational time, file output location, integration time step and the number of computer core nodes for the run.

The main aim of this chapter is to modify the GADGET code to include the quadrupole formalism in the inner schematics of the code. The GADGET code was constructed for parallel computing (which means that arrays/blocks of data are processed faster each consecutive time step). The modification discussed in this chapter is still a serial code structure (since this choice simplifies the coding procedure). No GW back reaction was implemented in the code due to the length and complexity of the code (Springel, 2005). Following the approach of Zhuge (1994), the SPH quadrupole tensor was constructed

$$\begin{aligned} Q_{lm} &= \int \rho x_l x_m dV \Rightarrow \hat{Q}_{lm} = \int \rho [x_l x_m - \frac{1}{3} \delta_{lm} r^2] dV \\ \ddot{Q}_{lm} &= \int [2\rho v_l v_m + 2P\delta_{lm} - \rho(x_m \partial_l \Phi + x_l \partial_m \Phi)] dV \\ \ddot{Q}_{lm}^{SPH} &= \sum_i^N m^i [2v_l^i v_m^i + 2(P^i / \rho^i) \delta_{lm} + (x_m^i g_l^i + x_l^i g_m^i)]. \end{aligned} \quad (4.1)$$

Here v^i, g^i, ρ^i and P^i represents the velocity, the gravitational potential, density and pressure experienced by each particle. These parameters are determined by the smoothing function (W_{ij}) that selects a small neighbourhood around each particle i and effectively determines the parameters $\{v^i, g^i, \rho^i, P^i\}$ in this neighbourhood. Once the code has calculated the components of the quadrupole tensor for each time step, the data is converted to a GW strain (Zhuge, 1994)

$$h_+ = \frac{G}{Dc^4} (\ddot{\mathcal{T}}_{xx} - \ddot{\mathcal{T}}_{yy}). \quad (4.2)$$

The wave has characteristic amplitude (Zhuge, 1994)

$$A_+ = \frac{8Dh_+}{\sqrt{15/\pi}}. \quad (4.3)$$

This formalism fits well inside the code, since all the required information exists for each time step in data array structures (accessible in one of the sub structures of the code). For illustration purposes the code is presented in Appendix D (the code contains the implementation of the numeric quadrupole mass moment and GW generation).

One of the main obstacles in of GADGET code is to provide initial mass structures, such as the core structure of the SN, approximated in this case with a Newtonian sphere (it is much harder to produce more than one structure on the grid and oddly shaped objects are difficult to create mathematically). The initial mass structure code is presented in Appendix D.

To investigate the GW signatures from core bounce, one needs to keep in mind that there exist fully relativistic codes that incorporate all the necessary micro and macro physics to produce a general relativistic core bounce GW signature. Numerical relativists invest enormous effort trying to solve problems like these (see Chapter 1 and Appendix A). The GADGET code however is purely Newtonian and does not include physics such as neutrino emission and neutrino driven instabilities. Newtonian codes produce quick and approximate methods for the generation of GW signatures, but over estimate the main GW signatures associated with, for example, SN core bounce (for reasons that will be mentioned later). Nevertheless, it provides a vehicle to determine upper limits for GW signals produced in various classes of astrophysical events. I will now present a few examples will be presented for illustration purposes of the capabilities of the code.

To initialize and test the modified GW N-body code (GADGET) we performed two test simulations; a collapsing core of particles. The second was of the collision of two very dense spheres of particles. These test-runs were performed to investigate the effectiveness of the code and the modified GW GADGET part of code (see extracts of code in Appendix D). Firstly, a non-rotating collapsing core of particles (with radius $r \sim 10^7$ cm, $\rho_{core} \sim 10^{14}$ g cm $^{-3}$ and $\gamma = 5/3$) was used as a test simulation. The visualization of the data produced by the test run was done by using SPLASH (Springel, 2005). See Fig. 4.2.



Fig. 4.2: A typical collapsing sphere, this event happens over several simulation time steps (the axis is in normalised units). The core shrinks and bounces. The colour-bar included in each Figure represents a density scale in normalized units. Time steps are in free falling time given by $t_{ff} = \sqrt{3\pi/32G\rho_{core}}$.

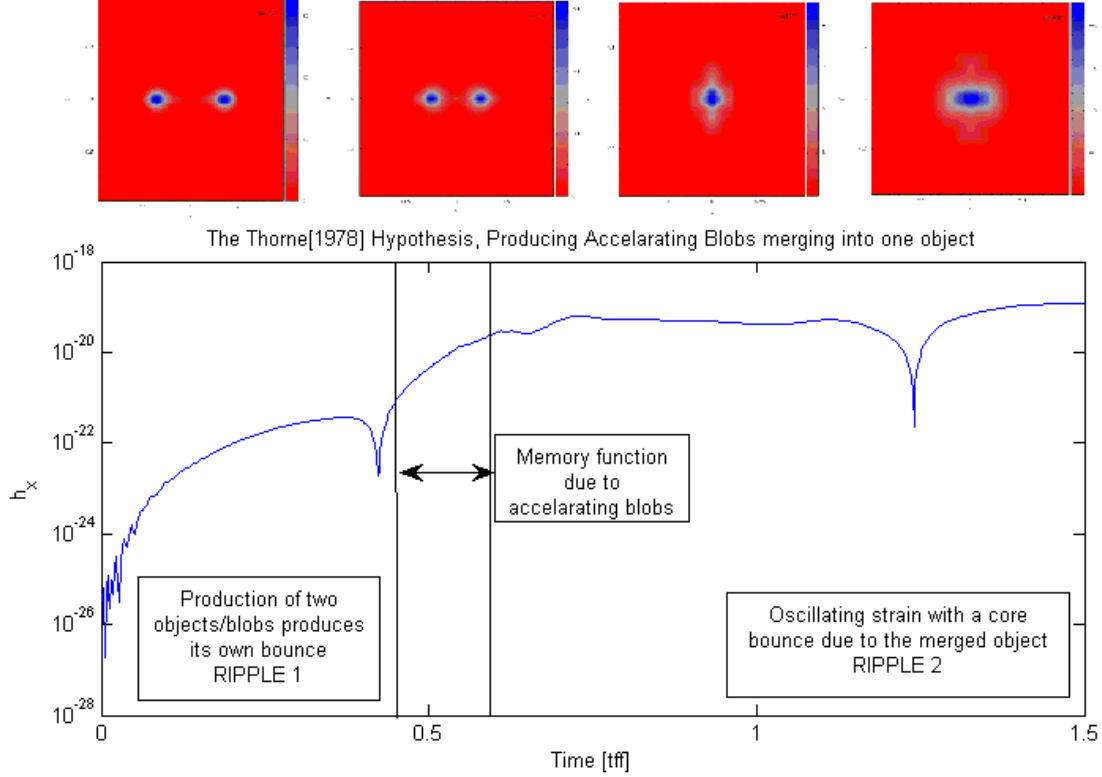


Fig. 4.3: Two dense objects crashing into one another. Each has $r \sim 10^7$ cm and $\rho_{core} \sim 10^{14}$ g cm $^{-3}$, at a distance $d \sim 10$ kPc from earth. The accompanying graph shows the log of the amplitude vs. time. The time steps are in units of free falling time $t_{ff} = \sqrt{3\pi/32G\rho_{core}}$ (Muller, 1991).

These two test GADGET simulations (see Fig. 4.2 and Fig. 4.3) confirm that one can construct Newtonian cores to simulate SN core collapse, and that one can also manipulate these objects to simulate different GW signatures. Fig. 4.3 illustrates the different GW signatures produced by two very dense objects in collision, the GW burst and ringing signatures will be detected up to a distance of a megaparsec with AdvLIGO. After testing the setup files and confirming that a core like object (see Fig. 4.2 and Fig. 4.3) can be created using the GADGET code, we implemented a more realistic core structure. Muller (1991) investigated core bounce mechanisms using hydrodynamic simulations. He considered models with different masses, rotations, central densities and density profiles. We used Muller's Model B (1991). This model initializes a core arising from a $20M_\odot$

progenitor star (having central density of $\rho_{core} \sim 10^{14} \text{ g cm}^{-3}$, $r \sim 10^8 \text{ cm}$, $M_{core} = 1.6M_\odot$ and relativistic adiabatic index of $\gamma = 4/3$). This is the same model that we investigated analytically in Section 3.2.

The above initial conditions were implemented in GADGET, using the setup files described above, to simulate core collapse and bounce. The simulation was repeated and the core was intentionally rotated (giving each particle angular velocity), see Fig. 4.4.

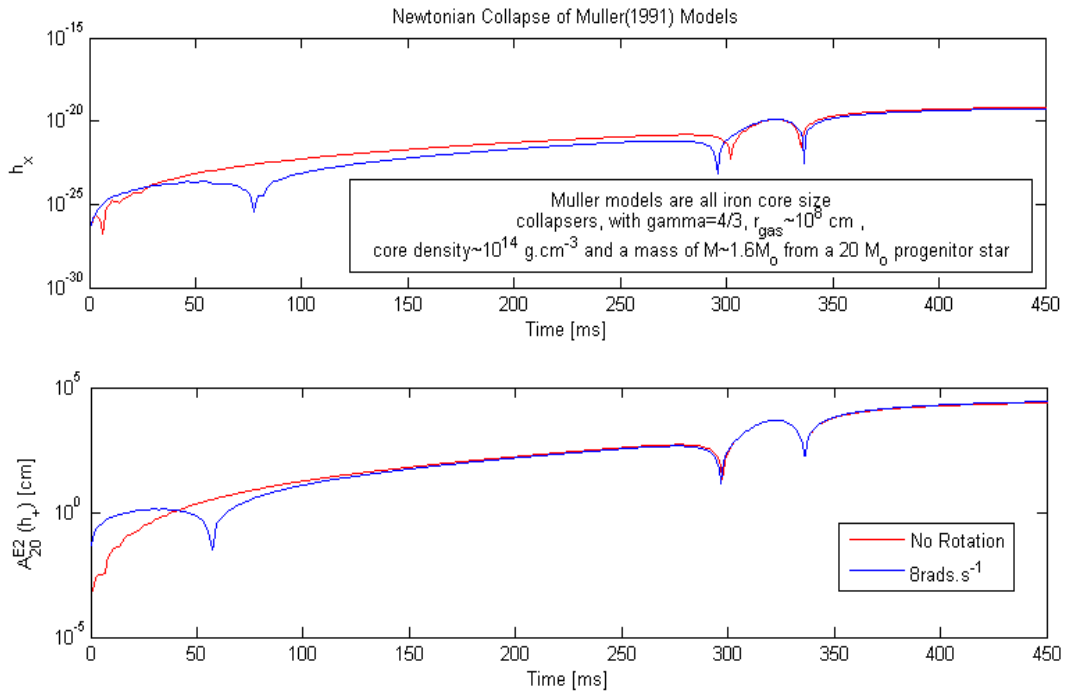


Fig. 4.4: GADGET simulation of model B. The dynamical time scale of the bounce is in milliseconds. The amplitude and the strain are plotted using a log scale, and the source (the core bounce event) occurs at a distance of $d \sim 10 \text{ kPc}$ from Earth.

The bump at time $t \sim 350 \text{ ms}$ corresponds to the bounce phase of the collapse. No GW back reaction was implemented in this modified GADGET extension code. The bounce causes a ripple in spacetime with dynamical frequency in the kHz range. The small cusps in the early stages of the collapse are due to a numerical imperfection (the code rearranges the particles slightly when the algorithm starts).

The collapse illustrated in Fig. 4.4 is a potential candidate as a source for AdvLIGO observed GWs due its favourable GW strains and frequency (see Fig. 1.6 in Chapter 1), since the characteristic frequency of the burst core bounce GW signature ($f \sim \text{kHz}$) and the characteristic strain ($h \sim 10^{-21}$) falls into the detection window of AdvLIGO (see Fig. 1.8 in Chapter 1). The results obtained by this numerical treatment of the core collapse also correspond to that found analytically in Section 3.2. The modified code can only provide upper limits for the GW strain from such core collapse events since it is Newtonian in structure. However comparing the predicted GW signatures with that predicted by relativistic codes, the main problem quickly becomes evident, see Fig. 4.5.

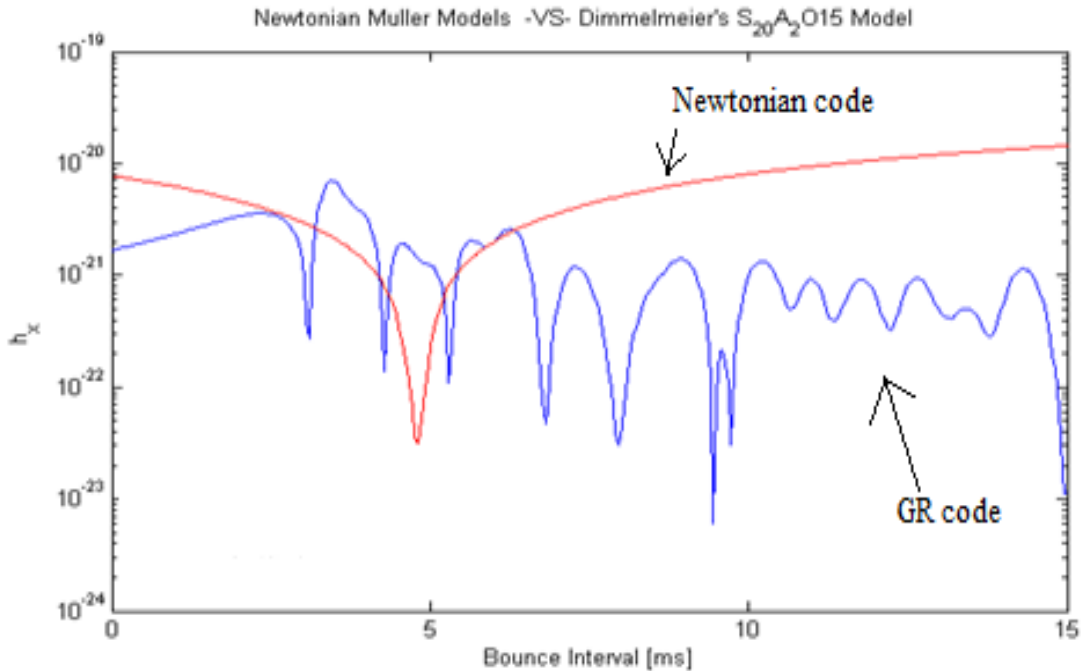


Fig. 4.5: Log scale plots of two different generations of SN core bounce codes (Newtonian codes and full relativistic codes). Both codes used the same core structure, containing 15 ms of the core bounce phase as predicted by both generations of codes (Dimmelmeier, 2002). Dimmelmeier's model $S_{20}A_2O15$ is equivalent to Muller's model B (Muller, 1991).

The Newtonian SN core bounce phase occurs later than the GR bounce. The GR core bounce is typically followed by several bounces (ringing phase). GADGET contains no GW back reaction, neutrino emission or framework of nuclear density. Neutrino emission during SN collapse plays a role in producing instabilities after the core bounce. Moments after the bounce, a burst of neutrino flavours are released from the core. We only consider electron capture neutrinos in this chapter, which could typically cause convectional instabilities and neutrino driven shocks.

It is known that escaping neutrinos generate a memory GW signature (this signature was first proposed by Thorne, 1980). During neutrino emissions caused by electron capture, a vast amount of neutrinos are emitted from the proto neutron star like object (one of the earliest remnants of the SN collapse). Using the data produced by Thompson (2003) for the luminosities of the ν_e -emission (for a $20M_\odot$ progenitor star over a time span of a few milliseconds), together with the neutrino memory waveform in Muller (1997) and Thompson (2003), we plotted the memory of the GW signature. This plot is displayed in Fig.4.6 and Fig. 4.7.

Neutrino emission is one of the post bounce processes that radiate away a large amount of energy in a short amount of time. If a neutrino is emitted with typical energy $E_\nu = 1 \text{ MeV}$ (Zhuge, 1994),

$$\begin{aligned} \lambda &= 200 \left(\frac{E_\nu}{10 \text{ MeV}} \right)^{-1} \text{ fm} \\ \tau_\nu &\sim 10 \left(\frac{r_\nu}{10 \text{ km}} \right) \left(\frac{E_\nu}{10 \text{ MeV}} \right) \left(\frac{\rho_{\text{core}}}{10^{14} \text{ g cm}^{-3}} \right) \text{ ms.} \end{aligned} \quad (4.4)$$

Here λ, τ_ν, r_ν and ρ_{core} are the wavelength of the neutrinos, the emission time scale, neutrino radius (the shell that encapsulates the neutrino burst event, chosen to be $r_\nu = 10 \text{ km}$) and the typical core density.

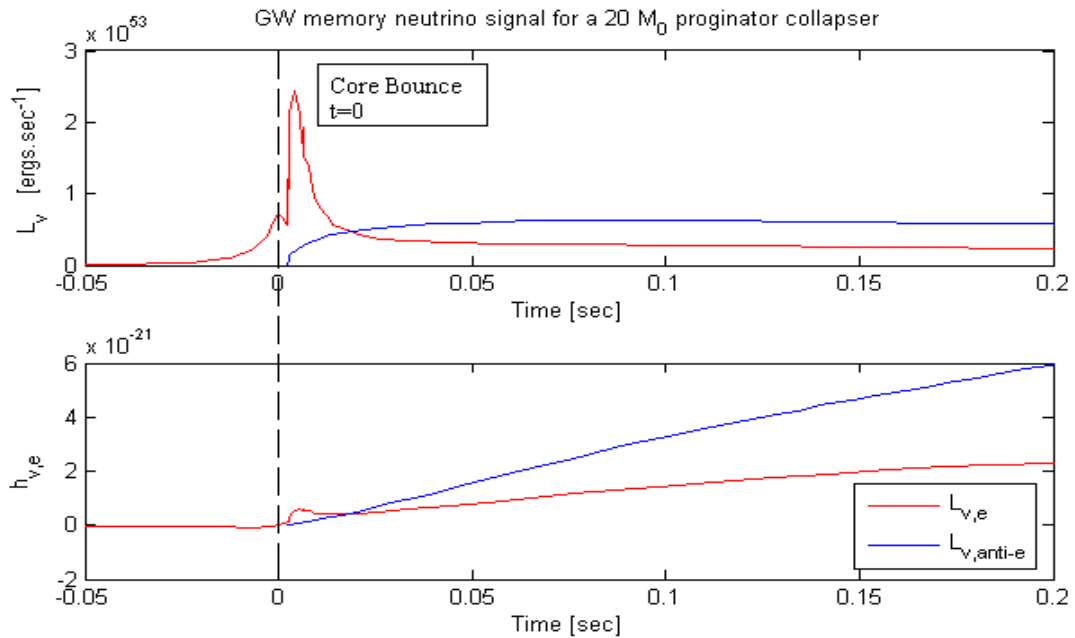


Fig. 4.6: Electron-capture neutrino emission; the neutrinos follow a memory waveform described by $h_\nu = (1.6 \times 10^2 \text{ cm}) \frac{L_\nu}{10^{52} \text{ ergs s}^{-1}} \left(\frac{\alpha}{0.1} \right) \frac{1}{D} \left(\frac{\Delta t}{1 \text{ sec}} \right)$, for $\alpha = 1$. This signal is a low frequency signal ($f_{dyn} \sim 100 \text{ Hz}$) compared with the bounce phase GW signal (Thompson, 2003).

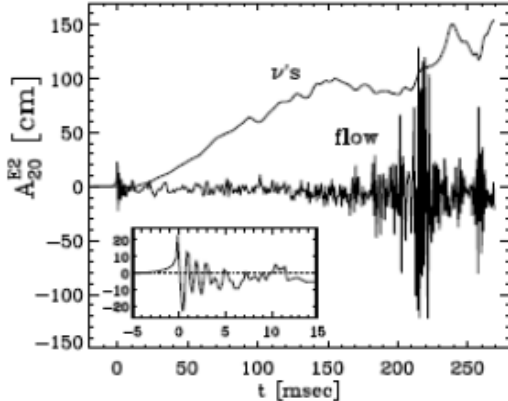


Fig. 4.7: After the core bounce phase, the GW memory signal from neutrinos strengthens and, at some stage, produces neutrino driven instabilities (convection in the core region) that strengthen the general GW signal in the higher frequency range, since convectional instabilities have a dynamical timescale of milliseconds (from Zhunge, 1994).

There exist many codes that implement full General Relativistic algorithms for SN collapse and neutrino emission from a proto neutron star like remnant. Neutrinos play a very important role in the characteristics of the GW signal after the bounce phase. The GADGET code is a robust Newtonian code that supports OpenMP (the capability of parallel computing) and is very user friendly. This code was used to produce several upper limits for the possible observed GWs from SN core bounce. We refer the reader to references such as Reisswig et al. (2011) if he wishes to perform SN simulations that include more detailed physics (in the GR framework). Modern day codes such as the Einstein Toolkit (Reisswig et al., 2011), contain all the relevant physics to produce GWs from core collapse SN. These codes will be utilized in a more quantitative follow-up study.

In the next Chapter, we will investigate the role of the SKA in the field of GW astronomy. The SKA is planning the first detection of GWs using Pulsar Timing Arrays (PTAs) which will be sensitive to Stochastic GW backgrounds (see the low frequency window of Fig. 1.8b) produced by merging binary super massive black holes. In Chapter 5 we will also be looking at the galactic center (GC) as a possible GW nursery.

Chapter 5

Pulsar Timing Arrays (PTAs) and detecting Gravitational Waves from the galactic center

In the preceding sections the GW signatures of waves emitted by several classes of astrophysical sources (or events) have been discussed. In this Chapter we will discuss briefly the role the SKA is expected to play in the field of GW astronomy.

5.1 SKA Pulser Timing Arrays

Precision radio measurements of binary pulsar systems have provided us with an exquisitely accurate tool to test General Relativity. Tracking pulses from the Hulse-Taylor system (PSR913+16), to an accuracy of 15 microseconds for example, has yielded the first accurate determination of neutron star masses using relativistic timing effects. The measured decrease in orbital radius of binary pulsar systems is consistent with the energy loss predicted due to the emission of Gravitational Waves (GW) from the binary system (Pitkin, 2011; Peter, 1963). Other astrophysical phenomena such as, among others the recently much discussed, “kilonova” (CGWAS 2013, www.cgwas.org) can potentially be associated with binary neutron star merger events. Binary pulsar systems are the most likely sources for earth based gravitational wave detectors such as LIGO. See Fig. 5.1.

Fig. 5.1 illustrates the detection window of LIGO when observing GWs from merging binaries. These binaries remain in the AdvLIGO band for several days and could trigger radio follow-up or source localization by the SKA. This characteristic detection window of LIGO supports the idea of a multi-messenger network, which will be discussed in a later section.

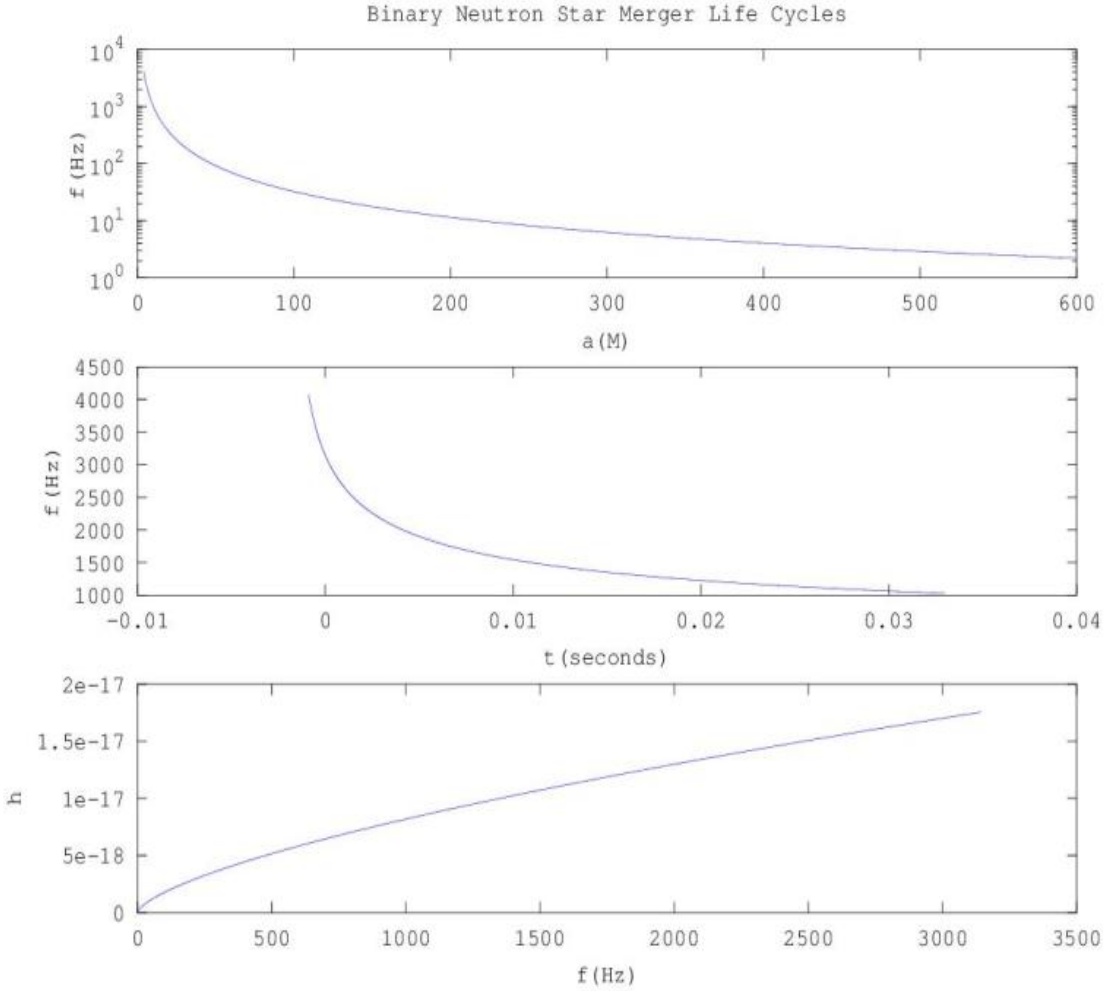


Fig. 5.1: Primitive inspiral modulation using Kepler's law to illustrate the strain h on the GW frequency. It is apparent that at some stage of the binary system inspiral the GW signal enters the LIGO band (3-3000 Hz). Here M represents the Schwarzschild radius of the neutron star. The merging event of two neutron stars is defined by a unique inspiral phase; as these neutron stars move closer to one another, the amplitude and the frequency of the GW increase.

The SKA is expected to be the most sensitive radio telescope in the history of science, with faster surveys than the Arecibo and Parkes radio telescopes (Aharonian et al., 2013). The SKA is planning the challenge of the first GW detection; observing several ms pulsars (the Einstein clocks in the universe) in vast arrays over the sky.

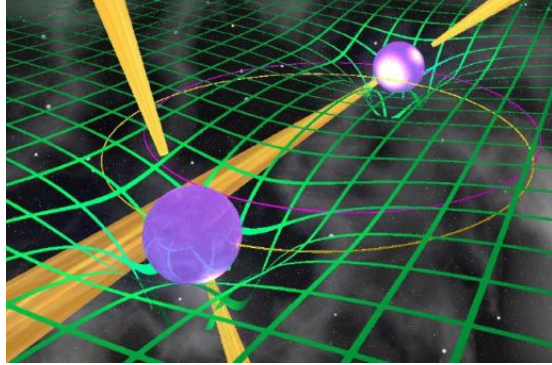


Fig. 5.2: Artist's impression of the concept of PTAs (from Aharonian et al., 2013).

These arrays are known more formally as Pulsar Timing Arrays (PTAs). To introduce PTAs, we started with the argument: there exist a frequency emitter (f_e) far away and some receiver (f_r). Let (f_e) emit continuous pulses with a certain frequency. These signals propagate through space, which may be filled with GW disturbances. These will have a direct effect on the transmitted signal, effectively dispersing the signal. One could insert and remove the disturbance periodically and generate a periodic noise. Ultimately the SKA and the proposed PTA project will detect stochastic GW backgrounds; a background GW signal that is produced by the superposition of several GWs signals into one background noise (Aharonian et al., 2013).

Consider Earth and one pulsar form one leg of an interferometer, and let the pulsar emit sharply defined regular pulses towards to the Earth. If a GW passes between this pulsar and Earth the effective path length of the photon will be changed introducing a small perturbation (noise) in the timing data (Hobbs, 2012). We constructed an array of pulsars containing only two pulsars in the sky with unit directional vectors $(\hat{n}_1^i, \hat{n}_2^j)$ (Hobbs, 2012), then the time of arrival becomes (assuming that the GW propagate in the z -direction)

$$TOA = t_{\text{emitted}} + D + \frac{1}{2} \int_{t_e}^{t_r} h_{ij} \hat{n}_1^i \hat{n}_2^j dt. \quad (5.1)$$

The perturbation in the background metric is given by h_{ij} (this is the disturbance created by the GW and represents the small ripples in spacetime). This “disturbance” in the background metric was derived from basic GR concepts (Hobbs, 2010). If the perturbation is of flat space ($g_{ij} = \eta_{ij} + h_{ij}$), then the assumptions of null geodesics (for propagating photons $ds^2 = 0$) explains the extra travel time term due to the disturbance (to first order)

$$dt = dr \left(1 + \frac{1}{2} \hat{n}_1^i \hat{n}_2^j h_{ij} \right). \quad (5.2)$$

Thus the time of arrival (TOA) will contain some GW induced noise. After introducing some geometrical constructions and reparameterizing the integral, with the angle between the directional vectors (\hat{n}_i, \hat{n}_j) given by the angle θ (Hobbs, 2010), then

$$TOA = t_{\text{emitted}} + D + \int_0^D h_{ij} [(t - t_{\text{emitted}})(1 - \cos \theta) + t_{\text{emitted}}] \hat{n}_1^i \hat{n}_2^j d(t - t_{\text{emitted}}). \quad (5.3)$$

Here $h_{r,ij}$ and $h_{e,ij}$ represent the GW induced perturbation at the Earth- and pulsar end of the timing array respectively, and D is light travel time from the pulsar to the detector (see Hobbs (2010) for an overview on PTAs). This induces a frequency shift,

$$\frac{\delta\nu(t)}{\nu} = \frac{\hat{n}_1^i \hat{n}_2^j}{2(1 - \cos \theta)} (h_{r,ij} - h_{e,ij}), \text{ and a timing noise, } R(t) = -\int \frac{\delta\nu(t)}{\nu} dt, \text{ in the pulsar}$$

timing data. If one assumes a PTA containing n pulsars then the main problem would be the correlation between the observed signals (how do we know that all of our pulsars in the array experienced the identical GW?). Luckily there exists a correlation between the signals observed the Earth end of the array. This correlation could be constructed using

two pulsars with directions $(\hat{n}_1^i, \hat{n}_2^j)$. Of particular interest is the correlation function between these two pulsars (Hobbs, 2010) at the Earth-end of the interferometer arm

$$\alpha(\hat{n}_1, \hat{n}_2) = 0.08 \sum_A \int \frac{e_{ij}^A \hat{n}_1^i \cdot \hat{n}_2^j}{2(1 + \hat{k} \cdot \hat{n}_1)} \frac{e_{ab}^A \hat{n}_1^a \cdot \hat{n}_2^b}{2(1 + \hat{k} \cdot \hat{n}_2)} d^2 \hat{k}. \quad (5.4)$$

Here $A = (+, -)$ and \hat{k} represents the direction vector of the GW. Also, $d^2 \hat{k}$ represents the unit sphere of GW propagation direction \hat{k} , here both e_{ij}^A and e_{ab}^A are polarization and the indices $\{i, j, a, b\}$ serving as integers. The correlation could be seen if one calculates the correlation of 100 pairs of pulsars and $N = 1000$ random cycles of different \hat{k} directional GW vectors, assuming the fact the each GW directional wave could be decomposed into orthonormal vectors in the $\hat{\phi}$ and $\hat{\theta}$ direction, see Fig. 5.3.

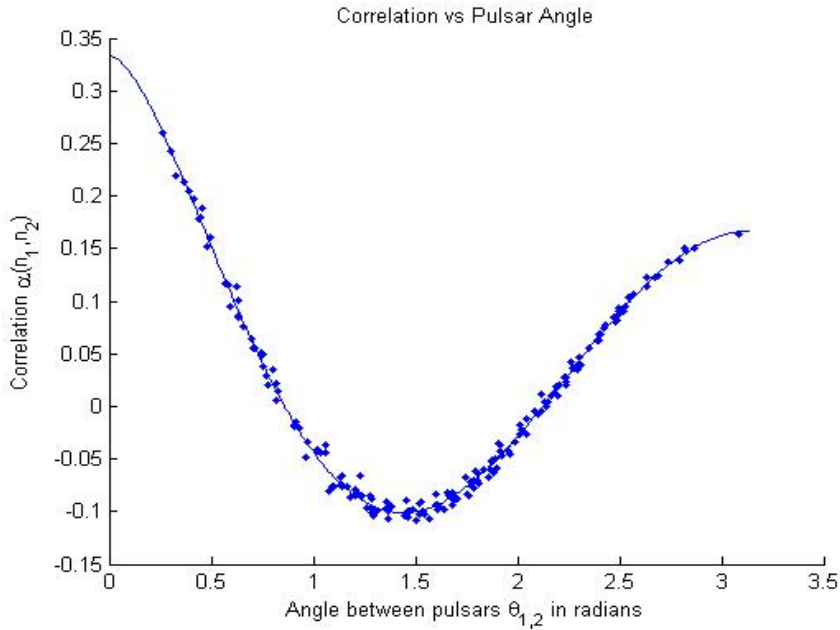


Fig. 5.3: The correlation function of 100 pairs of pulsars at the Earth end of the PTA. This correlation function (Hobbs, 2010) is described by the formula:

$$\alpha(\hat{n}_1, \hat{n}_2) = \frac{1 - \cos \theta}{2} \log \left[\frac{1 - \cos \theta}{2} \right] - \frac{1 - \cos \theta}{12} + \frac{1}{3} \quad \text{that represents the solid fitted line}$$

through the correlation points. This figure was produced in MATLAB.

If the SKA were to observe a pulsar for $T = 10$ yr with sufficiently accurate timing, it would be possible to construct PTAs that can be used to detect low frequency GW sources of the order of $f \sim \text{nHz}$ (Aharonian et al., 2013). The GW noise in timing data was investigated theoretically by using pulsar timing simulation packages such as TEMPO2. This package allows users to specify which GW background is present, whether it is due to a stochastic background or a single periodic source. The code operates using two input files: an ephemeris log file and a file containing the simulated pulsar timings for any number of pulsars (Hobbs, 2010). The ephemeris file contains information such as the pulsar name, right ascension, declination, first and second derivatives of the frequency, and the observed arrival times in modified Julian years. Any pulsar observation includes measurements of the Time of Arrivals (TOAs). The TEMPO code converts the TOAs to time of emission by applying all the known transformations to the timing data file. These “corrections” include the Solar System barycentre, delays due to the interstellar medium, and the transformation to the pulsar frame of reference. Then the time of emission can be compared to the pulsar model to produce timing residuals (Hobbs, 2010). The concepts of PTAs were tested with the TEMPO code by retrieving an array of targeted SKA pulsar ephemeris files (J2124-33, J1807-08, J1900-30, J1038+00 and J0030+04). The TEMPO code uses these files to create a grid and simulate timing residuals for each pulsar (see Fig. 5.4 and the sample ephemeris file).

The main aim with PTAs will be the detection of low frequency GW backgrounds due to merging Super Massive Black Holes (SMBH) in other galaxies. The coalescence of these binary systems produces characteristic GW amplitudes of $A_g \sim 10^{-14}$. The strain spectrum of a GW background is generally a power law of the GW frequency (Hobbs, 2010),

$$h_c \sim A_g \left(\frac{f_g}{\text{yr}^{-1}} \right)^\alpha,$$

and is produced by the slow orbiting patterns of binary SMBs. This

GW background could induce a considerable noise in the timing residuals of a pulsar array, see Fig. 5.5.

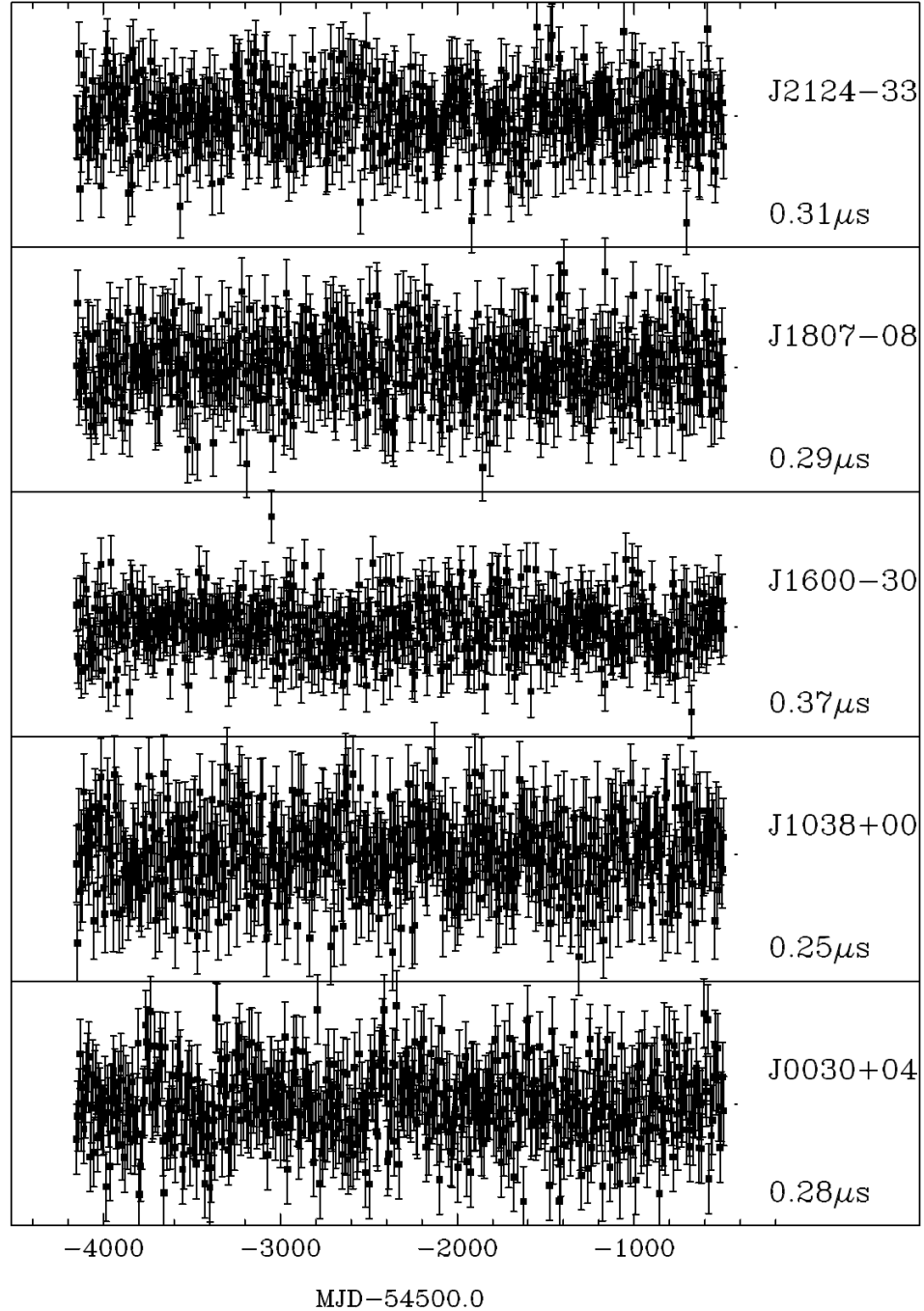


Fig. 5.4: Timing residuals for the pulsars that form part of an array of five SKA pulsars. There is no GW noise present. The residuals were produced for each pulsar by comparing the emission time of each pulsar to the standard pulsar model (Hobbs, 2010).

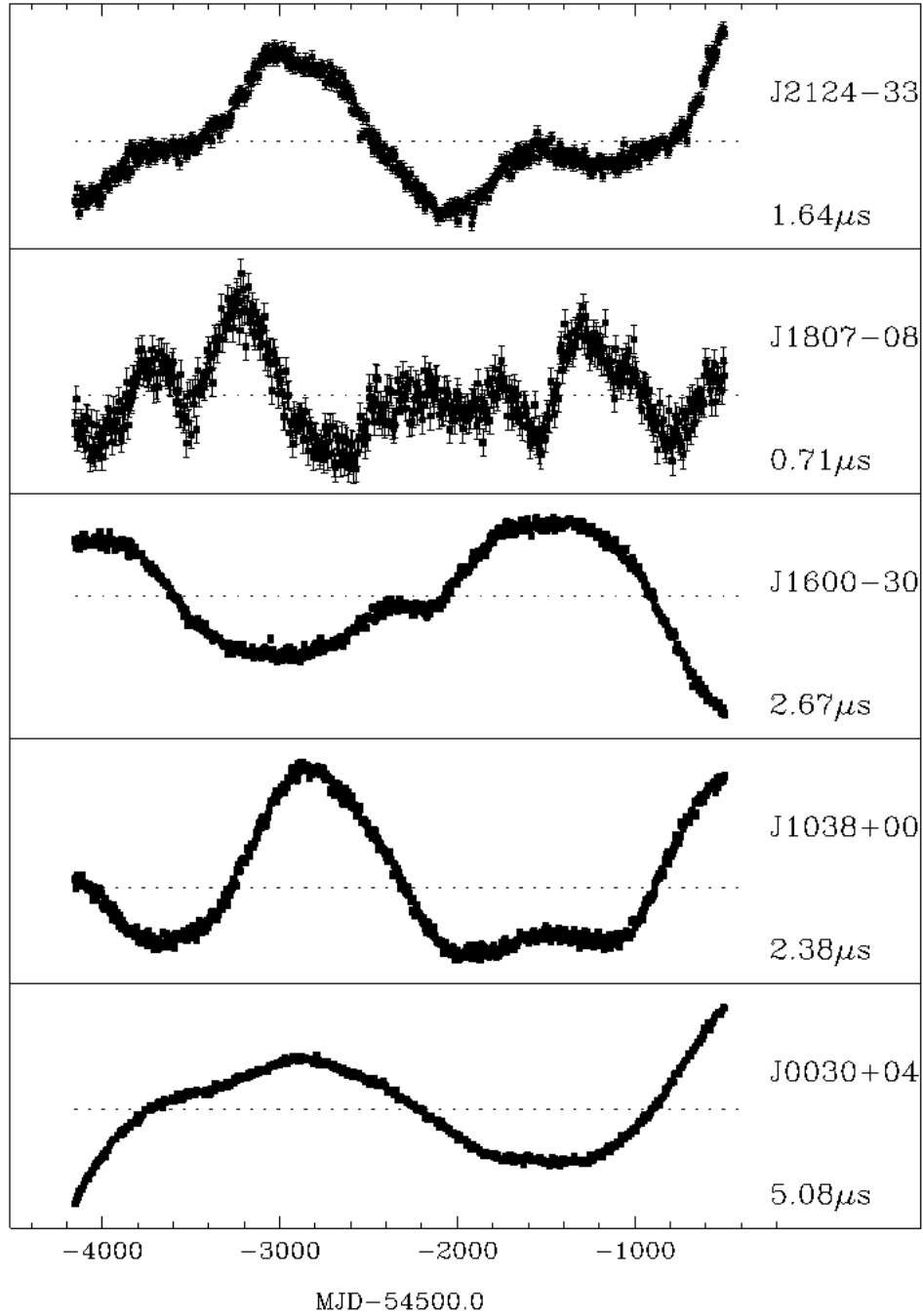


Fig. 5.5: Timing residuals produced for an array of five SKA pulsars by using their known ephemeris files. A binary SMBH GW “noise” was chosen with $A_g \sim 10^{-14}$ and $\alpha = -\frac{2}{3}$ (Hobbs, 2010).

```
/////////////////*Sample ephemeris file*/////////////////
```

<i>PSRJ</i>	<i>J2124-3358</i>		
<i>RAJ</i>	<i>21:24:43.85350</i>		<i>4.000e-05</i>
<i>DECJ</i>	<i>-33:58:44.668</i>		<i>1.000e-03</i>
<i>DM</i>	<i>4.5956</i>		<i>2.000e-04</i>
<i>PEPOCH</i>	<i>53174.0</i>		
<i>F0</i>	<i>202.793897023854</i>	<i>1</i>	<i>9.000e-12</i>
<i>F1</i>	<i>-8.468E-16</i>	<i>1</i>	<i>9.000e-19</i>
<i>PMRA</i>	<i>-14.4</i>		<i>8.000e-01</i>
<i>PMDEC</i>	<i>-50</i>		<i>2.000e+00</i>
<i>START</i>	<i>52649</i>		
<i>FINISH</i>	<i>53485</i>		
<i>EPHEM</i>	<i>DE200</i>		
<i>RM</i>	<i>1.2</i>		<i>1.000e-01</i>
<i>PX</i>	<i>4</i>		<i>2.000e+00</i>
<i>EPHVER</i>	<i>5</i>		

```
/////////////////////////////
```

Fig. 5.4 and Fig. 5.5 were produced by using five standard SKA targeted pulsars, together with their ephemeris files. These were provided by Hobbs (2008). We used one of the extensions of the Tempo2 code (called GWbkgd) together with all the necessary files describing the pulsars to investigate the influence of the GW disturbance on the pulsar timing residuals. The standard pulsar timing noise (without any GW noise) produced a noise with amplitude of $A \ll \mu s$. If a stochastic GW background is present the noise level increases to typical values of $A \gg \mu s$. However, there exist a number of problems with the concept of PTAs. The noise in the pulse arrival times of the pulsar (so called red pulsar noise) increases as the observation time increases. At some stage this red noise enters the GW noise band, complicating the decomposition of the various noise signals a very complex task to perform. The SKA is expected to observe single pulsars in binaries to indirectly observe the effect of GWs (as it was done for the Nobel Prize winning observation of PSR 913+16 (Taylor, 1982)).

5.2 Conclusion: Gravitational Waves from the galactic center

Our galaxy contains a nursery of rich stellar clusters in the direction of the constellation of Sagittarius at least a distance of $d \sim 8$ kpc from Earth). Hidden behind a thick screen of interstellar material (or plasma), lurks a dark massive object at the center of our Milky

Way (Genzel, 2010). This nursery is the center in our galaxy (GC). Having interesting X-ray, radio and infrared spectra, from which it appears that the galactic center harbours more than just dense stellar clouds. This object is assumed to be a rotating supermassive Kerr black hole with multiple objects in close orbit around it. This super-massive black hole (SMBH) (Also known as Sgr A*, due to the fact that the SMBH coincides with the position of the radio source Sgr A* in the GC). It is the nearest strong gravity source to Earth (Genzel, 2010). There exist a collection of stars orbiting the assumed SMBH inside the central parsec of the GC, known as the S-stars. These stars orbit Sgr A* in complete Keplerian orbits and allow astronomers to monitor Sgr A* very accurately (Gillessen, 2009). See Fig 5.6.

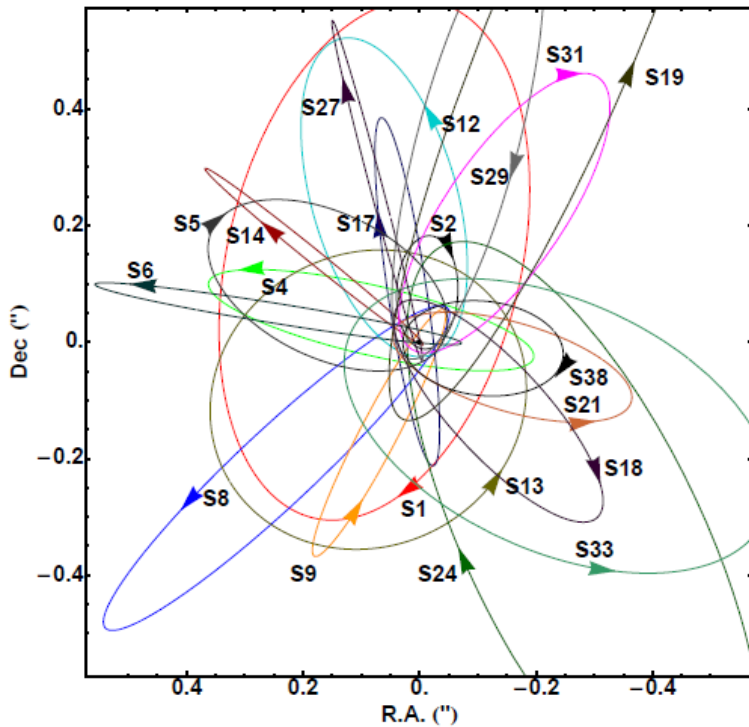


Fig. 5.6: The collection of S-stars that orbits Sgr A*, the mass of the black hole (which is roughly a million times the mass of the sun) was determined by close observations of the closed orbit of the star S2 (from Gillessen, 2009).

Since Sgr A* is a stable strong gravity source in the GC and is hidden behind an instellar screen. It allows one to test the no-hair theorem (Geroch, 1971) and the effect of pulse broadening of a pulsar orbiting Sgr A* (Lui, 2012; Gair, 2012). It has been showed by

Liu et al., (2012) that if one could observe a stable pulsar at 15 GHz orbiting Sgr A* with a period of one year, an observer would be able to determine the quadrupole moment of Sgr A* with a accuracy of less than 1 in 100.

There also exist Extreme Mass Ratio Inspirals (light object orbiting a heavy object) and produces interesting GW signatures and orbits with chaotic resonating frequency counterparts (Gair, 2012). This GW source will be observable in the eLISA frequency band ($f \sim 10^{-4} - 10^{-1}$ Hz). The SKA will probe the ultra-low GW frequency band ($f \sim \text{nHz}$) via PTAs and LIGO will probe GWs in the frequency band of $f \sim 3 \text{ Hz} - 3 \text{ kHz}$. Sgr A* holds an interesting characteristic of not having steady strong accretion rates. Strategically positioning Meerkat and ultimately the SKA to be able to follow up on gravitational wave detection (by LIGO) of binary pulsars could potentially result in some very exciting modeling of merger physics. The project of doing targeted searches using LIGO for the gravitational wave emission of binary pulsars systems discovered by the SKA to place upper bounds on the gravitational waves emitted from these systems could be an equally fertile test bed for precision tests of General Relativity.

Chapter 6

Conclusion

Gravitational Wave astronomy will give us access to the Universe's "soundtrack" (3-3000 Hz) within the next decade; opening a new and exciting observational window on the Universe. Ground based interferometers (such as LIGO/VIRGO) and radio telescopes (such as the SKA) are planning to detect Gravitational Waves through unique experiments that use either reflected light between two mirrors or observations of pulses from pulsars. Both LIGO and the SKA are in an advanced phase of development and rely currently on modelling related to GW detection using interferometers or pulsar timing arrays. This necessitated a theoretical study that focuses on retrieving upper limits for the GW amplitude and frequency of various LIGO and SKA Gravitational Wave (GW) sources such as collapsing supernovae, rapidly spinning magnetars and the coalescence of compact binary objects. Upper limits for the GW amplitudes and frequencies were retrieved by means of numerical and analytic methods. A core result this project was the identification of short period (transient) GW signatures, within the framework of the standard quadrupole formalism.

There exist several methods of modelling GWs from different sources that could be implemented in several platforms such as SPH numerical schemes and the quadrupole formalisms of spinning and collapsing stellar objects. Many of these GWs are detectable by modern day detectors such as LIGO, SKA or eLISA. It is also evident that accompanying the theory of GW production are mathematical tools that were studied and presented in this thesis (Chapter 2 and Appendices). This opens the opportunity to study GW sources in the GC and hopefully allows for the testing of GR using the SKA and LIGO. To search and understand the GW sky, an observer needs to understand all the available methods and models used to describe these complex GW signatures. It will help

with the development of the space- and ground based interferometers (especially the templates that will be used to search for well-known GW sources). GW signatures produced by transient sources are classified according to a strain amplitude and frequency. Both LIGO and the SKA are sensitive to GWs with unique amplitudes and frequencies (see Chapter 1). We found that spinning neutrons stars, magnetars and supernovae produce burst/periodic GW signals (with characteristic frequencies $f \sim \text{kHz}$ and strain amplitudes $h \sim 10^{-21}$) that could be observed with LIGO (see Chapter 3 and Chapter 4). Numerical relativity groups are producing GW signatures from supernovae core collapse and binary mergers to high accuracy aiming at producing template banks for the use of LIGO/VIRGO. The simulation of GW signatures using numerical techniques produces detailed signatures that could be linked with multiwavelength astronomy (optical and gamma-ray bursts). In Chapter 4 we produced numerically (within the framework of Smooth Particle Hydrodynamics) GW signatures for supernovae core bounce events and linked the GW spectrum to neutrino emission from these events. The SKA is planning the first GW detection (see Chapter 5) by using Pulsar Timing Arrays (which are sensitive to GWs in the nanohertz frequency range produced by stochastic GW backgrounds). It is evident from this thesis that galactic transient sources produce unique GW signatures (bursts, period or stochastic backgrounds) that could be used in multiwavelength detector systems as triggers, e.g. neutrino and radio follow-up of GW triggered supernovae core collapse (see Chapter 4).

In this study we matched a GW signature to each galactic transient source. Given all that we discussed, what can we learn from detecting Gravitational Waves from exotic objects such as neutron stars, magnetars and binary mergers? The fundamental consequence of GW detection is the test of Einstein's Theory of Relativity. If no GWs are detected it implies that there exists serious short-comings in our predicted event rates. However, any proof of the existence of GWs will allow us to probe black hole spacetimes, observe binary inspirals as standard sirens and link the unique GW signatures of transient sources to other parts of the electromagnetic spectrum. Gravitational wave astronomy will hopefully improve our understanding of the Universe and all the sources in more detail than ever before.

GW astronomy will form a fundamental part of a multi-detector astronomy venture; it will ultimately be the most sensitive, and the earliest, trigger for SN core bounce and NSNSs coalescence. It is due to this that the proposed path for future projects includes integrating the SKA and LIGO in a joint detection strategy, since the SKA could observe pulsars to high accuracy, and LIGO is independent of any obstacles such as the interstellar medium. By combining observations of an array of millisecond pulsars the SKA will achieve a sensitivity of a few nanoseconds. This sensitivity could make detection of the signal coming from the cosmic population of Massive Black Hole (MBH) binaries. One possible extension of this study is to search for new radio pulsar candidates for possible GW wave signature studies by utilizing the Fermi-LAT bright source catalogue of unidentified sources. It is anticipated that more than 200 millisecond pulsar candidates still lurk within the sample of unidentified Fermi-LAT sources. By performing a spectral analysis of the gamma-ray data above 300 MeV, pulsar candidates can be identified and selected for follow-up observations with the Arecibo radio telescope in Peru and the Parkes telescope in Australia (since these radio telescopes meet the necessary sensitivity requirements). Detailed observations with MEERKAT (in a few years time) will enable us to identify GW effects on the pulse profiles, possibly leading to the firm establishment of GW astronomy as a discipline on its own.

Bibliography

Einstein, A, Koniglich Preußische Akademie der Wissenschaften Berlin, Sitzungsberichte (1915), 831.

Einstein, A, Koniglich Preußische Akademie der Wissenschaften Berlin,Sitzungsberichte (1916), 688.

Aansi et al., arXiv:1309.4027v1 [astro-ph.HE], 16 September 2013.

Abel, T., “A novel smoothed particle hydrodynamics algorith”, arXiv1003.0937, astro-ph.CO, May 2011.

Adler, R., “Gravitational radiation from SN explosions”, Phys.Rev.D, 1975.

Aharonian et al., “Pathway to the Square Kilometre Array”, arXiv:1301.4124v1 [astro-ph.IM] , 16 Jan 2013.

Anderson, N. et al., “The Transient GW Sky”, ArXiv:1305.0816v1[gr-qc], 3 May 2013.

Arnett, W. D., Bowers, R. L., 1977, ApJS, 33, 415.

Bernard Schutz, “A first course in general relativity”, 2009, p196-250.

Bonazzola et al., “GW from neutron stars”, <http://arXiv.org/abs/astro-ph/9605187v1>, 30 May 1996.

Blanchet, L., Damour, T., “Post-Newtonian generation of gravitational waves”, Ann. Inst. Henri Poincare A, 50, 377–408, (1989).

Burke, W.L, Thorne, K.S, "Gravitational Radiation Damping," in *Relativity*, eds. M. Carmeli, S.I. Fickler, L. Witten (Plenum Press, New York, 1970), pp. 209-228.

Brans,C., Dicke,R.H., Physical Review, 124,3, 1961.

Carlson, B.C., "Numerical Recipes", 10,13, 1995.

Chandrasekhar, S.,1953, ApJ,118,116C.

Chandrasekhar, S., ApJ, 161, 571C, 1970a.

Chandrasekhar, S., ApJ, 161, 571C, 1970b.

Dicke, R.H., Phys. Rev., 125, 2163, 1962.

Dimmelmeier, Font, Muller, Astron. Astrophys., 388, 917 {935} (2002), astro-ph/0204288.

Fryer, C., Kimberly, C.B, "Gravitational Waves from Gravitational Collapse", *Living Rev. Relativity* 14, (2011), <http://www.livingreviews.org/lrr-2011-1>.

Gair, J., "Improved approximation inspirals of test-bodies into the Kerr Black Holes", arXiv: gr-qc/0510129, 2012.

Genzel, R. "The galactic center massive black hole and stellarsensity clusters", arXiv 1006.0064, 2010.

Gerakopoulos. "Non-linear effects in non-kerr spacetimes". In proceedings: Relativity and Gravitation 100 years after Einstein in Prague, edition open access.

Geroch, R. “A method for generating Solutions of Einstein’s Equations”. Journal of Mathematical Physics”, 12:918-924, June 1971.

Gillessen, S., “The orbit of the star S2 around Sgr A* from VLT to Keck data”, ApJ, 707:L117, 2009.

Gordon and Breach, “Relativity, groups and topology”, Science Publishers Inc, 1964, p525-p527.

Haskell, B., 2008, R. Astron. Soc. 385, 531–542.

Hobbs, G., “Pulsars as gravitational wave detectors”, arXiv006.3969v1,26 June 2010.

Hotokezaka, K., arXiv:1105.4370v1 [astro-ph.HE], 22 May 2011.

Hughes, S, “Gravitational waves from merging compact binaries”,
<http://arxiv.org/abs/0903.4877v3>

Jones, D.H , APJ,580:L137-L141, 2002.

King, A.R., Watson, M.G., “The Shortest Period Binary Star”, Nature, 323:105, 1986.

Kiuchi, K., <http://arxiv.org/abs/1206.0509v1>

Konstantin, A., Postnov, The evolution of compact binary star system, Living Rev. relativity, 9, 2006.

Kotake, K, “Explosion Mechanism, Neutrino Burst, and Gravitational Wave in Core-Collapse Supernovae”,arXiv:astro-ph/0509456v2, 16 Sep 2005.

Landau, L.D, Lifschitz, E.M., “The classical theory of fields”,Volume 2,1975,p269.

Liu, K. “Prospects of probing the Spacetime of Sgr A*”. ApJ, 747:1, 2012.

Matthew Pitkin et al., “Gravitational Wave Detection by Interferometry (Ground and Space)”, <http://www.livingreviews.org/lrr-2011-5>.

Misner, C. W. , K. S. Thorne, and J. A. Wheeler, 1970, “Gravitation”, first preliminary edition (University of Maryland, College Park).

Muller, E., “Gravitational radiation from convective instabilities in Type II supernova explosions” Astron. Astrophys. 317, 140–163 (1997).

Muller, E., 1991, A&A,246,417M.

Peters, P.C, Matthews , J. 1963, Physical Review,136,435.

Pertry, Walter, “Lorentz covariant theory of Gravity”,GR and gravitation, Vol. 10, No. 7, 1979, p 599.

Pertry, Walter, “Cosmological Model without singularities”,GR and gravitation, Vol. 13, No. 11, 1981.

Pertry, Walter, “PN approximation of Gravitation theory of Flat space”, 1992, AP&SS, 189, p. 63.

Pitkin, M. et al., Gravitational Wave Detection by Interferometry (Ground and Space), Living Rev. Relativity 14, (2011), 5. <http://www.livingreviews.org/lrr-2011-5>.

Read, J.S et al., “Matter effects on binary neutron star waveforms”, arXiv:1306.4069v1 [gr-qc], 18 June 2013.

Reisswig, C, Ott, C.D., “Gravitational Wave Extraction in Simulations of Rotating Stellar Core Collapse” arXiv:1012.0595v2 [gr-qc] 8 Mar 2011.

Scharf, G., Journal of Modern Physics 2, 274 (2011),1101.1207.

Shibata, M., arXiv:gr-qc/0203037v1 [gr-qc], 12 Mar 2002.

Spitler et al., arXiv:1309.4472v1 [astro-ph.HE], 18 September 2013.

Springel V., 2005, MNRAS, 364, 1105 [GADGET CODE].

Stella, L., APJ, 634:L165–L168, 2005.

Stella, L., arXiv:0811.4311v1,[astro-ph], 26 Nov 2008.

Taylor, J.H., & Weisberg J.M. 1982, ApJ, 253, 908.

Thompson, A, “Shock breakout in core-collapse supernovae and its neutrino signature” arXiv:astro-ph/0211194v2, 2 April 2003.

Thorne, K. S. , 1980, Mon. Not. Roy. Astron. Soc.

Will, C., Zaglaur W., ApJS, 346, 1989.

Appendix A

The weak field limit and the quadrupole formalism

In Newtonian theory, gravitation is considered as an instantaneous force between two objects and any gravitational effects are transmitted with infinite speed ($v \rightarrow \infty$). Einstein's theory does not suffer from this effect. Just gravitational effects travel at the speed of light. In Einstein theory gravity is interpreted geometrically.

In this thesis we use Greek indices $\mu, \nu, \alpha, \beta \in \{0, 1, 2, 3\}$ where the zero indexes represents the time component and the Latin indices i, j, k denote the spatial components.

The metric tensor $g_{\mu\nu}$ is used to measure the length between two spacetime coordinates (x^μ and $x^\mu + dx^\mu$), i.e. the metric measures the lengths of vectors situated at the event x^μ . It is this metric tensor that defines the geometrical properties of the spacetime. The components of the metric $g_{\mu\nu}$, when expressed in terms of a set of inertial coordinates, take the form

$$g_{\mu\nu} = \eta_{\mu\nu} = \text{diag}(-1, 1, 1, 1). \quad (\text{A.1})$$

In this thesis we use the signature $(-, +, +, +)$ throughout.

This produces a spacetime interval (or line-element)

$$ds^2 = -dt^2 + (dx^1)^2 + (dx^2)^2 + (dx^3)^2. \quad (\text{A.2})$$

Or using the Einstein summation notation the spacetime interval can be expressed as

$$ds^2 = \eta_{\mu\nu} dx^\mu dx^\nu. \quad (\text{A.3})$$

The spacetime interval remains invariant under coordinate transformations and is either positive, negative or zero, i.e. for a $(-, +, +, +)$ signature

$$ds^2 = \begin{cases} 0, \text{ null} \\ > 0, \text{ spacelike} \\ < 0, \text{ timelike} \end{cases}. \quad (\text{A.4})$$

The physical interpretation of Eq. (A.4) is as follows: non-zero rest mass particles satisfies $ds^2 < 0$ (timelike), while spacetime travel with velocities $v > c$ would satisfy $ds^2 > 0$ (spacelike), whereas for photons $ds^2 = 0$. This is illustrated in Fig. A.1.

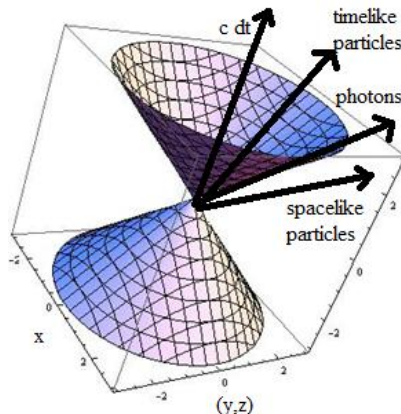


Fig. A.1: Null-cone construction in Minkowskian spacetime.

The world-lines of photons are called light-like geodesics (only under no external forces). The world lines of free-particles are called time-like world-lines. These geodesics can be calculated from the variational problem of the spacetime interval (geodesics are the straightest world-lines and extremal world-lines with respect to the metric)

$$\delta \int ds^2 = 0, \quad (\text{A.5})$$

This produces a world-line (geodesic equation)

$$\frac{\partial^2 x^\mu}{\partial \lambda^2} + \Gamma_{\alpha\beta}^\mu \frac{\partial x^\alpha}{\partial \lambda} \frac{\partial x^\beta}{\partial \lambda} = 0. \quad (\text{A.6})$$

Here λ represents an affine parameter and where $\Gamma_{\alpha\beta}^\mu$ represent the Christoffel symbols. These symbols are represented by

$$\Gamma_{\alpha\beta}^\mu = 0.5 g^{\mu k} \left(\frac{\partial g_{k\beta}}{\partial x^\alpha} + \frac{\partial g_{\alpha k}}{\partial x^\beta} - \frac{\partial g_{\alpha\beta}}{\partial x^k} \right), \quad (\text{A.7})$$

The presence of mass (or subsequently energy) curves the fabric of space surrounding the object and directly determines the metric of the spacetime. Einstein formulated this fundamental idea in the form of the Einstein Field equations

$$G^{\mu\nu} = \frac{8\pi G}{c^4} T^{\mu\nu}. \quad (\text{A.8})$$

Here $G^{\mu\nu}$ is the Einstein tensor (which fundamentally contains the metric tensor that geometrically describes the spacetime) and $T^{\mu\nu}$ is the stress tensor of the source that curves spacetime. If there is no source present then the Einstein equations reduce to the vacuum equations (equations of flat space, $G^{\mu\nu} = 0$).

In this Appendix the basic properties of GWs will be reviewed. The discussion will present the properties of GWs within the frameworks of General Relativity (the quadrupole weak-field formalism) and the Post Newtonian theory. Each of these provides a vehicle to explore certain aspects of the GW emission of astrophysical sources.

In order to produce a weak field limit approximation and ultimately deduce an equation to relate a gravitational wave and a possible source, typically being the stress energy tensor $T^{\alpha\beta}$, a very small perturbation or change can be introduced to the metric, starting with Minkowskian background

$$g_{\alpha\beta} = \eta_{\alpha\beta} + h_{\alpha\beta}. \quad (\text{A.9})$$

Defining index raising and lowering operators: $h_\beta^\mu = \eta^{\mu\alpha} h_{\alpha\beta}$, $h^{\mu\nu} = \eta^{\mu\beta} h_\beta^\nu$, $h = \eta^{\mu\nu} h_{\mu\nu}$
also

$$g^{\mu\nu} g_{\nu\rho} = \delta_\rho^\mu + O(h^2) \quad (\text{A.10})$$

Expanding the all the known GR quantities: Starting with the Riemann Tensor

$$R^\alpha_{\mu\alpha\nu} = \Gamma^\alpha_{\mu\nu,\alpha} - \Gamma^\alpha_{\mu\nu,\alpha} + O(h^2). \quad (\text{A.11})$$

Or in the full covariant form,

$$R_{\alpha\beta\mu\nu} = \frac{1}{2} (h_{\alpha\nu,\beta\mu} + h_{\beta\mu,\alpha\nu} - h_{\alpha\mu,\beta\nu} - h_{\beta\nu,\alpha\mu}). \quad (\text{A.12})$$

And generally the Christoffel Symbols can be expressed as follows:

$$\begin{aligned} \Gamma^\mu_{\alpha\beta} &= \frac{1}{2} g^{\mu\sigma} (g_{\alpha\sigma,\beta} + g_{\beta\sigma,\alpha} - g_{\alpha\beta,\sigma}) \\ &= \frac{1}{2} (h^\mu_{\alpha,\beta} + h^\mu_{\beta,\alpha} + h^\mu_{\alpha\beta}). \end{aligned} \quad (\text{A.13})$$

The Ricci tensor becomes

$$\begin{aligned} R_{\mu\nu} &= R^\sigma_{\mu\sigma\nu} = \Gamma^\sigma_{\mu\nu,\sigma} - \Gamma^\sigma_{\mu\sigma,\nu} \\ &= \frac{1}{2} \left(h^\sigma_{\nu,\mu\sigma} + h_{\mu\sigma,\nu}^\sigma - h_{\mu\nu,\sigma}^\sigma - h_{,\mu\nu}^\sigma \right). \end{aligned} \quad (\text{A.14})$$

The Ricci scalar, R , becomes

$$R = h^{\mu\sigma}_{,\mu\sigma} - h_{,\sigma}^\sigma. \quad (\text{A.15})$$

The Einstein tensor can expressed as,

$$G_{\mu\nu} = R_{\mu\nu} - 0.5\eta_{\mu\nu}R. \quad (\text{A.16})$$

Then

$$\begin{aligned} G_{\mu\nu} &= R_{\mu\nu} - 0.5\eta_{\mu\nu}R \\ &= \frac{1}{2} \left(h^\sigma_{\nu,\mu\sigma} + h_{\mu\sigma,\nu}^\sigma - h_{\mu\nu,\sigma}^\sigma - h_{,\mu\nu}^\sigma \right) - \frac{1}{2}\eta_{\mu\nu}(h^{\mu\sigma}_{,\mu\sigma} - h_{,\sigma}^\sigma) \\ &= \frac{1}{2} \left(h^\sigma_{\nu,\mu\sigma} + h_{\mu,\nu\sigma}^\sigma - \square h_{\mu\nu} - h_{,\mu\nu} - \eta_{\mu\nu}h^{\rho\sigma}_{,\rho\sigma} + \eta_{\mu\nu}\square h \right). \end{aligned} \quad (\text{A.17})$$

To simplify the Einstein tensor, we apply certain gauges. First of all we use the Lorentz gauge (harmonic gauge)

$$\partial_\mu h^{\mu\nu} = 0, \quad (\text{A.18})$$

together with the energy-momentum conservation laws:

$$\partial_\mu T^{\mu\nu} = 0. \quad (\text{A.19})$$

One could also define the traceless metric perturbation:

$$\bar{h}_{\mu\nu} = h_{\mu\nu} - \frac{1}{2}\eta_{\mu\nu}h, \quad (\text{A.20})$$

Together with the condition of:

$$\bar{h} = h \quad (\text{A.21})$$

To investigate the freedom of the harmonic gauge, one could easily perform a coordinate transformation ($X^{\mu'} = X^{\mu} + \xi^{\mu}$):

$$\partial^{\mu}\bar{h}_{\mu\nu} = \partial^{\mu}\bar{h}_{\mu\nu} - \square\xi^{\mu} \quad (\text{A.22})$$

From here one can fix the gauge freedom, by choosing $\square\xi^{\mu} = 0$. This choice will insure the invariance of $\partial^{\mu}\bar{h}_{\mu\nu}$.

Applying these gauges to Eq. (A.17)

$$\square\bar{h}_{\mu\nu} = -\frac{16\pi G}{c^4}T_{\mu\nu}. \quad (\text{A.23})$$

Using the principles of Green's solution, a solution to the wave equation becomes

$$\bar{h}_{\mu\nu}(t, \bar{x}) = \frac{4G}{c^4} \int \frac{T_{\mu\nu}(t - |\bar{x} - \bar{y}|, \bar{y})}{|\bar{x} - \bar{y}|} d^4y. \quad (\text{A.24})$$

where \bar{x} and \bar{y} represents the spatial coordinates of the field point and the source, respectively, and $|\bar{x} - \bar{y}|$ represents the distance between the source and the field point.

The volume integrals are taken over the part of space time with $t_{retarded} = t - |\bar{x} - \bar{y}|$.

Transforming the solution $\bar{h}_{\mu\nu}(t, \bar{x})$ to Fourier space leads to:

$$\tilde{h}_{\mu\nu}(\omega, \bar{x}) = \frac{4G}{\sqrt{2\pi c^4}} \int e^{i\omega t_{ret}} e^{i\omega |\bar{x} - \bar{y}|} \frac{T_{\mu\nu}(t_{retarded}, \bar{y})}{|\bar{x} - \bar{y}|} d^3y dt. \quad (\text{A.25})$$

Assuming the far away limit (where the distance between the field point and the source point could be set to the distance from the source to earth, namely $|\bar{x} - \bar{y}| \sim r$),

$$\tilde{h}_{\mu\nu}(\omega, \bar{x}) = \frac{4Ge^{i\omega r}}{rc^4} \int \tilde{T}_{\mu\nu}(\omega, \bar{y}) d^3y. \quad (\text{A.26})$$

Taking only the spatial part of $\tilde{h}_{\mu\nu}(\omega, \bar{x})$ and expanding the integral by using integration by parts ($\int \tilde{T}_{\mu\nu}(\omega, \bar{y}) d^3y$) leads to:

$$\tilde{h}_{ij}(\omega, \bar{x}) = -\frac{2Ge^{i\omega r}\omega^2}{rc^4} \int y^i y^j \tilde{T}_{00}(\omega, \bar{y}) d^3y. \quad (\text{A.27})$$

Using the definition of the Quadrupole tensor ($Q^{ij} = \int y^i y^j T^{00} d^3y$) leads to

$$\tilde{h}_{ij}(\omega, \bar{x}) = -\frac{2Ge^{i\omega r}\omega^2}{rc^4} \tilde{Q}_{ij}(\omega) \quad (\text{A.28})$$

Transforming back to the time domain

$$\bar{h}_{ij}(t, \bar{x}) = \frac{2G}{rc^4} \ddot{\tilde{Q}}_{ij} \quad (\text{A.29})$$

Finally applying the transverse gauge to the equation above leads to the definition of the signature of GWs that links to the changing quadrupole tensor of the source:

$$\bar{h}_{ij}^{TT} = \frac{2G}{rc^4} \Lambda_{ijkl} \hat{\mathcal{Q}}^{kl} \quad (\text{A.30})$$

Here $\Lambda_{ijkl} = P_i^k P_j^l - \frac{1}{2} P^{kl} P_{ij}$ represents the projection tensor (orthogonal to the direction of wave propagation) and $\hat{\mathcal{Q}}^{kl} = Q^{kl} - \frac{1}{3} \delta_{kl} Q$ represents the reduced quadrupole tensor. Also, we have that $P_{ij} = \delta_{ij} - \hat{x}_i \hat{x}_j$.

The effective stress-energy tensor of GWs is:

$$T_{\mu\nu} = \frac{c^4}{32\pi G} \langle h^{\beta\alpha}{}_{,\mu} h_{\alpha\beta,\nu} \rangle. \quad (\text{A.31})$$

The energy loss due to GW radiation through a sphere with radius r , can also be calculated since the stress-energy tensor contains the energy flux information,

$$E = \int_S T_{0\mu} n^\mu r^2 d\Omega \quad (\text{A.32})$$

Where n^μ is the normal vector that points in the direction of the radius r . If we restrict our problem to spherical coordinates, then

$$T_{0\mu} n^\mu = \frac{1}{32\pi G} \langle h_{\alpha\beta,0}^{TT} h^{\alpha\beta}_{TT,r} \rangle \quad (\text{A.33})$$

We could now use Eq. (A.30) to produce power radiated

$$\dot{E} = \left\langle \frac{G}{8\pi} \int \ddot{\mathcal{Q}}_{TT}^{ij} \ddot{\mathcal{Q}}_{ij}^{TT} d\Omega \right\rangle \quad (\text{A.34})$$

The only calculation that remains is to eliminate the TT's:

$$\mathcal{Q}_{TT}^{ij}\mathcal{Q}_{ij}^{TT} = (P_i^k P_j^l - \frac{1}{2} P^{kl} P_{ij})(P_i^a P_j^b - \frac{1}{2} P^{ab} P_{ij}) \ddot{\mathcal{Q}}_{TT}^{kl} \ddot{\mathcal{Q}}_{ab}^{TT} \quad (\text{A.35})$$

Using the fact that $P_{ij} = \delta_{ij} - \hat{x}_i \hat{x}_j$, together with several standard integrals for a surface S with radius r , as well as symmetry and null-trace characteristics of the quadrupole tensor, we get the power radiated due to GW radiation:

$$\dot{E} = \frac{G}{5c^5} \langle \ddot{\mathcal{Q}}^{ij} \ddot{\mathcal{Q}}_{ij} \rangle \quad (\text{A.36})$$

Appendix B

Detector sensitivity curves

Sensitivity curves are used to plot the strength required for a GW emitter, as a function of frequency, in order to be detectable by ground-based GW interferometers such as LIGO or VIRGO. There are two standard curves that are used, namely a strain sensitivity curve and an amplitude spectral density curve. Strain sensitivity curves are plots of strain (h) against GW frequency (f_{GW}) and amplitude spectral sensitivity (h_f) curves are plots of the square root of the power spectral density ($\sqrt{S_h}$) against GW frequency (f_{GW}). Here S_h is the power spectral density and represents the power per unit frequency and is often a more desirable representation of sensitivity curves. One could formulate the relation between GW strain (h) and power spectral density (h_f) as follows,

$$h_f = h \sqrt{S_f}, \quad (\text{B.1})$$

where h_f has units of $h \text{ Hz}^{-0.5}$.

Appendix C

The Post Newtonian expansion of Gravitation in flat space

In this appendix we use Greek indices $\mu, \nu, \alpha, \beta \in \{0, 1, 2, 3\}$ that include the time component and $i, j, k, l \in \{1, 2, 3\}$ denote the spatial components. To invoke the setup for the field equations, a good starting point would be the Euler equations of the system

$$\left(\frac{\partial L_G}{\partial g^{\mu\nu}} \right)_{;\alpha} = \frac{\partial L_G}{\partial g^{\mu\nu}} + 8\varphi \frac{\partial L_M}{\partial g^{\mu\nu}}, \quad (\text{C.1})$$

this problem can be expanded in short, by incorporating the Riemann curvature tensor in an appropriate way,

$$\begin{aligned} \partial g^{\mu\nu} / \partial x^k \left(\frac{\partial L_G}{\partial g^{\mu\nu}} \right)_{;\alpha} &= \partial g^{\mu\nu} / \partial x^k \frac{\partial L_G}{\partial g^{\mu\nu}} + 8\varphi \partial g^{\mu\nu} / \partial x^k \frac{\partial L_M}{\partial g^{\mu\nu}} \\ &\Rightarrow \left(\partial g^{\nu\mu} / \partial x^k \frac{\partial L_G}{\partial g^{\nu\mu}} \right)_{;\alpha} - \frac{\partial L_G}{\partial g^{\nu\mu}} g^{\nu\mu}_{;k;\alpha} = \partial g^{\mu\nu} / \partial x^k \frac{\partial L_G}{\partial g^{\mu\nu}} + 8\varphi \partial g^{\mu\nu} / \partial x^k \frac{\partial L_M}{\partial g^{\mu\nu}}. \end{aligned} \quad (\text{C.2})$$

Since the Riemann Tensors consists of first and second derivative of the metric, the term from (C.2), $g^{\nu\mu}_{;k;\alpha}$, contain the nested Riemann Tensors, ultimately (Petry, 1978) reduced (C.2) to a very elegant form,

$$\left(\frac{\partial g^{\nu\mu}}{\partial x^\alpha} \frac{\partial L_G}{\partial g^{\nu\mu}} - \delta_k^\alpha L_G \right)_{;\alpha} - 2g^{\beta\mu} R_{\beta k\alpha}^\nu \frac{\partial L_G}{\partial g^{\nu\mu}} = 16\varphi \left(\rho g_{k\alpha} \frac{dx_\alpha}{d\tau} \frac{dx_\beta}{d\tau} \right)_{;\beta} - g_{k\alpha} \frac{dx_\alpha}{d\tau} \left(\rho \frac{dx_\beta}{d\tau} \right)_{;\beta}$$

(C.3)

Imposing the conditions of $T_{\mu\nu} = T_{\mu\nu}^G + T_{\mu\nu}^M$, particle conservation $\left(\rho \frac{dx_\beta}{d\tau} \right)_{;\beta} = 0$, the condition of flat space $R_{\beta k\alpha}^\nu = 0$ and tensor analysis identity $T_\nu^\mu = g^{\mu\alpha} T_{\alpha\nu}$, equation (C.1) with the use of equations (C.2)- (C.3) becomes

$$\left((-G)^{0.5} g^{\alpha\beta} g_{\nu\mu} \frac{\partial g^{\nu\mu}}{\partial x^\beta} \right)_{;\alpha} = 4\varphi T_\mu^\nu.$$

(C.4)

Finally summing over the indices $\{\mu, \nu\}$, equation (C.4) becomes
 $\left((-G)^{0.5} g^{\alpha\beta} g_{\nu\mu} \frac{\partial g^{\nu\mu}}{\partial x^\beta} \right)_{;\alpha} = 4\varphi T_\alpha^\alpha$, this result represents the new field equations, after

incorporating the total tensor $T_{\mu\nu} = T_{\mu\nu}^G + T_{\mu\nu}^M$.

```
//////////  

#init metric tensor!!  

> g_compts:=array(sparse,1..4,1..4):  

> g_compts[1,1]:=(1+2*U/c^2)*delta:  

g_compts[2,2]:=(1+2*U/c^2)*delta:  

g_compts[3,3]:=(1+2*U/c^2)*delta:  

g_compts[4,4]:=-1*(1-(2*U/c^2)+S/c^4):  

g_compts[1,4]:=-1*4*V_i/c^3:  

g_compts[2,4]:=-1*4*V_i/c^3:  

g_compts[3,4]:=-1*4*V_i/c^3:  

g_compts[4,1]:=-1*4*V_j/c^3:  

g_compts[4,2]:=-1*4*V_j/c^3:  

g_compts[4,3]:=-1*4*V_j/c^3:  

#create metric tensor!! (C.5)  

> g:=create([-1,-1], eval(g_compts));  

g := TABLE  

compts = 
$$\begin{bmatrix} \left(1 + \frac{2U}{c^2}\right)\delta & 0 & 0 & -\frac{4Vi}{c^3} \\ 0 & \left(1 + \frac{2U}{c^2}\right)\delta & 0 & -\frac{4Vi}{c^3} \\ 0 & 0 & \left(1 + \frac{2U}{c^2}\right)\delta & -\frac{4Vi}{c^3} \\ -\frac{4Vj}{c^3} & -\frac{4Vj}{c^3} & -\frac{4Vj}{c^3} & -1 + \frac{2U}{c^2} - \frac{S}{c^4} \end{bmatrix},$$
  


```

```
//////////
```

```
>sort(expand(MassTensor_compts[4,4]),c);  

#T44!!
```

$$-1. \rho c^2 - 1.0 \rho v^2 - 1. \rho H - 2 \rho U$$

```
>sort(expand(MassTensor_compts[1,1]),c);  

#T11!!
```

$$p \delta^2 c^2 + p \delta^2 U + 1. p \delta v_{\perp} l^2 + 1. p \delta v_{\perp} l^2$$

```
>sort(expand(MassTensor_compts[1,4]),c);
```

#T14!!

$$1.p \delta v_I c + 1.p \delta v_I c - \frac{4 p V j \delta}{c} + \frac{6.p \delta v_I U}{c} - \frac{4.p V i}{c} + \frac{1.p \Pi \delta v_I}{c} + \frac{1.0 p \delta v_I v^2}{c}$$

```
>sort(expand(MassTensor_compts[4,1]),c);
```

#T41 ! !

$$-1.v_I p c - 1.v_I p c - \frac{4 p V j \delta}{c} - \frac{1.v_I p H}{c} + \frac{4 p V i}{c} - \frac{1.0 v_I p v^2}{c} - \frac{1.0 v_I p v^2}{c} - \frac{2 v_I p U}{c} - \frac{2 v_I p U}{c} \quad (C.6)$$

.....

#Gravity tensor T44 !!

$$\begin{aligned}
 & -\frac{0.6562500000 \delta^4 D_{-ct}^2 S}{K c^4} + \frac{0.1250000000 D_{-3}^2 \delta U^2}{K c^4} - \frac{1.500000000 \delta^3 U^2 D_{-J^2}}{K c^4} \\
 & + \frac{5.250000000 \delta^2 U^2 D_{-ct}^2}{K c^4} - \frac{1.125000000 \delta^5 D_{-2}^2 U^2}{K c^4} + \frac{0.1250000000 \delta D_{-J^2} U^2}{K c^4} \\
 & - \frac{1.750000000 D_{-ct}^2 U^2}{K c^4} - \frac{1.312500000 \delta^2 D_{-ct}^2 S}{K c^4} - \frac{1.125000000 \delta^5 D_{-J^2} U^2}{K c^4} \\
 & + \frac{0.2187500000 D_{-ct}^2 S}{K c^4} - \frac{1.125000000 \delta^5 D_{-3}^2 U^2}{K c^4} - \frac{1.500000000 \delta^3 U^2 D_{-J^2}}{K c^4}
 \end{aligned}$$

#Gravity tensor T11!!

$$\begin{aligned}
& \frac{0.3750000000 \delta^6 V_{jD_ctD_I}}{Kc^3} - \frac{1.500000000 \delta^7 D_{_3}^2 U^2}{Kc^4} + \frac{0.09375000000 \delta^6 D_{_ct}^2 S}{Kc^4} \\
& + \frac{6.750000000 \delta^5 D_{_I}^2 U^2}{Kc^4} - \frac{0.03125000000 D_{_ct}^2 \delta^2 S}{Kc^4} + \frac{0.2500000000 \delta^3 D_{_2}^2 U^2}{Kc^4} \\
& + \frac{0.3750000000 \delta^6 D_{_ct}^2 U^2}{Kc^4} - \frac{1.0000000000 U^2 D_{_I}^2 \delta}{Kc^4} + \frac{0.2500000000 \delta^3 D_{_3}^2 U^2}{Kc^4} \\
& + \frac{12.250000000 \delta^3 U^2 D_{_I}^2}{Kc^4} - \frac{2.2500000000 \delta^5 U^2 D_{_2}^2}{Kc^4} - \frac{2.2500000000 \delta^5 U^2 D_{_3}^2}{Kc^4} \\
& - \frac{1.5000000000 \delta^7 D_{_I}^2 U^2}{Kc^4} + \frac{0.1875000000 \delta^4 D_{_ct}^2 S}{Kc^4} + \frac{0.1250000000 D_{_ct}^2 \delta^2 U^2}{Kc^4} \\
& - \frac{1.5000000000 \delta^7 D_{_2}^2 U^2}{Kc^4} + \frac{0.2500000000 V_{jD_ctD_2} \delta^2 U}{Kc^5} - \frac{0.7500000000 \delta^6 V_{jD_ctD_I} U}{Kc^5}
\end{aligned}$$

#Gravity tensor T14 !!

$$\frac{1.000000000 U^2 D_{_ct} \delta D_{_I}}{K c^4} + \frac{12.00000000 \delta^3 U^2 D_{_ct} D_{_I}}{K c^4} + \frac{9.000000000 \delta^5 D_{_ct} D_{_I} U^2}{K c^4}$$

$$\frac{0.7500000000 \delta^5 D_{_I}^2 V_{_i} U}{K c^5} + \frac{1.500000000 \delta^4 V_{_j} U D_{_I}^2}{K c^5} + \frac{0.7500000000 \delta^6 D_{_I}^3 V_{_j} U}{K c^5}$$

$$\frac{0.7500000000 \delta^5 D_{_I}^2 V_{_i} U}{K c^5} + \frac{0.2500000000 D_{_I}^2 \delta V_{_i} U}{K c^5} + \frac{0.7500000000 \delta^5 D_{_ct}^2 V_{_j} U}{K c^5}$$

#Gravity tensor T41!!

$$\begin{aligned} & \frac{1.000000000 U^2 D_{-ct} \delta D_{-J}}{K c^4} + \frac{12.00000000 \delta^3 U^2 D_{-ct} D_{-J}}{K c^4} + \frac{9.000000000 \delta^5 D_{-ct} D_{-J} U^2}{K c^4} \\ & - \frac{0.7500000000 \delta^5 D_{-2}^2 V_{-j} U}{K c^5} + \frac{1.500000000 \delta^4 V_{-j} U D_{-J}^2}{K c^5} + \frac{0.7500000000 \delta^6 D_{-3}^2 V_{-j} U}{K c^5} \end{aligned} \quad (C.7)$$

100% of the energy consumed by the U.S. economy is derived from fossil fuels.

Appendix D

GADGET code and files

Initialization code:

```

/*Begin::: Gravitational Wave calculation: SPH Q-pole formulation>>>/
%N_gas== the number of particles for the run

for (k=0;k<N_gas;k++)
{
    I_11+=
    2*P[k].Mass*P[k].Vel[1]*P[k].Vel[1]+(2*P[k].Mass*SphP[k].Pressure/
    SphP[k].Density)+2*P[k].Mass*P[k].Mass*P[k].Vel[1]*P[k].GravAccel[1];

    I_22+=
    2*P[k].Mass*P[k].Vel[2]*P[k].Vel[2]+2*(P[k].Mass*SphP[k].Pressure
    /SphP[k].Density)+2*P[k].Mass*P[k].Mass*P[k].Vel[2]*P[k].GravAccel[2];

    I_12+=
    2*P[k].Mass*P[k].Vel[1]*P[k].Vel[2]+P[k].Mass*P[k].Mass*P[k].Vel[2]*P[k
    ].GravAccel[1]+P[k].Mass*P[k].Mass*P[k].Vel[1]*P[k].GravAccel[2];

    I_13+=
    2*P[k].Mass*P[k].Vel[1]*P[k].Vel[3]+P[k].Mass*P[k].Mass*P[k].Vel[3]*P[k
    ].GravAccel[1]+P[k].Mass*P[k].Mass*P[k].Vel[1]*P[k].GravAccel[3];
}

```

```

I_23+=
2*P[k].Mass*P[k].Vel[2]*P[k].Vel[3]+P[k].Mass*P[k].Mass*P[k].Vel[2]*P[k]
].GravAccel[3]+P[k].Mass*P[k].Mass*P[k].Vel[3]*P[k].GravAccel[2];

SystemDensity+=SphP[k].Density;
}

%writing out the GW data

h_cross_plane= (2*GG/(c_4*distance))* (I_12);
h_plus_plane= fabs((GG/(c_4*distance))* (I_11-I_22));
A_E2=distance*3.66*h_plus_plane;

%writing to file .dat

FILE *GRAV;
GRAV=fopen ("r_cross.dat","a");
fprintf(GRAV,"%f,%e,%e,%e\n",count,h_cross_plane,A_E2,SystemDensity);
count+=1;
fclose(GRAV);

/* End: Gravity Wave calculation: SPH Q-pole formulation>>>>>>>> */
~~~~~

```

Mass distribution setup:

```

~~~~~
; Number of Particles..... .

ngas = 21^round(15)

; Constants..... .

G = 6.6738e-8
msun = 1.98892e33

```

```

omega=0
rho0 = 0.14
gamma = 4.0/3

mgas=10*msun
rgas = 5.9d11

tff = sqrt(3*3.1416/(32*G*rho0))

; Setting the units of the simulation.....
unitMass_in_g = Msun
unitTime_in_s = tff
unitLength_in_cm = rgas
unitVelocity_in_cm_per_s = unitLength_in_cm / unitTime_in_s

; Scaling things to code units

rgas /= UnitLength_in_cm
mgas /= UnitMass_in_g
omega *= UnitTime_in_s
~~~~~
```